

Università di Pisa

Facoltà di Scienze Matematiche Fisiche e Naturali

Corso di Laurea Specialistica in Scienze Fisiche

Anno Accademico 2016/2017

Tesi di Laurea Specialistica

Intrappolamento ottico di atomi di disprosio per la realizzazione  
di un condensato di Bose-Einstein di atomi dipolari

(Optical Trapping of Dysprosium Atoms in view of a Dipolar Bose-Einstein  
Condensate)

Candidato  
Alessandro Fregosi

Relatore  
Dr. Andrea Fioretti  
Co-Relatore  
Prof. Danilo Giulietti



# CONTENTS

INTRODUCTION	2
1 THEORETICAL BACKGROUND	5
1.1 Radiative force	5
1.2 Absorption cross section	7
1.3 Radiative force and Doppler effect	9
1.3.1 1D Optical molasses	10
1.4 Radiative force and Zeeman effect	11
1.4.1 Magneto optical trap	13
1.5 Dipole force	15
1.5.1 Optical dipole trap	15
1.5.2 Spatial distribution of atoms in an optical dipole trap	16
1.6 Evaporative cooling	16
1.7 Bose-Einstein condensation	18
1.7.1 Non interacting particles	18
1.7.2 Interacting particles	20
1.8 Atomic beam	21
1.9 Dysprosium	23
2 EXPERIMENTAL SETUP	27
2.1 Vacuum chamber	29
2.2 The 421 nm laser	32
2.2.1 Zeeman Slower and transverse cooling	33
2.3 The 626 nm laser	34
2.3.1 Iodine lock	36
2.3.2 MOT optical design	36
2.4 The 1064 nm lasers	37
2.4.1 Resonator optical trap	37
2.4.2 Single-beam optical dipole traps	38
2.5 Imaging setup	40
2.5.1 Time of flight measurement	41
2.5.2 Horizontal imaging magnification	42
3 RESULTS	43
3.1 Transverse cooling	44
3.2 Zeeman Slower	45
3.3 626 nm MOT	52
3.3.1 MOT imaging	53
3.3.2 MOT detuning and related characteristics	55

3.3.3	MOT population temporal evolution	56
3.3.4	MOT dimensions and temperature	58
3.3.5	Oven temperature and MOT population	58
3.3.6	Other MOTs in literature	58
3.4	Resonator optical dipole trap	60
3.5	MOT to resonator optical dipole trap transfer	62
3.5.1	The resonator trap lifetime	65
3.6	Single beam optical dipole traps	67
3.6.1	Crossed optical dipole traps frequencies	67
3.6.2	Ods lifetime	72
3.7	Evaporative cooling and first signs of Bose-Einstein condensation	72
	CONCLUSIONS	74
	References	79

# INTRODUCTION

Dilute quantum degenerate [1, 7, 9] gases can be considered at the intersection of atomic and statistical physics. Thanks to the development in laser manufacturing it is nowadays possible to trap atomic clouds at temperatures so low to achieve quantum degenerate phases, such as the Bose-Einstein condensation or the degenerate Fermi gases. It has also been possible to efficiently load these quantum degenerate clouds into optical lattices, i.e. lattices formed by the interference of laser beams, therefore virtually defect-free with period and depth experimentally controllable to a great extent. These systems can be used to realize experimental models of typical solid-state physics problems [5].

The majority of these experiments use alkali or alkaline-like earth atoms that interact with each other through a short range isotropic potential (contact interaction). This potential can be described by a single parameter  $a_s$  called *scattering length* (or *s-wave scattering length*) which can be tuned by a magnetic field using the so called *Feshbach resonances*; in this way it is possible to obtain attractive, repulsive or non interacting atomic clouds.

During the last years the interest in the realization of cold gases formed by particles, atoms or molecules, with a natural magnetic or electric dipole moment is growing. Given the long-range and anisotropic nature of the dipole-dipole interaction, these gases are predicted to show different properties than those regulated by the contact interaction only, as bulk systems [18] or loaded in an optical lattice [33]. A comparison between the contact and the dipolar interaction strength is expressed by the ratio between the scattering length  $a_s$  and the so called *dipolar length*  $a_{\text{DD}}$  which quantifies the strength of the dipolar interaction; the physical properties of these systems are determined by this ratio. The first experiment devoted to the study of a dipolar ultracold gas used Chromium ( $\mu = 6\mu_B$ ) [17] and in that case the scattering length was frustrated using a Feshbach resonance. More recently the interest is devoted to the lanthanides elements and in particular to erbium ( $\mu = 7\mu_B$ ) and dysprosium ( $\mu = 9.93\mu_B$ ). The dipolar length  $a_{\text{DD}}$  is proportional to the squared (electric or magnetic) dipole moment and as a consequence the use of atoms with higher magnetic dipole moment facilitate the emerging of the dipolar nature on the trapped element. In this picture, dysprosium is particularly interesting not only because of it has the highest magnetic dipole moment among stable elements but also because is present with both bosonic and fermionic stable isotopes.

This thesis work has been done in the Laboratorio Disprosio in the Pisa Section of the Istituto Nazionale di Ottica of the Consiglio Nazionale delle Ricerche. This laboratory runs an experiment devoted to the Bose-Einstein condensation of  $^{162}\text{Dy}$  performed in partnership with the LENS in Florence. My work started when the initial cooling schemes of dysprosium were implemented and finished when the first results on the Bose-Einstein condensation were obtained.

The condensation of  $^{162}\text{Dy}$  is achieved starting from a dysprosium beam emerging from a high temperature effusive oven. This beam is collimated and slowed using the 421 nm wide transition. The first confinement and further cooling is realized in a magneto optic trap (MOT) that operates with the 626 nm narrow transition. Given the low Doppler temperature of the MOT, dysprosium atoms can be captured in an optical dipole trap realized in a high finesse Fabry-Perot cavity that permits to obtain a large waist and a sufficiently high potential well. Subsequently atoms are transferred in a crossed optical dipole trap where as a results of forced evaporation cooling the Bose-Einstein condensation is achieved. All the optical dipole traps operate with 1064 nm radiation. Data are extracted with standard absorption imaging.

This Thesis is divided in three chapters: the first one, of theoretical nature, presents the scattering and dipole forces and their use in the experiment, then the forced evaporative cooling process and finally the Bose-Einstein condensation for non interacting bosons in an harmonic potential. The second chapter is devoted to the description of the apparatus, the control systems for the lasers frequency and the imaging setup while in the last chapter the results obtained are presented .

My contribution has been mainly experimental as I participated in most of the measurements reported in this Thesis concerning the MOT and the optical dipole trap characterization.

I also developed a Mathematica™ code to calculate the characteristics of one or more dipole traps, to perform a comparison with the experimental data. The results of this code are reported in the last chapter.

# THEORETICAL BACKGROUND

In this chapter I will briefly report some concepts concerning the interaction between an atomic beam and the laser light that will be used to perform the slowing, cooling and trapping processes. In order to maintain the text compact and ordered, in spite of subject coherence, after a first part regarding the light matter interaction, I will add a brief description of the atomic beam. The whole description will be restricted to a two levels atom in a semiclassical framework, thus the atom is described by quantum mechanics while the laser field is considered as a classic field. This is a vast and well known subject, so the aim of this chapter is simply to report the essential facts to provide a compact framework in which, the processes described in this Thesis, are contained. The reference books used are [25] and [11] so a more detailed descriptions can be found there as well as in many others books.

## 1.1 RADIATIVE FORCE

In a two level approximation the atom is considered to be in a state

$$\begin{aligned}\Psi(\mathbf{r}, t) &= c_1(t)\psi_1(\mathbf{r}, t) + c_2(t)\psi_2(\mathbf{r}, t) \\ &= c_1(t)\varphi_1(\mathbf{r})e^{-i\omega_1 t} + c_2(t)\varphi_2(\mathbf{r})e^{-i\omega_2 t}\end{aligned}\tag{1.1}$$

that is a linear combination of the two  $H_0$  eigenstates  $H_0\varphi_i = E_i\varphi_i$  and where  $\omega_i = E_i/\hbar$ .

The semiclassical Hamiltonian of an atom in a electromagnetic field is

$$H = \frac{1}{2m} \left( \mathbf{p} + \frac{e}{c} \mathbf{A} \right)^2 + V(\mathbf{r})\tag{1.2}$$

where  $\mathbf{A}(\mathbf{r}, t)$  is the vector potential and  $\mathbf{E}(\mathbf{r}, t) = -\frac{1}{c} \frac{\partial \mathbf{A}}{\partial t}$  is the electric field. In the Coulomb gauge ( $\nabla \cdot \mathbf{A} = 0$ ), and neglecting the  $\mathbf{A}^2$  term, the previous Hamiltonian can be written as

$$H = \frac{\mathbf{p}^2}{2m} + V(\mathbf{r}) + \frac{e}{mc} \mathbf{p} \cdot \mathbf{A} = H_0 + H'.\tag{1.3}$$

Assuming  $\mathbf{A}(\mathbf{r}, t) = \frac{\mathbf{A}_0}{2} (e^{i(\mathbf{k}\mathbf{r}-\omega t)} + e^{-i(\mathbf{k}\mathbf{r}-\omega t)})$  and taking into account that  $\frac{\lambda}{2\pi} \simeq 100 \text{ nm}$  while the Bohr radius is  $a_B \simeq 0.5 \text{ \AA}$  it can be considered  $e^{i\mathbf{k}\mathbf{r}} \simeq 1$  over the atomic volume; this is the *electric dipole approximation*:  $\mathbf{A}(\mathbf{r}, t) = \mathbf{A}_0 \cos(\omega t)$ . Using the commutation rules between  $H_0$ ,  $\mathbf{r}$  and  $\mathbf{p}$  the last term in EQ. 1.3 can be written in the form

$$H' = \mathbf{e}\mathbf{r} \cdot \mathbf{E}_0 \frac{e^{i\omega t} + e^{-i\omega t}}{2}; \quad \mathbf{E}_0 = \frac{E_1 - E_2}{\hbar c} \mathbf{A}_0. \quad (1.4)$$

Using the Hamiltonian in EQ. 1.3 in the time dependent Schrödinger equation for the wave function in EQ. 1.1 yields to

$$\begin{aligned} i\dot{c}_1(t) &= c_2(t) \frac{\langle 1|\mathbf{e}\mathbf{r} \cdot \mathbf{E}_0|2\rangle}{\hbar} \left( e^{i(\omega-\omega_A)t} + e^{-i(\omega+\omega_A)t} \right) \\ i\dot{c}_2(t) &= c_1(t) \frac{\langle 2|\mathbf{e}\mathbf{r} \cdot \mathbf{E}_0|1\rangle}{\hbar} \left( e^{-i(\omega-\omega_A)t} + e^{i(\omega+\omega_A)t} \right) \end{aligned} \quad (1.5)$$

where

$$\omega_A = \frac{E_2 - E_1}{\hbar}. \quad (1.6)$$

The weak field approximation  $c_1(t) \simeq 1$  is not valid in the case of the interaction with a coherent field that can actually drive significant displacements from equilibrium among the two populations, then, the two EQ. 1.5 have to be solved simultaneously. For  $\omega \simeq \omega_A$  the exponential term in  $(\omega + \omega_A)$  can be neglected and this case is called the *rotating wave approximation* (RWA). With these approximation EQ. 1.5 can be rearranged in two second order linear differential equations. For the  $c_2(t)$  term the equation is:

$$\ddot{c}_2 + i\delta\dot{c}_2 + \frac{|\Omega|^2}{2} c_2 = 0 \quad (1.7)$$

having defined the *Rabi frequency*  $\Omega$  and the *detuning*  $\delta$  as

$$\begin{aligned} \Omega &= \frac{\langle 1|\mathbf{e}\mathbf{r} \cdot \mathbf{E}_0|2\rangle}{\hbar} = E_0 e \frac{\langle 1|r|2\rangle}{\hbar} \cos(\theta) \\ \delta &= \omega - \omega_A \end{aligned} \quad (1.8)$$

where  $\theta$  is the angle between the quantization axis of the atom and the electric field.

The excited state population is described by  $|c_2(t)|^2$  that results in

$$|c_2(t)|^2 = \frac{\Omega^2}{\Omega^2 + \delta^2} \sin^2 \left( \frac{\sqrt{\Omega^2 + \delta^2}}{2} t \right). \quad (1.9)$$

The use of the  $c_i(t)$  coefficients implies that the atom is in a pure state but, because of the spontaneous emission, the atom is actually in a superposition of states each with a probability  $p_i$  therefore the density matrix  $\rho$  has to be used. The  $\rho_{ii}$  terms are called the *populations* of the states while the  $\rho_{ij} = \rho_{ji}^*$  are the *coherences*. In the case of a pure state, when the atom can be described by a complete wave function, the density matrix reduces to  $\rho_{ij} = c_i c_j^*$ .

The electric dipole moment of an atom in a state  $|\Psi(\mathbf{r}, t)\rangle$  where  $\Psi$  is given by EQ. 1.1, is

$$\begin{aligned} \mathbf{d}(\mathbf{t}) &= -e \langle \Psi|\mathbf{r}|\Psi \rangle = -e(c_2^* c_1 \langle 1|\mathbf{r}|2\rangle e^{i\omega_A t} + c_1^* c_2 \langle 2|\mathbf{r}|1\rangle e^{-i\omega_A t}) \\ &= -e \langle 1|\mathbf{r}|2\rangle (\rho_{12} e^{i\omega_A t} + \rho_{21} e^{-i\omega_A t}). \end{aligned} \quad (1.10)$$

Defining  $\hat{c}_1 = c_1 e^{-i\frac{\delta}{2}t}$ ;  $\hat{c}_2 = c_1 e^{i\frac{\delta}{2}t}$  so that  $\hat{\rho}_{12} = \rho_{12} e^{i\delta t}$  and  $\hat{\rho}_{21} = \rho_{21} e^{-i\delta t}$ , EQ. 1.10 can be written in the form

$$\mathbf{d}(\mathbf{t}) = -e\langle 1|\mathbf{r}|2\rangle (u \cos \omega t - v \sin \omega t) \quad (1.11)$$

where  $u = \hat{\rho}_{12} + \hat{\rho}_{21}$ ;  $v = -i(\hat{\rho}_{12} - \hat{\rho}_{21})$ .

A detailed description of the spontaneous emission is beyond the scope of this thesis, here I will report that in a similar way used to obtain EQ. 1.5 and introducing the excited state lifetime  $\tau = \frac{1}{\Gamma}$  as the exponential decay time constant for the  $\rho_{22}$  population and  $\gamma/2$  for the coherences yield to the *optical Bloch equations* whose stationary solutions are:

$$\begin{pmatrix} u \\ v \\ w \end{pmatrix} = \frac{1}{\delta^2 + \frac{\Omega^2}{2} + \frac{\gamma^2}{4}} \begin{pmatrix} \Omega\delta \\ \frac{\Omega\gamma}{2} \\ \delta^2 + \frac{\gamma^2}{4} \end{pmatrix} \quad (1.12)$$

where  $w = \rho_{11} - \rho_{22}$  and finally for  $\rho_{22}$  it can be written as

$$\rho_{22} = \frac{1}{2}(1 - w) = \frac{1}{2} \frac{\Omega^2/2}{\delta^2 + \frac{\Omega^2}{2} + \frac{\gamma^2}{4}}. \quad (1.13)$$

The previous expression (EQ. 1.13) quantifies the number of photons scattered by an atom. In a plane-wave laser field every photon has the same wave vector and the same momentum  $\hbar\mathbf{k}$ , therefore, after each absorption (emission), the atom's momentum changes by the same (opposite for emission) amount. On the other hand, the spontaneous emission of a photon by the atom is symmetrically distributed with respect to the acquired dipole momentum direction giving an average of 0 after a long time compared to a spontaneous decay rate  $\gamma$ .

This change of the atomic momentum gives rise to a force, called the *radiative or scattering force*. The number of decays per second is given by  $R_s = \gamma\rho_{22}$  and each decay causes a momentum variation of  $\hbar\mathbf{k}$  therefore the radiative force can be written as  $\mathbf{F} = \hbar\mathbf{k}\gamma\rho_{22}$ . Using the expression (EQ. 1.13) it finally results in

$$\mathbf{F} = \hbar\mathbf{k} \frac{\gamma}{2} \frac{\Omega^2/2}{\delta^2 + \frac{\Omega^2}{2} + \frac{\gamma^2}{4}}. \quad (1.14)$$

## 1.2 ABSORPTION CROSS SECTION AND SATURATION INTENSITY

For a laser beam of intensity  $I = \frac{\epsilon_0 E_0^2}{2} c$  traveling through a medium with populations  $N_1$  and  $N_2$  for the ground and the excited states respectively, it can be written

$$\frac{dI}{dz} = -(N_1 - N_2)\sigma(\omega)I \quad (1.15)$$

where  $\sigma(\omega)$  is the *absorption cross section*. At the steady state, the energy absorbed per unity volume has to be equal to the energy emitted by spontaneous emission:

$$(N_1 - N_2)\sigma(\omega)I = N_2 A_{21} \hbar\omega \quad (1.16)$$

where

$$A_{21} = \frac{g_1}{g_2} \frac{e^2 \omega^3}{\pi \epsilon_0 \hbar c^3} \frac{|\langle 1|\mathbf{r}|2\rangle|^2}{3} \quad (1.17)$$

is the Einstein coefficient for the spontaneous emission and  $g_1$  and  $g_2$  the degenerancies of the ground and excited levels respectively.

An expression for  $\sigma(\omega)$  can be obtained from EQ. 1.16. Taking into account that  $N_1 + N_2 = N$ ,  $N_2 = \rho_{22}N$  and substituting the expression for  $\rho_{22}$  (EQ. 1.13) and the expression for the Rabi frequency (EQ. 1.8) the absorption cross section results

$$\sigma(\omega) = 3 \cos^2(\theta) \frac{g_2}{g_1} \frac{\pi c^2}{\omega_A^2} \frac{A_{21}^2}{\delta^2 + \gamma^2/4}. \quad (1.18)$$

Some attention has to be payed to EQ. 1.18: the 3 factor multiplying the whole expression arises from the isotropy of spontaneous emission  $A_{21} \propto \frac{1}{3} |\langle 1|\mathbf{r}|2\rangle|^2$  and from expressing the Rabi frequency in terms of  $A_{21}$  but  $\Omega^2 \propto |\langle 1|\mathbf{r} \cdot \hat{\mathbf{E}}_0|2\rangle|^2 = \cos^2(\theta) E_0^2 |\langle 1|\mathbf{r}|2\rangle|^2$  therefore if atoms aren't polarized in the right direction with respect to the incident light there is another  $\frac{1}{3}$  factor (from  $\frac{1}{4\pi} \int \cos^2(\theta) d\Omega = \frac{1}{3}$ ) to be taken into account and in EQ. 1.18 the 3 factor has to be substituted by 1.

At resonance ( $\omega = \omega_A$ ) and in absence of degenerancies ( $g_1 = g_2$  and  $A_{21} = \gamma$ ) EQ. 1.18 becomes:

$$\sigma(\omega_A) = 3 \cos^2(\theta) \frac{\lambda^2}{2\pi}. \quad (1.19)$$

Again from EQ. 1.16, writing  $N = N_1 + N_2 = (N_1 - N_2) + 2N_2$ , it can be obtained

$$N_1 - N_2 = \frac{N}{1 + I \frac{2\sigma(\omega)}{\hbar\omega A_{21}}} \quad (1.20)$$

therefore the *saturation intensity*  $I_s$  can be defined the as:

$$I_s(\omega) = \frac{\hbar\omega A_{21}}{2\sigma(\omega)}; \quad I_s(\omega_A) = I_s = \frac{\pi \hbar c}{3} \frac{\gamma}{\lambda^3}. \quad (1.21)$$

For  $I(\omega) = I_s(\omega_A)$  the numeric density of the two states assumes the form  $N_1 - N_2 = \frac{1}{2}N$ . From EQ. 1.13 it can be defined the *saturation parameter*  $s = I/I_s$  and again from  $N_1 + N_2 = N$  it can be obtained:

$$s = \frac{I}{I_s} = \frac{2\Omega^2}{\gamma^2} \quad (1.22)$$

therefore the radiative force (EQ. 1.14) can be written in the more friendly form:

$$\mathbf{F}_r = \hbar \mathbf{k} \frac{\gamma}{2} \frac{s}{1 + s + 4 \frac{\delta^2}{\gamma^2}}. \quad (1.23)$$

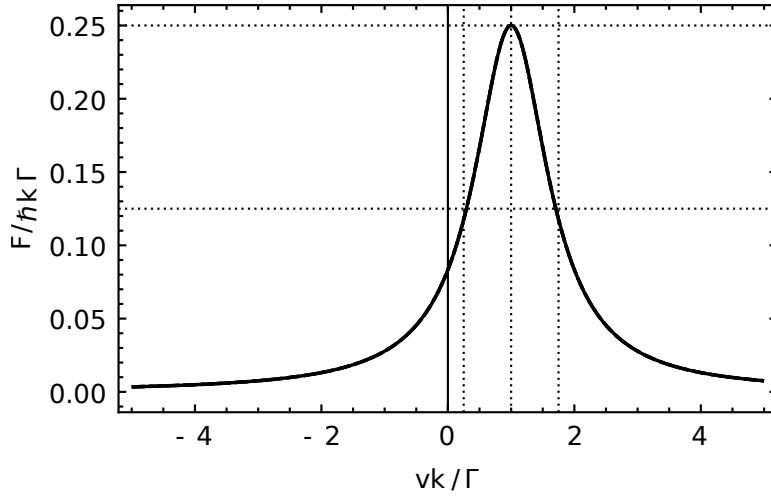


FIGURE 1.1: Velocity dependence of the radiative force EQ. 1.28 for  $I/I_S = 1$ ;  $\delta = -\gamma$ .  $\mathbf{k}$  and  $\mathbf{v}$  have the same direction.

### 1.3 RADIATIVE FORCE AND DOPPLER EFFECT

The expression for the radiative force EQ. 1.14 was obtained considering the atom at rest (with respect to the laser source). Taking into account the motion of an atom implies that Doppler effect has to be considered. For sake of simplicity EQ. 1.14 will be reported below in the form:

$$\mathbf{F}_R = \hbar \mathbf{k} \frac{\gamma}{2} \frac{s}{1 + s + 4 \frac{(\omega - \omega_A)^2}{\gamma^2}}. \quad (1.24)$$

Note that this expression reaches its maximum at resonance and, increasing the laser intensity, the force saturate to

$$\mathbf{F}_{MAX} = \hbar \mathbf{k} \frac{\gamma}{2}. \quad (1.25)$$

If the atom is moving with a velocity  $\mathbf{v}$  being  $\mathbf{k}$  the wave vector of the laser beam, because of the Doppler, effect the laser frequency becomes

$$\omega'_L = \omega_L \left(1 - \frac{\mathbf{v}}{c} \cos(\phi)\right) \quad (1.26)$$

where  $\phi$  is the angle between  $\mathbf{v}$  and  $\mathbf{k}$ . This expression can be written in a more convenient form as

$$\omega' = \omega - \mathbf{k} \cdot \mathbf{v} \quad (1.27)$$

and, reminding that  $\delta = \omega - \omega_A$ , we have  $\omega' - \omega_A = \delta - \mathbf{k} \cdot \mathbf{v}$ . Therefore, for an atom in motion, the expression of the force becomes

$$\mathbf{F}_R = \hbar \mathbf{k} \frac{\gamma}{2} \frac{s}{1 + s + 4 \frac{(\delta - \mathbf{k} \cdot \mathbf{v})^2}{\gamma^2}} \quad (1.28)$$

resulting in a force that, at a given intensity, reaches its maximum when  $\delta + kv = 0$ , i.e. when  $\omega - \omega_A + kv = 0$ .

The force assumes half its maximum value at  $v = -\frac{\delta}{k} \pm \frac{1}{2} \frac{\gamma}{k} \sqrt{1+s}$  resulting in a full width at half maximum FWHM of

$$\text{FWHM} = \frac{\gamma}{k} \sqrt{1+s} \quad (1.29)$$

as can be seen in FIG. 1.1.

### 1.3.1 1D OPTICAL MOLASSES

Consider the case of two counter propagating, collinear and red detuned laser beams (i.e.  $\omega - \omega_A < 0$ ) and an atom forced to move along their common direction. In this condition, due to Doppler effect, the difference  $\omega' - \omega_A$  is reduced for the beam propagating in the opposite direction of the velocity of the atom and increased for the other beam therefore the force component (EQ. 1.28) opposite to the velocity  $\mathbf{v}$  is always more intense than the one in the direction of  $\mathbf{v}$  resulting in a slowing of the atom.

For the sake of clarity let's suppose the atom moving through the positive  $\hat{z}$  direction and consider the laser beam propagating in the negative  $\hat{z}$  direction, the arising force is then described by EQ. 1.28:

$$F_- = -\hbar k \frac{\gamma}{2} \frac{s}{1+s+4\frac{(\delta+kv)^2}{\gamma^2}}. \quad (1.30)$$

On the other hand, the laser beam propagating in the positive  $\hat{z}$  direction generates a force given by

$$F_+ = +\hbar k \frac{\gamma}{2} \frac{s}{1+s+4\frac{(\delta-kv)^2}{\gamma^2}} \quad (1.31)$$

and the resulting force is the sum  $F = F_+ + F_-$ , resulting in

$$F = \hbar k \frac{\gamma}{2} s \frac{16\frac{\delta kv}{\gamma^2}}{(1+s)^2 + 8\frac{\delta^2 + k^2 v^2}{\gamma^2}(1+s) + 16\frac{(\delta^2 - k^2 v^2)^2}{\gamma^4}} \quad (1.32)$$

In this form, is quite useless (the graph is reported in FIG. 1.2) but neglecting the term  $(\frac{k}{\gamma}v)^2 = (2\pi\frac{v}{\gamma c})^2$  and higher orders it becomes

$$F_{\text{OM}} = \frac{\hbar k^2}{\gamma} s \frac{8\delta v}{(1+s+4\frac{\delta^2}{\gamma^2})^2}. \quad (1.33)$$

If  $\omega < \omega_A$ , and in this case the laser is said to be *red detuned*, it results  $\delta < 0$  so that the force  $F_{\text{OM}}$  in EQ. 1.33 is a damping force that can be written in the more convenient form:

$$F_{\text{OM}} = -\beta v; \quad \beta = \frac{\hbar k^2}{\gamma} s \frac{8|\delta|}{(1+s+4\frac{\delta^2}{\gamma^2})^2}. \quad (1.34)$$

At a given detuning  $\delta$ ,  $\beta$  is constant and doesn't depend on the velocity  $v$  so the equation of motion of the atom is

$$M\dot{v} = -\beta v \quad \Rightarrow \quad v(t) = v(0) e^{-\frac{\beta}{M}t} \quad (1.35)$$

$v(t)$  seems to vanish (and the temperature seems to reach  $T = 0$  K) quite quickly disregarding any atom initial velocity, but this is not the case. There are in fact a lower velocity limit and thus a lower temperature limit, as discussed below.

This whole description isn't valid for any initial velocity as EQ. 1.34 could indicate given the linear dependence of  $F_{\text{OM}}$  by  $v$  (for example in FIG. 1.1 it can be seen how the force actually depends on the velocity). This arises from the assumption that has been made to obtain EQ. 1.33. The whole expression of the force, EQ. 1.32, plotted in FIG. 1.2 is quite linear in  $z$  around  $v \frac{k}{\gamma} \approx 0$  while decreases and vanishes after reaching the maximum. From EQ. 1.29 and FIG. 1.2, if  $I \ll I_s$ , one can define the molasses capture velocity as  $v_C = \frac{\gamma}{k}$  and the model depicted is valid for  $v < v_C$ .

Furthermore, there is a lower temperature limit that can be achieved: considering an atom at rest, after absorbing or emitting a photon, the momentum conservation law implies that the atom isn't at rest anymore but has to fulfill  $\hbar\mathbf{k} + \mathbf{P}_{\text{ATM}} = 0$ , therefore its kinetic energy changes due to the recoil by  $\Delta E_R = \frac{\mathbf{p}^2}{2M} = \frac{\hbar^2 k^2}{2M}$  and so, for the absorption and emission processes we have respectively  $\Delta E_{\text{ABS}} = \hbar\omega_A + \Delta E_R$  and  $\Delta E_{\text{EM}} = \hbar\omega_A - \Delta E_R$  so that the energy exchanged with the laser after an absorption and an emission is  $\Delta E = \Delta E_{\text{ABS}} - \Delta E_{\text{EM}} = 2\Delta E_R$ .

Due to the randomness of spontaneous emission this process actually turns in a heating of the atoms. Recalling the scattering rate from EQ. 1.23 and considering the two beams, the heating power can be expressed by:

$$P_{\text{HEAT}} = 4\Delta E_R \frac{\gamma}{2} \frac{s}{1 + s + 4\frac{\delta^2}{\gamma^2}}. \quad (1.36)$$

On the other hand, the power dissipated by the dumping force (EQ. 1.33) is  $F_{\text{OM}} \frac{ds}{dt} = F_{\text{OM}} v = -\beta v^2$  and at the equilibrium the sum of the two has to vanish:  $P_{\text{HEAT}} - \beta v^2 = 0$ . Substituting  $\beta$  with its expression (EQ. 1.33) for the squared velocity we have  $v^2 = \frac{1}{M} \frac{\hbar\gamma^2}{8\delta} (1 + s + 4\frac{\delta^2}{\gamma^2})$ . For small intensity,  $I \ll I_s$ , and taking into account the equipartition theorem in a 1D case ( $E_{\text{CIN}} = \frac{1}{2} k_B T$ ) an expression for the temperature can be obtained:

$$T = \frac{\hbar\gamma}{8k_B} \left( \frac{\gamma}{|\delta|} + 4\frac{|\delta|}{\gamma} \right). \quad (1.37)$$

This expression has a minimum in  $\delta = -\frac{\gamma}{2}$ , the minimum is called the *Doppler temperature*  $T_D$  and its value is:

$$T_D = \frac{\hbar\gamma}{2k_B}. \quad (1.38)$$

## 1.4 RADIATIVE FORCE AND ZEEMAN EFFECT

As can be seen in FIG. 1.1, the radiative force (EQ. 1.28) is different from 0 only in a narrow region across  $v = -\frac{\delta}{k}$  (see EQ. 1.29) resulting in a poor slowing capability: if the laser is chosen to

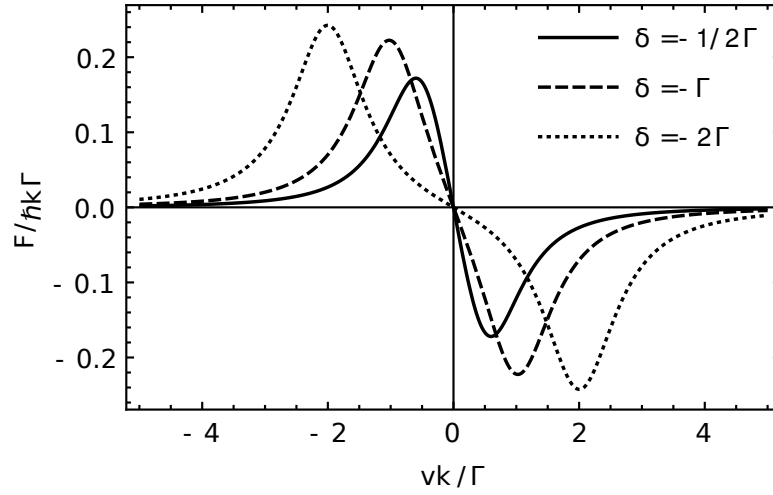


FIGURE 1.2: Velocity dependence of the optical molasses force EQ. 1.32 for  $lI_s = 1$  and for different values of red detuning.

be resonant for a certain velocity, the more the atoms are slowed the more the laser becomes off resonant with the atomic transition and so the force vanishes.

If one wants the force to be resonant in a large range of velocities, as it is in the case for example for slowing down an atomic beam, an usual method to overcome this is to use the Zeeman effect to keep the laser and the atomic transition tuned.

Consider a transition where the angular momentum changes from a ground state with  $J = 0$  to an excited state with  $J' = 1$  so that  $^1 \Delta J_z = -1, 0, 1$ . In the presence of a magnetic field along the  $\hat{z}$  direction, the excited state energy level is split in three different sublevels, corresponding to the three values  $\Delta J_z$ . The atomic frequency  $\hbar\omega_A^{(0)} = E_2 - E_1$ , then becomes

$$\omega_A = \omega_A^{(0)} + \mu_B \frac{\Delta J_z B}{\hbar} \quad (1.39)$$

where  $\mu_B$  is the *Bohr magneton*. The force expression is

$$F_{zs} = \hbar k \frac{\gamma}{2} \frac{s}{1 + s + \frac{4}{\gamma^2} (\delta + kv - \mu_B \frac{\Delta J_z B(z)}{\hbar})^2} \quad (1.40)$$

valid for the case of atom velocity opposite to the laser wave vector, both aligned with the magnetic field along  $\hat{z}$ .

With an appropriate magnetic field variation along  $z$  the atom and the laser can be kept in resonance even for large velocity variations. From the previous EQ. 1.40 the resonance condition is  $\omega - \omega_A^{(0)} + kv - \mu_B \frac{\Delta J_z B(z)}{\hbar} = 0$  therefore  $B(z)$  has to fulfill the relation

$$B(z) = \frac{\hbar k}{\mu_B \Delta J_z} v(z) + \frac{\hbar}{\mu_B \Delta J_z} \delta. \quad (1.41)$$

In order to determine  $B(z)$  one needs the expression for  $v(z)$  while the last term in EQ. 1.41 is constant and will not be considered. Solving the equation of motion isn't easy because of the

<sup>1</sup>Here the Landè factors are omitted.

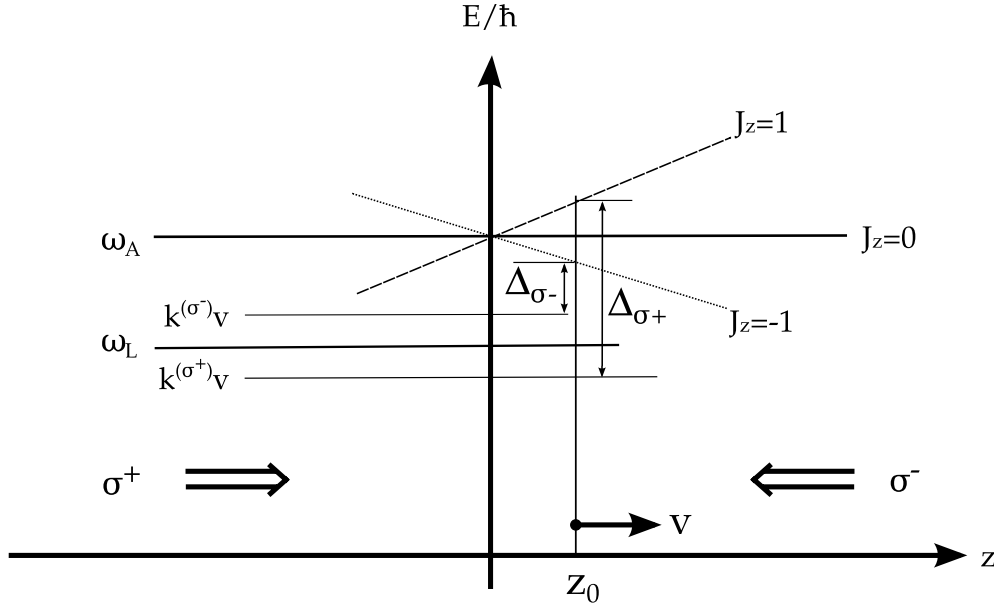


FIGURE 1.3: Scheme for energy levels shift for an atom in position  $z_0$  moving toward  $\hat{z}$  with velocity  $v$  in presence of a magnetic field of the form  $B = bz$ . Notation  $\sigma^+$  and  $\sigma^-$  stand respectively for the polarization beams increasing and decreasing  $J_z$  by  $\hbar$ ;  $k^{(\sigma^+)}$  and  $k^{(\sigma^-)}$  are referred to the wave vectors of the two beams.

velocity dependent force  $F_{zs}(v)$  (EQ. 1.40). To overcome this difficulty it can be chosen to have a constant acceleration  $a = \eta a_{\text{MAX}} = \frac{\eta}{M} \frac{\hbar \gamma}{2}$ , with  $\eta < 1$ , resulting in a constant force. With this approximation we obtain  $\frac{1}{2} M v_0^2 = \eta \frac{\hbar k \gamma}{2} z_0$  where  $v_0$  is the initial velocity of the atom and  $z_0$  is the distance at which the atom is stopped, while for  $v(z)$ :

$$v(z) = v_0 \sqrt{1 - \frac{z}{z_0}} \quad \Rightarrow \quad B(z) = \frac{\hbar k}{\mu_B \Delta J_z} v_0 \sqrt{1 - \frac{z}{z_0}} + \frac{\hbar \delta}{\mu_B \Delta J_z}. \quad (1.42)$$

All atoms having velocity  $v < v_0$  will be resonant with the laser beam at a certain  $z$  and so will be slowed while atoms with velocity  $v > v_0$  are never resonant and so won't be slowed. This will actually turns out in a cooling of the atomic beam because there is an actual increase of the atomic velocity distribution around the final velocity.  $\eta$  is a security a factor that can be chosen experimentally in order to compensate the difference between the real and the maximum acceleration.

#### 1.4.1 MAGNETO OPTICAL TRAP

The technique described so far allows slowing and cooling atoms or atomic beams but neither one is able to confine atoms. This result can be achieved with an optical molasses, arranged with opportune polarization, and a non constant magnetic field, the so-called *magneto-optical trap* (MOT) [30].

We illustrate here the basic working principle of a MOT. For the sake of simplicity let's consider the case of an atom in position  $z_0$  moving with a velocity  $v\hat{z}$ , the case of two beams separately and suppose the magnetic field to take the expression

$$B = bz \quad \mathbf{b} = \nabla B_z \Big|_{z=0} \quad (1.43)$$

where  $\mathbf{b}$  is the field gradient

As in EQ. 1.40, there is a change in the atomic and laser frequencies difference as shown in FIG. 1.3. For the  $\sigma^+$  and  $\sigma^-$  polarized beams, their detuning  $\Delta$  can be written respectively:

$$\Delta_{\sigma^+} = \delta + kv + \mu_B \frac{bz}{\hbar} \quad \Delta_{\sigma^-} = \delta - kv - \mu_B \frac{bz}{\hbar}. \quad (1.44)$$

Inserting this quantities in EQ. 1.23, we obtain

$$F_{\sigma^+} = \hbar k \frac{\gamma}{2} \frac{s}{1 + s + 4\left(\frac{\Delta_{\sigma^+}}{\gamma}\right)^2}; \quad F_{\sigma^-} = -\hbar k \frac{\gamma}{2} \frac{s}{1 + s + 4\left(\frac{\Delta_{\sigma^-}}{\gamma}\right)^2} \quad (1.45)$$

and, as in the optical molasses case, the resulting force is given the sum  $F_{\text{MOT}} = F_{\sigma^+} + F_{\sigma^-}$ . Performing the same approximations as before one obtains

$$F_{\text{MOT}} = -8 \frac{\hbar k}{\gamma} s \frac{|\delta|(kv + \frac{\mu_B b}{\hbar} z)}{\left(1 + s + 4\frac{\delta^2}{\gamma^2}\right)^2}. \quad (1.46)$$

This expression resembles  $F_{\text{OM}}$  (EQ. 1.33) except for the  $z$  linear term that represent a damped harmonic oscillator. Defining

$$\beta = s \frac{8\hbar k^2 |\delta|}{\gamma(1 + s + 4\frac{\delta^2}{\gamma^2})^2}; \quad \mathcal{K} = s \frac{8\mu_B k |\delta| \mathbf{b}}{\gamma(1 + s + 4\frac{\delta^2}{\gamma^2})^2} = \beta \frac{\mu_B}{\hbar k} \mathbf{b} \quad (1.47)$$

we obtain, for an atom moving in the MOT region

$$F_{\text{MOT}} = -\beta v - \beta \frac{\mu_B \mathbf{b}}{\hbar k} z = -\beta v - \mathcal{K} z \quad (1.48)$$

In a classical viewpoint the solution of the equation of motion is

$$z(t) = z(0) e^{-\frac{\gamma_M}{2} t} \cos(\omega_M t) \quad (1.49)$$

i.e. that of a damped harmonic oscillator with a damping rate and frequency oscillation given respectively by:

$$\gamma_M = \frac{\beta}{M}; \quad \omega_M = \sqrt{\frac{\beta}{M} \frac{\mu_B \mathbf{b}}{\hbar k}}. \quad (1.50)$$

## 1.5 DIPOLE FORCE

The interaction energy between the atomic electric dipole moment  $\mathbf{d}$  induced by an electric field  $\mathbf{E}$  and the field itself is given by  $U = -\frac{1}{2}\mathbf{d} \cdot \mathbf{E}$ . Using EQ. 1.11 and  $\mathbf{E} = \hat{\mathbf{x}}E_0(z) \cos(\omega t - kz)$  and taking the average over the time the expression of the force becomes [11]:

$$F = -\nabla U = -e \frac{\langle 1|x|2 \rangle}{2} \left( u \frac{\partial E_0}{\partial z} - \nu E_0 k \right) \quad (1.51)$$

Substituting the expressions for  $u$  and  $\nu$  EQ. 1.12 and taking into account EQ. 1.8 the force can be divided in two terms:

$$F_D = -\frac{\hbar\delta}{2} \frac{1}{1 + \frac{I}{I_s} + 4\left(\frac{\delta}{\gamma}\right)^2} \frac{1}{I_s} \frac{\partial I}{\partial z}; \quad F_R = \hbar k \frac{\gamma}{2} \frac{I}{I_s} \frac{1}{1 + \frac{I}{I_s} + 4\left(\frac{\delta}{\gamma}\right)^2}. \quad (1.52)$$

The second term is the radiative force, described in detail in the preceding paragraphs, while  $\mathbf{F}_D$  is the so-called *dipole force*. In the three dimensional case  $\mathbf{F}_D$  is:

$$\mathbf{F}_D = -\frac{\hbar\delta}{2} \frac{1}{1 + \frac{I}{I_s} + 4\left(\frac{\delta}{\gamma}\right)^2} \frac{1}{I_s} \nabla I. \quad (1.53)$$

$F_D$  doesn't saturate by increasing the laser intensity and vanishes for  $\delta = 0$ . Furthermore, while  $\mathbf{F}_R$  has the direction of  $\mathbf{k}$ ,  $\mathbf{F}_D$  has the direction of  $\nabla I$  while the verse depends on  $\delta$  so that for a red detuned laser beam an atom is attracted toward the maximum of the laser intensity.

### 1.5.1 OPTICAL DIPOLE TRAP

To realize an optical dipole trap then, it is sufficient to focus a red detuned laser beam ( $\delta < 0$ ) and, given EQ. 1.53, the atoms will be attracted to the focus itself.

Note that

$$F_D \simeq \frac{1}{\delta} \quad F_R \simeq \frac{1}{\delta^2} \quad \text{for } \delta \rightarrow \infty \quad (1.54)$$

given that  $F_R$  is proportional to the scattering rate of photons, in the end, is responsible for the heating of the atoms as it can be seen in EQ. 1.36. In order to avoid heating, given the asymptotic behaviour of the radiative and the dipole force, very intense and far detuned beam are usually used in optical dipole traps.

The force  $\mathbf{F}_D$  is a conservative force so it can be obtained from  $\mathbf{F}_D = -\nabla V$  with

$$V(\mathbf{r}) = \frac{\hbar\delta}{2} \ln \left( 1 + \frac{I(\mathbf{r})/I_s}{1 + 4\delta^2/\gamma^2} \right) \quad (1.55)$$

where the integrating constant is chosen so that  $V = 0$  for  $I = 0$ .

For a far red detuned beam,  $|\delta| \gg \gamma$ , using  $\log(1+x) \simeq x$ ,  $\frac{\gamma^2}{\gamma^2 + 4\delta^2} \simeq \frac{\gamma^2}{4\delta^2}$  and with the  $I_s$  definition (EQ. 1.21) the previous formula can be simplified as:

$$V(\mathbf{r}) \simeq \frac{\hbar\delta}{2} \left( \frac{\gamma^2}{\gamma^2 + 4\delta^2} \right) \frac{I(\mathbf{r})}{I_s} \simeq \frac{3\pi c^2}{2\omega_A^3} \frac{\gamma}{\delta} I(\mathbf{r}) \quad (1.56)$$

For a gaussian beam propagating along the  $z$  axis the intensity is:

$$I(x, y, z) = \frac{2P}{\pi w^2(z)} e^{-\frac{2(x^2+y^2)}{w^2(z)}} \quad (1.57)$$

where  $w(z) = w_0 \sqrt{1 + \left(\frac{z}{z_R}\right)^2}$ ;  $z_R = \frac{\pi w_0^2}{\lambda}$  and  $P$  is the power of the laser. For low temperatures  $k_B T < V(0)$ ,  $r \ll w_0$  and  $z \ll z_R$ , and using  $e^{-x} \simeq 1 - x$  and  $\frac{1}{1+x^2} \simeq 1 - x^2$  the potential results in [13]:

$$V_D(\mathbf{r}) \simeq \frac{3\pi c^2 \gamma}{2\omega_A^3 \delta} \frac{2P}{\pi w_0^2} \left(1 - \frac{2}{w_0^2}(x^2 + y^2) - \frac{1}{z_R^2} z^2\right) = V_D \left(1 - \frac{2}{w_0^2}(x^2 + y^2) - \frac{1}{z_R^2} z^2\right) \quad (1.58)$$

that is said an harmonic 3D potential summed to a constant.

### 1.5.2 SPATIAL DISTRIBUTION OF ATOMS IN AN OPTICAL DIPOLE TRAP

Again in the case of a gaussian laser beam propagating along the  $\hat{z}$  direction (EQ. 1.57), the classical Hamiltonian of an atom of mass  $M$  moving in the potential of EQ. 1.58 can be written as

$$H = \frac{\mathbf{P}^2}{2M} + \frac{1}{2} M (\omega_x^2 x^2 + \omega_y^2 y^2 + \omega_z^2 z^2) \quad \text{with} \quad \omega_{x,y}^2 = \frac{4V_D}{Mw_0^2}; \quad \omega_z^2 = \frac{2V_D}{Mz_R^2}. \quad (1.59)$$

Using the Boltzmann statistic the trapped atom density  $n(\mathbf{r})$  as a function of  $\mathbf{r} = (x, y, z)$  is:

$$n(x, y, z) = N \left( \frac{M}{2\pi k_B T} \right)^{\frac{3}{2}} \omega_x \omega_y \omega_z e^{-\frac{1}{k_B T} \frac{M}{2} (\omega_x^2 x^2 + \omega_y^2 y^2 + \omega_z^2 z^2)} \quad (1.60)$$

and defining

$$\sigma_{x,y,z}^2 = \frac{k_B T_{x,y,z}}{M\omega_{x,y,z}^2}; \quad n_0 = \frac{N}{(2\pi)^{3/2}} \frac{1}{\sigma_x \sigma_y \sigma_z} \quad (1.61)$$

the atom density distribution is

$$n(x, y, z) = n_0 e^{-\left(\frac{x^2}{2\sigma_x^2} + \frac{y^2}{2\sigma_y^2} + \frac{z^2}{2\sigma_z^2}\right)} \quad (1.62)$$

with  $n_0$  the *peak density*.

## 1.6 EVAPORATIVE COOLING

The scattering force  $F_R$  permits to slow and cool atoms and, combined with the Zeeman shift of the atomic levels, can be used over a wide range of velocities but the lower limit of the

temperature that can be achieved is determined by the spontaneous emission process and by the *recoil kinetic energy*  $E_R = \hbar^2 k^2 / 2M$  i.e. the kinetic energy acquired by an atom after a spontaneous emission event. On the other hand, in a far red detuned optical dipole trap, photons scattering is avoided (EQ. 1.54) but, given the conservative nature of the trapping force EQ. 1.58, this kind of traps can't be used to dissipate the kinetic energy of the atoms.

Evaporative cooling permits to cool the atomic sample at the cost of atom losses. In a finite depth ( $U_0$ ) potential well, atoms with higher kinetic energy are more likely to leave the trap and, as a results, the temperature of the atomic cloud, formed by the remaining atoms with lower average kinetic energy, is lowered. This is called the *static evaporation* because the potential well depth  $U_0$  remains constant. In this configuration, the more the atomic cloud is cooled the less probable that an atom with "high" kinetic energy will leave the trap is. For this reason, the trap depth  $U_0$  is lowered in time and this technique is called *forced evaporative cooling* [16]. For an atomic cloud at a temperature  $T$  so high that the motion of atoms can be considered classical:  $k_B T \gg \hbar \omega_0$  (where  $\omega_0$  is the trap frequency), the process consists in maintaining  $U_0 \simeq \zeta k_B T$ , where  $\zeta > 1$  is an arbitrary constant. In an optical dipole trap this is done by regulating the laser power (see EQ. 1.58). For values of  $\zeta$  of the order or higher than 10, the atomic cloud can be described by a truncated Boltzmann distribution [20] but here, as a good approximation, will be used the Boltzmann distribution as in sec. 1.5.2. In the case of an harmonic potential, atoms that are more likely to leave the trap have an average kinetic energy  $\sim (\zeta + 1)k_B T$  [8] and for the variation of the atomic cloud temperature and the number of atoms can be written the equation [8]:

$$\frac{dT}{T} = \alpha \frac{dN}{N} \quad \Rightarrow \quad \frac{T_f}{T_i} = \left( \frac{N_f}{N_i} \right)^\alpha; \quad \alpha \simeq \frac{\zeta + 1}{3} - 1 \quad (1.63)$$

that shows how, at a cost of some atomic loss the temperature is lowered. This description is valid if a temperature of the atomic cloud can be defined i.e. if atoms have the time to reach the thermodynamic equilibrium through elastic collisions. This is never strictly true (evaporative cooling is a non equilibrium process) but is at least approximately true if  $U_0$  is lowered in a time longer compared to the inverse of the elastic collisional rate  $n\sigma\bar{v}$  and thus the trap frequencies  $\omega_{x,y,z}$  can be considered constant while atoms reach the thermal equilibrium. The elastic collision rate is expressed as a function of the atomic density  $n = N/V$ , the temperature independent elastic collisional cross section  $\sigma$  and the mean velocity  $\bar{v} = \sqrt{3k_B T/M}$ . From EQ. 1.59 and EQ. 1.61 it holds  $V = \sigma_x \sigma_y \sigma_z = (\omega_x \omega_y \omega_z)^{-1} (k_B T/M)^{3/2}$  and as a results the collisional rate scaling law can be expressed as a function of the temperature and, thanks to EQ. 1.63, to the number of atoms. The relevant quantity in all this process, as it will be said in the next section, is the *phase space density* defined as  $\mathcal{D} = n \lambda_{dB}^3$  where  $\lambda_{dB}$  is the thermal de Broglie wavelength. All these quantities can then be described as a function of the number of atoms

$$T \sim N^\alpha; \quad V \sim T^{\frac{3}{2}} = N^{\frac{3}{2}\alpha}; \quad n\sigma\bar{v} \sim N^{1-\alpha}; \quad \mathcal{D} \sim N^{1-3\alpha}. \quad (1.64)$$

In an evaporation where the number of atoms changes from  $N_i$  to  $N_f$ , the phase space density changes from  $\mathcal{D}_i$  to  $\mathcal{D}_f$  and as results of EQ. 1.64 it holds

$$\mathcal{D}_f = \mathcal{D}_i \left( \frac{N_i}{N_f} \right)^{\frac{1-3\alpha}{\alpha}} \quad (1.65)$$

in the evaporative cooling there is a loss of particles thus  $N_i > N_f$  and as a consequence, provided that  $\alpha > 1/3$ , there is a gain in the final phase space density  $\mathcal{D}_f$ . As an example, for  $\zeta = 11$  and thus  $\alpha = 3$ , for  $N_f = 0.1N_i$  we have  $\mathcal{D}_f = 2.37\mathcal{D}_i$ .

A detailed description of the temporal behaviour of the evaporative cooling is beyond the scope of this thesis, here it will be said that as  $\eta$  increases (and as a consequence  $\alpha$ ), an increase in the phase space density requires less atoms to be lost (EQ. 1.65) thus the efficiency of the process increases as well. As a drawback increasing  $\eta$  and hence the potential well depth  $U_0$ , slows the process because it is less probable that an atom acquires an energy high enough to leave the trap. Given that a trap has a finite lifetime, a balance between the cooling efficiency and the time required has to be found empirically.

## 1.7 BOSE-EINSTEIN CONDENSATION

A complete description of the Bose-Einstein condensation is beyond the scope of this thesis, nevertheless the fundamental concepts and the characteristics observed in our experiment so far will be reported here following the description in [8].

### 1.7.1 NON INTERACTING PARTICLES

The simpler starting point to describe the condensation is the case of  $N$  non interacting bosons contained in a box of volume  $V$ . The number of states with energy  $\epsilon_i$  is given by the Bose-Einstein statistics multiplied by the degeneracy of each state ( $g_i$ ) and the sum of all these states must be equal to the number of particles:

$$N = \sum_i g_i \frac{1}{\exp\left(\frac{\epsilon_i - \mu}{k_b T}\right) - 1} = \sum_i g_i \frac{z}{\exp\left(\frac{\epsilon_i}{k_b T}\right) - z} \quad (1.66)$$

where  $\mu$  is the chemical potential and  $z = \exp\left(\frac{\mu}{k_b T}\right)$  the *fugacity* that must satisfy  $0 \leq z < 1$  and, for fixed  $T$  and  $V$ , is an increasing function of  $N$ . The condensation phenomena appears when, at  $T$  and  $V$  fixed, the fugacity  $z$  approaches 1. Considering  $N$  in EQ. 1.66 as the sum of the ground ( $\epsilon_0 = 0$  and non degenerate) state and of the excited states leads to

$$N = N_0 + N_{\text{ex}} = \frac{z}{1 - z} + \sum_{i \neq 0} g_i \frac{z}{\exp\left(\frac{\epsilon_i}{k_b T}\right) - z}. \quad (1.67)$$

For  $T$  and  $V$  fixed,  $N_{\text{ex}}$  is upper bounded, while  $N_0$  isn't and when the population in the excited states is saturated any new particle must occupy the ground state. In the case of particles contained in a box of volume  $V$  it holds  $g_i \rightarrow \frac{4\pi V}{h^3} p^2 dp$  and the sum in EQ. 1.67 can be evaluated resulting in

$$N_{\text{ex}} = \frac{V}{\lambda_{\text{dB}}^3} g_{3/2}(z) \quad \Rightarrow \quad N = N_0 + \frac{V}{\lambda_{\text{dB}}^3} g_{3/2}(z) \quad (1.68)$$

where  $\lambda_{\text{dB}} = \frac{h}{\sqrt{2\pi m k_B T}}$  is the de Broglie wavelength and  $g_{3/2}(z) = \sum_{m=1}^{\infty} \frac{z^m}{m^{3/2}}$  has the maximum for  $z = 1$  and its maximum is 2.612. In order to have  $n_0 = N_0/V \geq 0$  i.e. in order to populate the ground state,  $n = N/V$  must satisfy the relation

$$n\lambda_{\text{dB}}^3(T) \geq 2.612 \quad (1.69)$$

thus the distance between the particles has to be of the order of  $\lambda_{\text{dB}}$ . From its definition,  $\lambda_{\text{dB}}$  is a decreasing function of the temperature then, once the density  $n$  is fixed, the critical temperature  $T_c$  can be defined from  $n\lambda_{\text{dB}}^3(T_c) = 2.612$  and when the temperature is lowered below  $T_c$ , the particles start to accumulate in the ground state. The quantity  $\mathcal{D} = n\lambda_{\text{dB}}$  already encountered in the previous section, is called the phase space density.

In a similar way it can be described the case of non interacting particles in an isotropic harmonic potential. Here the energies are the eigenvalues of the Hamiltonian of a three dimensional harmonic oscillator:  $\epsilon_{\mathbf{n}} = \hbar\omega_{\text{HO}}(n_x + n_y + n_z + \frac{3}{2})$  where  $\omega_{\text{HO}}$  is the oscillator frequency and  $n_x, n_y, n_z \in \mathbb{N}$  and  $\mathbf{n} = (n_x, n_y, n_z)$ . The ground state has an energy  $\epsilon_0 = 3/2\hbar\omega_{\text{HO}}$  and is not degenerate while each eigenstate with given  $n = n_x + n_y + n_z$  has a degeneracy  $g_n = 1/2(n+1)(n+2)$ . As in the previous case it can be written

$$N = N_0 + N_{\text{ex}} = \frac{z}{1-z} + \sum_{n=1}^{\infty} \left( \frac{(n+1)(n+2)}{2} \frac{z}{\exp(\frac{n\hbar\omega_{\text{HO}}}{k_B T}) - z} \right) \quad (1.70)$$

and also in this case the sum in EQ. 1.70 is upper bounded. For  $z = 1$  and in the condition  $\hbar\omega_{\text{HO}} \ll k_B T$  its upper limit can be calculated resulting in [8]:

$$N_{\text{max}} \simeq \left( \frac{k_B T}{\hbar\omega_{\text{HO}}} \right)^3 g_3(1); \quad g_3(1) \simeq 1.2 \quad (1.71)$$

from this equation, posing  $N = N_{\text{max}}$ , it can be defined the critical temperature ( $T_c$ ) and the ground state population for temperatures  $T < T_c$ :

$$T_c \frac{\hbar\omega_{\text{HO}}}{k_B} \left( \frac{N}{g_3(1)} \right); \quad N_0(T) = N \left( 1 - \left( \frac{T}{T_c} \right)^3 \right). \quad (1.72)$$

A system composed by non interacting particles in an harmonic potential, is described by the Hamiltonian

$$H_1 = \sum_i \left[ \frac{\mathbf{p}_i^2}{2M} + V_T(\mathbf{r}_i) \right]; \quad V_T(\mathbf{r}) = \frac{1}{2} M \omega_{\text{HO}}^2 \mathbf{r}_i^2 \quad (1.73)$$

that is the sum of  $N$  independent terms and thus the collective many body wave function  $\psi(\mathbf{r})$  can be written as the tensor product of the single particle wave functions  $\phi(\mathbf{r}_i)$

$$\psi(\mathbf{r}) = |\phi(\mathbf{r}_1)\rangle \otimes |\phi(\mathbf{r}_2)\rangle \otimes \dots \otimes |\phi(\mathbf{r}_N)\rangle \quad (1.74)$$

where  $|\phi(\mathbf{r}_i)\rangle$  are the wave functions of a quantum harmonic oscillator. In this way  $|\psi(\mathbf{r})\rangle$  is symmetric for particle exchange as required for bosons [8] and at  $T = 0$  each single particle wave function is the ground state solution of the harmonic oscillator

$$\phi_0(\mathbf{r}_i) = \left( \frac{M\omega_{\text{HO}}}{\pi\hbar} \right)^{3/4} e^{-\frac{M\omega_{\text{HO}}}{2\hbar} \mathbf{r}_i^2}. \quad (1.75)$$

## 1.7.2 INTERACTING PARTICLES

In the case of interacting bosons, in addition to the trapping potential  $V_T(\mathbf{r})$ , has to be considered the interaction potential  $V(\mathbf{r}_i - \mathbf{r}_j)$  and the many body Hamiltonian results in

$$H = \sum_i \left[ \frac{\mathbf{p}_i^2}{2M} + V_T(\mathbf{r}_i) + \frac{1}{2} \sum_{j \neq i} V(\mathbf{r}_i - \mathbf{r}_j) \right] = \sum_i \left[ H_1(\mathbf{r}_i) + \frac{1}{2} \sum_{j \neq i} V(\mathbf{r}_i - \mathbf{r}_j) \right]. \quad (1.76)$$

The ground state many body wave function is again taken in the form EQ. 1.74 that satisfies the symmetry required for bosons but the single particle wave functions  $\phi(\mathbf{r}_i)$  have to be found. Instead of finding the eigenfunctions of EQ. 1.76 is used a variational method: the many body wave function,  $\psi(\mathbf{r})$ , must minimize the Hamiltonian matrix element with the constrain  $\langle \psi(\mathbf{r}) | \psi(\mathbf{r}) \rangle = 1$  and, using the Lagrange multipliers method, has to be a solution of  $\langle \delta \psi | H | \psi \rangle - \mu \langle \delta \psi | \psi \rangle + \langle \psi | H | \delta \psi \rangle - \mu \langle \psi | \delta \psi \rangle = 0$ . The two terms in  $\psi^*$  and  $\psi$  are considered to be independent so only the first two terms in the previous equation remain. Substituting EQ. 1.74 and using the Hamiltonian expression EQ. 1.76 and remembering that for  $N$  bosons at  $T = 0$  all the single particle wave function  $\phi(\mathbf{r}_i)$  are identical, the problem becomes a single particle problem in the form [8]

$$H_1(\mathbf{r})\phi(\mathbf{r}) + N \left( \int V(\mathbf{r} - \mathbf{r}')\phi(\mathbf{r}') d\mathbf{r}' \right) \phi(\mathbf{r}) = \mu\phi(\mathbf{r}). \quad (1.77)$$

This expression is valid for low density gasses, EQ. 1.74 implies that correlations between particles are not taken into account. In this condition, the interaction between particles is described by the asymptotic behaviour of the wave function. Furthermore, in the case of ultracold particles, collisions happen at very low energy. Expanding the scattering wave function of two particles interacting through the potential  $V(\mathbf{r} - \mathbf{r}')$  in spherical harmonics, the lowest energy solution is the  $\ell = 0$  one. In this approximation the interaction potential can be replaced by a pseudo potential in the form [8]:

$$V_{ps} = \frac{4\pi\hbar^2}{M} a_s \delta(\mathbf{r} - \mathbf{r}') \quad (1.78)$$

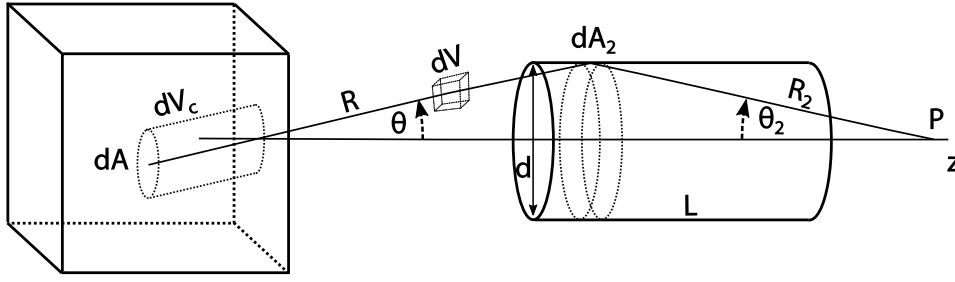
where  $a_s$  is the  $s$ -wave *scattering length*. Substituting  $V_{ps}$  in EQ. 1.77 we find the Gross-Pitaevskii equation:

$$-\frac{\hbar^2}{2M} \nabla^2 \phi(\mathbf{r}) + V_T(\mathbf{r})\phi(\mathbf{r}) + Ng |\phi(\mathbf{r})|^2 = \mu\phi(\mathbf{r}); \quad g = \frac{4\pi\hbar^2}{M} a_s \quad (1.79)$$

that describes the static ground state of an interacting Bose-Einstein condensate. Substituting the pseudo potential to the interaction potential in EQ. 1.77 it can be shown that the energy of the ground state depends explicitly on the particles number  $N$  and the Lagrange multiplier  $\mu$  in EQ. 1.79 is the chemical potential of the condensate.

In order to obtain an explicit expression of a solution of EQ. 1.79 in the case of an harmonic trapping potential EQ. 1.73, the ground state wave function of an harmonic oscillator EQ. 1.75 is used as a model in the so called *Gaussian ansatz*:

$$\phi(\mathbf{r}) = \frac{1}{\pi^{3/4} \sqrt{w^3 a_{HO}^3}} e^{-\frac{r^2}{2w^2 a_{HO}^2}} \quad (1.80)$$

FIGURE 1.4: Scheme of the oven. The  $\varphi$  angle is omitted.

where  $a_{\text{HO}} = \sqrt{\hbar/M\omega_{\text{HO}}}$  is the width of the ground state wave function of the harmonic oscillator and  $w$  a numeric parameter.

In the Gaussian ansatz it can be found that the energy of the ground state is given by [8]:

$$E(w) = N\omega_{\text{HO}} \left( \frac{3}{4} \frac{1}{w^2} + \frac{3}{4} w^2 + \frac{1}{\sqrt{2\pi}} \frac{a_s N}{a_{\text{HO}}} \frac{1}{w^3} \right) \quad (1.81)$$

where the three terms are respectively the kinetic energy, the potential energy in the trap potential and the energy due to the interactions. If  $\frac{Na_s}{a_{\text{HO}}} \gg 1$  the kinetic energy of the particles can be ignored and the Gross-Pitarvskii equation EQ. 1.79, in the Thomas-Fermi limit, reduces to

$$V_{\text{T}}(\mathbf{r}) + Ng|\phi(\mathbf{r})|^2 = \mu \quad \Rightarrow \quad n(\mathbf{r}) = \frac{1}{g} \left( \mu - \frac{1}{2} M\omega_{\text{HO}}^2 r^2 \right) \quad (1.82)$$

thus, in the Thomas-Fermi limit, the particle density  $n(\mathbf{r}) = N|\phi(\mathbf{r})|^2$  has the shape of a parabola. This last equation is one of the characteristics that can be easily observed experimentally that indicates when Bose-Einstein condensation occurs and it is valid even in the case of dipolar Bose-Einstein condensates [18].

## 1.8 ATOMIC BEAM

The starting point of the experiment is the slowing of an atomic beam of dysprosium, hence it will be reported a brief description of the atomic beam consisting of free particles emerging from an oven depicted as a box of volume  $V$  at a certain temperature  $T$  with a circular hole on a wall submerged in the vacuum.

Assuming the box as a closed box, the number of particle in the vapor is proportional to the vapor pressure itself. Vapor pressure of dysprosium has been studied in [24] and can be expressed as

$$P = e^{\mathcal{B} - \frac{\mathcal{A}}{T}} \quad (1.83)$$

where  $\mathcal{A} = 35170/\text{K}$  and  $\mathcal{B} = 20.56$  for temperature in the 1239–1534 K range.

Assuming the particle number  $N$  proportional to the vapor pressure and considering dysprosium atoms as hard spheres, their energy is the kinetic energy  $E = \frac{1}{2}Mv^2$  and from the Boltzmann statistic it follows that

$$n(\mathbf{v}) = \frac{N}{V} \left( \frac{2\pi k_B T}{M} \right)^{-\frac{3}{2}} e^{-\frac{1}{2} \frac{Mv^2}{k_B T}} \quad (1.84)$$

and the Maxwell-Boltzmann distribution for the modulus of the velocity is

$$f(v) = 4\pi \left( \frac{2\pi k_B T}{M} \right)^{-\frac{3}{2}} v^2 e^{-\frac{1}{2} \frac{Mv^2}{k_B T}}. \quad (1.85)$$

The atoms emerging from the aperture  $dA$  with velocity  $v$  are those contained in the cylinder of volume  $dV_C = v \cos\theta dt dA$  and because the EQ. 1.84 doesn't depend on the angle, atoms in the solid angle  $\sin\theta d\theta d\varphi$  have to be considered. The resulting atom flux through the aperture is

$$\frac{dN(v, \theta, \varphi)}{dt} = n_0 \frac{\cos\theta \sin\theta d\theta d\varphi}{4\pi} \pi \left( \frac{2\pi k_B T}{M} \right)^{-\frac{3}{2}} v^3 e^{-\frac{1}{2} \frac{Mv^2}{k_B T}} dA \quad (1.86)$$

integrating for  $\theta \in (0, \frac{\pi}{2})$  and  $\varphi \in (0, 2\pi)$  it results in the velocity distribution of the atomic flux:

$$\frac{dN(v)}{dt} = \pi n_0 \left( \frac{2\pi k_B T}{M} \right)^{-\frac{3}{2}} v^3 e^{-\frac{1}{2} \frac{Mv^2}{k_B T}} dA \quad (1.87)$$

and the most probable velocity therefore is

$$v_{MP} = \sqrt{3 \frac{k_B T}{M}}. \quad (1.88)$$

The atomic density in the volume element  $dV = R^2 \sin\theta d\theta d\varphi dR$  in FIG. 1.4 is given by

$$\frac{dN}{dV} = n_0 \frac{\cos\theta dA}{R^2} \left( \frac{2\pi k_B T}{M} \right)^{-\frac{3}{2}} v^2 e^{-\frac{1}{2} \frac{Mv^2}{k_B T}} \quad (1.89)$$

and integrating over  $v \in (0, \infty)$  it becomes [28]

$$n(\theta, \varphi) = n_0 \frac{dA}{4\pi R^2} \cos\theta \quad (1.90)$$

and then the atomic density in  $dV$  is obtained integrating EQ. 1.90 over the area  $dA$ . Assuming that in the channel represented in FIG. 1.4 atoms are reflected by the walls with the same angle dependence as EQ. 1.90 and that no atoms are trapped by the walls the particle density can be obtained integrating EQ. 1.90 on the aperture  $dA$  (for the particles arriving at  $P$  without hitting the channel) and over  $dA_2(z)$  along the  $z$  axis:

$$n(z) = \int_A n_0 \frac{dA}{4\pi R^2} \cos\theta dA + \iint_{A_2} n(z') \frac{dA_2}{4\pi R_2^2} \cos\theta_2 dA_2 dz'. \quad (1.91)$$

An approximate expression for the wall collision rate  $v(z)$  has been found [28]:

$$v(z) = v_0 \left( 1 - \alpha(\beta) - (1 - 2\alpha(\beta)) \frac{z}{L} \right) \quad (1.92)$$

TABLE 1.1: *Dysprosium has seven stable isotopes with mass number 154, 156, 158, 160–164,  $^{154}\text{Dy}$  is artificial. The two most abundant isotopes are  $^{162}\text{Dy}$  and  $^{164}\text{Dy}$  which, together with  $^{160}\text{Dy}$  are bosons;  $^{161}\text{Dy}$  and  $^{163}\text{Dy}$  are fermions. The relative abundance of  $^{156}\text{Dy}$  and  $^{158}\text{Dy}$  is below 1%. Data from [27].*

Isotope	Abundance [%]	Spin
$^{160}\text{Dy}$	2.34	0
$^{161}\text{Dy}$	18.9	5/2
$^{162}\text{Dy}$	25.5	0
$^{163}\text{Dy}$	24.9	5/2
$^{164}\text{Dy}$	28.2	0

where  $\beta = \frac{d}{L}$  and  $\alpha(\beta) \rightarrow 2/3\beta$  for  $L \gg d$  and  $\alpha(\beta) \rightarrow 1/2(1 - \beta)$  for  $d \gg L$ . With  $v(z)$  the integral in EQ. 1.91 can be solved resulting in the expression for the atomic flux at a given angle  $I(\varphi)$ :

$$I(\varphi)d\omega = v_0 \frac{A}{\pi} j(\varphi)d\omega \quad (1.93)$$

where  $A = \pi/4d^2$  is the area of the channel,  $d\omega$  is the solid angle of observation and  $j(\varphi)$  is a function defined differently for  $\tan(\varphi) < d/L$  or  $\tan(\varphi) \geq d/L$ , i.e. depending on which of the two terms in EQ. 1.91 is dominating. The first term (when  $\tan(\varphi) < d/L$ ) concerns particles that aren't reflected by the channel walls and the second one ( $\tan(\varphi) \geq d/L$ ) when reflected particles are the majority.

The collision rate  $v(z)$  can be substituted by the atom density  $n(z)$  (the number of collision is proportional to the number of particles present) and writing all the various parts together we have an expression for the atom density at a given angle of observation given by:

$$I(\varphi)d\omega \propto (e^{\mathcal{B} - \frac{d}{T}}) \frac{A}{\pi} j(\varphi)d\omega \quad (1.94)$$

## 1.9 DYSPROSIUM

Dysprosium [Dy] is a rare earth element with atomic number 66 and seven stable isotopes (TAB. 1.1). Its electronic configuration is  $[\text{Xe}]4f^{10}6s^2$  and the ground state has angular momentum  $J = 8$  ( $L = 6$ ,  $S = 2$ ) and the magnetic moment of the ground state is  $\mu = 9.93\mu_B$  [22] is the highest among the natural elements. Its melting point is 1680 K and thus to reach suitable atomic effusive flux dysprosium is usually heated at around 1200 °C.

The complex electronic structure of Dy allows many quasi-cycling transitions. The strongest one, with linewidth 32 MHz, is the one at 421 nm. In our experiment it is used for the atomic beam collimation and slowing respectively in the transverse cooling and Zeeman Slower stages. Nevertheless, being the Doppler temperature associated with this transition very large ( $T_{D-421} = 774\mu\text{K}$ ), a second, narrower, optical transition at 626 nm has been used for the MOT trapping. Here, the reduced linewidth (136 kHz) guarantees a Doppler Temperature of  $T_{D-626} = 3.3\mu\text{K}$  suitable for direct loading of the atoms in an optical dipole trap at the cost of a reduced capture

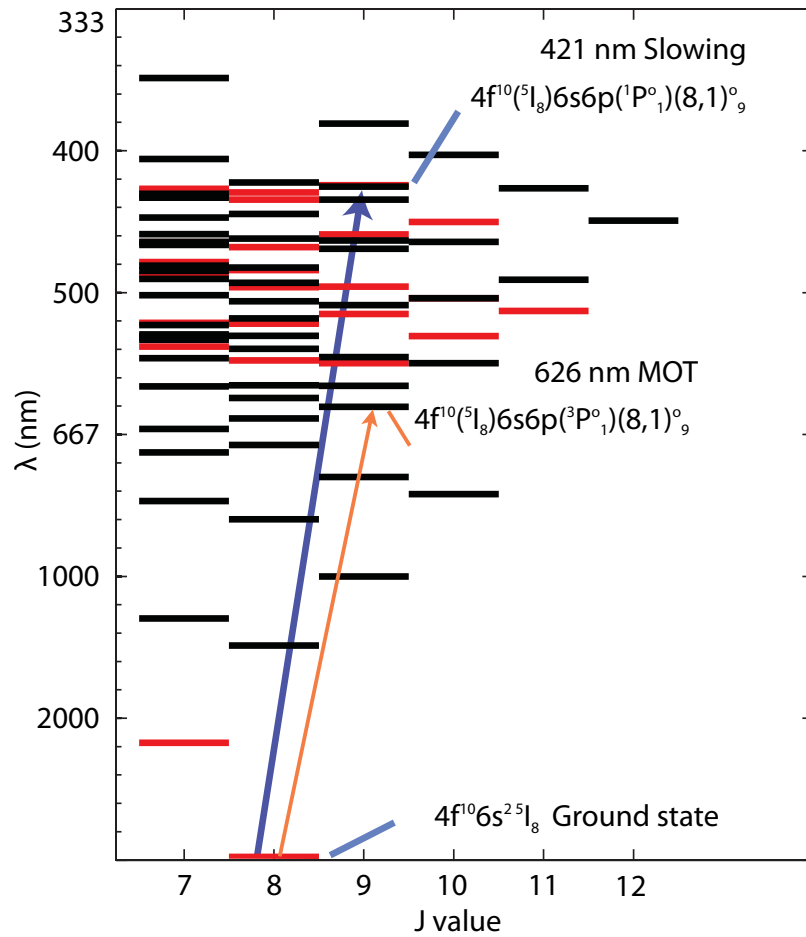


FIGURE 1.5: Dy energy-level diagram with high  $J$  values. The relevant laser cooling transitions between the even parity (red) ground state and the odd (black) excited states are marked with wavelengths and spectroscopic terms. The figure has been modified from ref. [19].

TABLE 1.2: Characteristics of the transitions in use [3](\*) from [22].

SYMBOL	DESCRIPTION	421 nm	626 nm
$\lambda$	wavelength (air)	421.1714 nm	626.083 nm
$k = \frac{2\pi}{\lambda}$	wave vector	$23\,743\text{ cm}^{-1}$	$1.0 \times 10^5\text{ cm}^{-1}$
$\tau$	life time	4.94 ns	1.17 $\mu\text{s}$
$\Gamma = \frac{1}{\tau}$	spontaneous decay rate	$2.02 \times 10^8\text{ s}^{-1}$	$8.54 \times 10^5\text{ s}^{-1}$
$\gamma = \frac{\Gamma}{2\pi}$			
$\Delta\nu_{\text{NAT}} = \frac{\Gamma}{2\pi}$	natural line width	32.2 MHz	136 kHz
$I_s = \frac{\pi\hbar c\Gamma}{3\lambda^2}$	saturation int.	56.4 mW/cm <sup>2</sup>	72.5 $\mu\text{W}/\text{cm}^2$
$T_D = \frac{\hbar\gamma}{2k_B}$	Doppler temperature	774 $\mu\text{K}$	3.26 $\mu\text{K}$
$T_{\text{REC}} = \frac{\hbar^2 k^2}{2M}$	recoil temp.	660 nK	300 nK
$a_{\text{MAX}} = \frac{\hbar k \gamma}{2M}$	max. acc.	$5.79 \times 10^5\text{ m/s}^2$	$1.68 \times 10^3\text{ m/s}^2$
$v_C = \frac{\gamma}{k}$	OM capture velocity	14 m/s	0.085 m/s
$g$ (*)	g-factor	1.22	1.29

velocity [21] [10]. A narrower transition at 741 nm (14 kHz) exists and has been used to obtain the first Dy Bose-Einstein condensate [26].

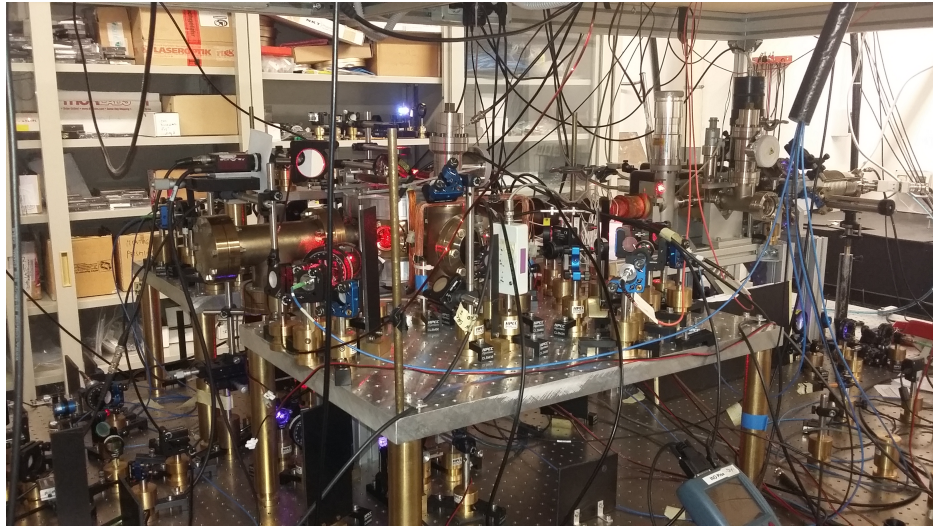


## EXPERIMENTAL SETUP

This chapter is devoted to the description of the setup we used to trap dysprosium atoms. The majority of the apparatus was already built before my thesis started. Even if during my thesis I did not directly build any part of the apparatus, nevertheless a description of the various devices provides a general overview of the experiment.

As said before, we use the 421 nm blue transition for the transverse cooling, the Zeeman-Slower, and the imaging; the 626 nm red transition for the MOT and 1064 nm radiation for the optical dipole traps. Hence we need three laser systems that make the apparatus rather complex and sensitive to the ambient conditions. For these reasons the laboratory is temperature controlled: the temperature oscillates in less than 2 °C in the room and less than 1 °C at the optical tables. In the laboratory there are several optical tables: one containing the red and blue laser sources, shown in FIG. 2.1(A) and a second one with the vacuum setup, shown in FIG. 2.1(B), containing the atomic compound composed by the oven, the Zeeman Slower, and the science cell. The vacuum chamber is placed over a 40 cm supporting structure to allow the entrance of the vertical beams and in order to gain space on the optical table. Two 3.5 cm aluminium breadboard at the same high provide additional support for the necessary optics. One arm of the MOT mounted on one of the two breadboard is showed in FIG. 2.1(C). The two 1064 nm lasers and the relative optics used are place on the second optical table and in other two smaller tables. The light is transported from the various sources by single mode polarization maintaining optical fibers.

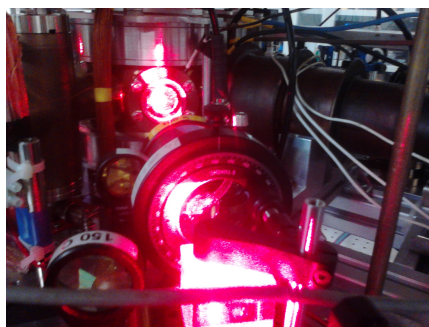
As described in the section of this chapter devoted to the imaging, we extract all the measures from an absorption image of the sample that destroys the sample itself so, in order to perform another measure, a new sample has to be prepared. For this reason the experiment runs in cycles controlled by a computer where all the single operations are scheduled and executed trough TTL and analog signals generators.



(A)



(B)



(C)



(D)

FIGURE 2.1: (A) Picture of the table containing the vacuum chamber. (B) Picture of the red and blue lasers in the dark. (C) Picture of an arm of the MOT. It can be seen the science cell and final coils of the Zeeman Slower. (D) Picture of the two beams of the transverse cooling crossing on the atomic beam. It can also be seen the blue light of the Zeeman Slower scattered by the atoms.

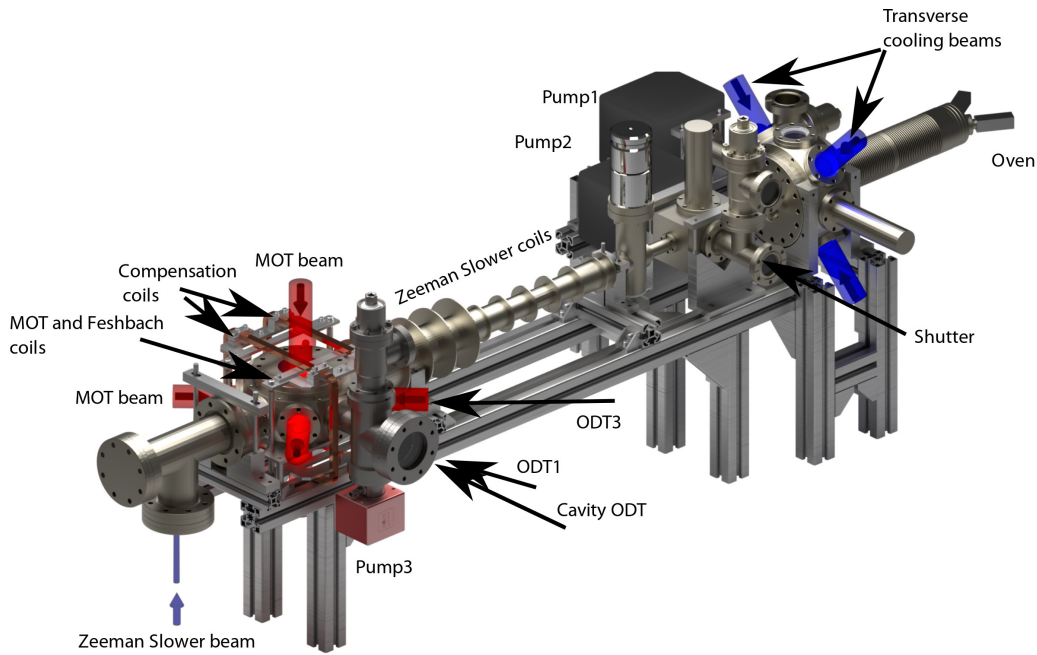


FIGURE 2.2: Scheme of the apparatus.

## 2.1 VACUUM CHAMBER

The vacuum setup is divided in two regions, a first one with the effusive oven of high vacuum ( $< 1 \times 10^{-7}$  Torr) section, and a second one, containing the science cell, of ultra high vacuum ( $< 1 \times 10^{-10}$  Torr). Looking at the apparatus setup from left to right (see FIG. 2.2), the setup is composed of the Dy effusive oven, the transverse cooling section, a differential pumping section that ends with a high vacuum valve that separates the high vacuum and the UHV sections. After the valve there is the Zeeman Slower section then the science cell that terminates with a tee from where the slowing laser beam enters the setup.

The cold atomic cloud in the vacuum chamber is submerged into the residual gas that is in thermal equilibrium with the chamber walls. For this reasons, its composing particles, are moving at velocities of the order of thousand of metre per second. If they collide with a trapped atom this atom is lost regardless of the trap depth that is by far lower than the thermal particles energy. This kind of atom loss is proportional to the probability that such collision occurs, hence to the atomic cloud density multiplied the residual gas density, and is called one body loss. In this picture, the number of atoms that remain trapped can be described by a decreasing exponential function of the time and its time constant is called the lifetime of the trap. In order to increase the cloud lifetime, the residual gas pressure has to be made as low as possible.

A particular attention is paid to the effusive oven. If, on the one hand, a higher pressure of the subliming dysprosium is desirable to achieve an intense atomic flux, on the other hand high velocity dysprosium atoms are a cause of trapped atom losses. This particular situation is circumvented using a differential pumping stage: in the relatively high pressure zone of the oven section, a Varian VacIon Plus 20 ion pump (that has an ultimate pressure of  $10^{-11}$  Torr)

is placed. This section of the experimental chamber is then connected to the beginning of the Zeeman Slower with a tube 8 cm in length and 5mm in diameter and at its end is placed a second ion pump identical to the first one. In the molecular flux condition (the condition in which gas density is so small that particles interact primarily with the chamber surface rather than with each other) the small conductance of this tube guarantees a pressure difference at the tube extremes, in this way the higher pressure zone of the oven is separated from the lower pressure zone at the beginning of the Zeeman Slower. At the end of the Zeeman Slower, in the proximity of the MOT chamber, there is a third pump: a NEX Torr D 100-5 (that, again, has an ultimate pressure of  $10^{-11}$  Torr). This pump is a combination of a small ion pump and a getter cartridge and is placed as close as possible to the MOT zone without getting into the optical paths. The pressure in the MOT chamber can be estimated by the current of ions gathered by the last pump that is smaller than minimum current the device can read, so it can be said that, at least in this zone, the pressure is lower than  $1 \times 10^{-11}$  Torr.

At the beginning of the Zeeman Slower is present a shutter used to block the atomic flux once the MOT is loaded in order to protect the trapped atoms from the non slowed atoms; the Zeeman Slower beam is turned off once the MOT is loaded because, given the large difference in the linewidth of the respective transitions, atoms trapped in the MOT are easily pushed away by the blue light.

Externally of the science cell (see FIG. 2.2) we find different coils necessary for the generation of the magnetic fields. There are two pairs of circular coils with vertical axes placed in Helmholtz and anti-Helmholtz configuration, i.e. with their radius equal to their distance. The coils used for the MOT are in the anti-Helmholtz configuration, the current flow in a coil is opposite than in the other, in this way is generated a linear magnetic field gradient around the point on the common axis equidistant from the coils centres (the MOT is formed in the vicinity of this point). In each of the coils in the Helmholtz configuration the current flow is the same in order to generate a constant magnetic field in the neighbourhood of the quadrupole centre. The current flow in these two coils is controlled and stabilised by a PID, because they are used for the Feshbach spectroscopy hence the magnetic field has to be fine controlled. Other two rectangular coils are placed in a quasi Helmholtz configuration with the axis in common with the Zeeman Slower axis and are used in order to compensate for the disperse magnetic field emerging from the Zeeman Slower itself.

The Zeeman Slower laser beam enters in the vacuum chamber vertically and then is turned horizontally by a  $45^\circ$  mirror. In a precedent configuration a window was used but the glass was coated by the dysprosium flux coming from the beam. The use of the mirror, being the dysprosium coating reflective, avoid this problem.

The stainless steel MOT chamber is a standard octagonal cell (by Kimball) with CF40 flanges on the side surface and other two windows one on the top and one on the bottom surfaces that provide the optical access for the MOT, the ODT and the imaging beams.

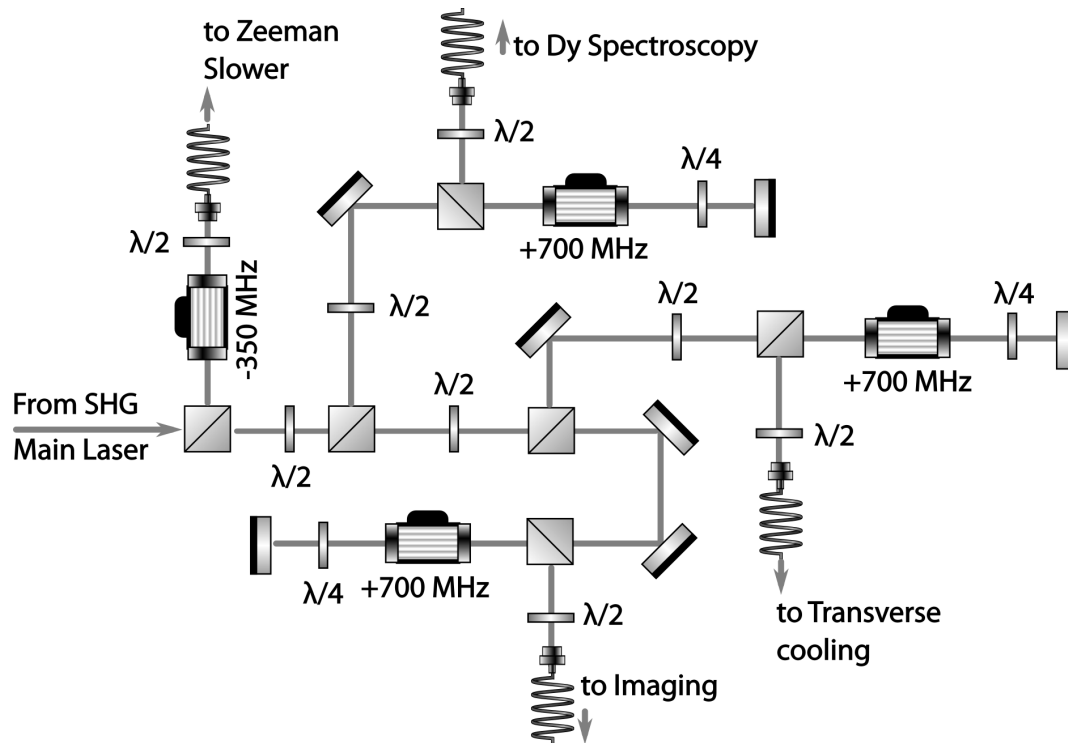


FIGURE 2.3: Schematics of the 421 nm laser optics after the SHG frequency doubling cavity, lenses for the beam shaping are omitted. The frequency of the different beams is detailed in the text. In the present setup the third fiber for imaging is not used and the imaging beam is derived from the one for transverse cooling.

## 2.2 THE 421 nm LASER

The 421 nm light is obtained by frequency doubling the 842 nm light with a second harmonic generation (SHG) cavity. The laser is subsequently locked to the atomic line by the Pound-Drevel-Hall technique performed on the dysprosium atomic beam itself via modulation transfer spectroscopy. The laser project is detailed in [3]. As showed in FIG. 2.3 the laser is divided in to three different beams. The first beam, after a double passage in a 350 MHz AOM is shined on the atomic beam to perform both the spectroscopy and the frequency lock; the second one, again after a double passage in a 350 MHz AOM is used for the transverse cooling and the imaging; the third one after a single passage in a in a  $-350$  MHz AOM is sent to the Zeeman Slower. In this way the transverse cooling and imaging beams are in resonance with the atomic transition (correction of the order of  $\Gamma_{421}$  are done fine-tuning the AOM frequency) while the Zeeman Slower is red detuned by  $1 \text{ GHz} \approx 27\Gamma_{421}$  as designed. Furthermore the AOM can be used as an optical switch.

The 842 nm laser is a commercial Ti:Sapphire (SolsTiS by M2) laser pumped by another commercial 10 W 532 nm laser (Sprout by Lighthouse Photonics) and generates up to 2.4 W of 842 nm light; it is composed by a Sapphire crystal doped with Titanium enclosed in a ring cavity. The wavelength is conditioned by a birefringent filter and an etalon in the cavity, then, a second external reference cavity with a free spectral range of 3 GHz, narrows the linewidth down to 50 kHz. This cavity is provided with an external input that we use to lock the cavity to the atomic line.

The 842 nm radiation is then frequency doubled by a SHG cavity built in the LENS laboratory in Firenze [3]. This cavity uses an LBO ( $\text{LiB}_3\text{O}_5$ ) crystal in a bow tie optical scheme. In order to actually work, a cavity must have an optical length that is an integer multiple of the light wavelength, hence one of the mirrors is mounted on a piezoelectric transducer controlled via the Hansch-Couillaud locking technique [14]. The construction and analysis of the locking scheme in use is detailed in [3]. Briefly, the LBO crystal has different refractive indexes in the different directions so the optical path depends on the light polarization. Assuming that the cavity length is chosen in order to be an integer multiple of the wavelength for the component of the electric field ( $E_{\parallel}$ ) parallel to one of the optical axes of the LBO crystal, the orthogonal component of the electric field ( $E_{\perp}$ ), due to the difference in the refractive index, doesn't propagate in the cavity and is reflected with no change in its phase with respect to the incident field.  $E_{\parallel}$ , on the other hand, does propagate in the cavity and acquires a phase  $\delta$  with respect to  $E_{\perp}$ . At resonance it holds  $\delta = 2\pi m$  and the reflected electric field  $E^{(r)} = E_{\perp}^{(r)} + E_{\parallel}^{(r)}$  is linearly polarised. Out of resonance we have  $\delta \neq 2\pi m$  and  $E^{(r)}$  is elliptically polarised. With a  $\lambda/4$  waveplate it is possible to distinguish these two situations by sending the two elliptical polarizations to two photo diodes and monitoring the difference in their output signals.

Once obtained the 421 nm light, it is possible to lock the SolsTiS reference cavity to the atomic transition. In order to have a Doppler-free reference the saturated absorption spectroscopy scheme [11] is used. In a first apparatus design a hollow cathode lamp was used as source of dysprosium vapour unfortunately these lamps have a too short lifespan (two of them were required over three years) for our purpose and so the locking scheme has been changed and today the atomic beam emerging from the oven is used instead. The locking principles are in any case the same: atoms are excited by a pump beam and the absorption of a counter-propagating probe beam is observed. If the two beams have the same frequency, because of the Doppler shift,

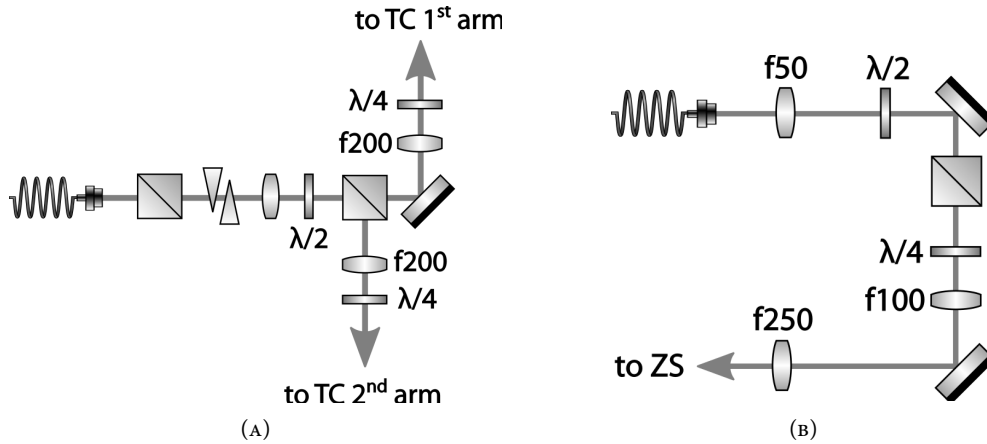


FIGURE 2.4: (A) Scheme (not to scale) of the transverse cooling (TC) optics; the first polarising beamsplitter is inserted in order to have a clean linear polarised light. The beam is then elliptically shaped by two anamorphics prisms and divided in two with  $\lambda/2$  waveplate and a second polarising beamsplitter in order to balance the two arms intensities. The two  $\lambda/4$  waveplates change the polarization from linear to circular, finally the two beams are retroreflected. (B) Scheme (not to scale) of the Zeeman Slower (ZS) optics; after the polarising beamsplitter the light is linearly polarised and finally made circular by the  $\lambda/4$  waveplate.

they interact only with atoms moving at a velocity  $v = 0$  along the beams propagation direction; the pump beam excites these atoms and as a consequence the absorption of the probe beam is decreased. In this way it is possible to obtain a Doppler free absorption peak whose width is comparable to the natural linewidth. The actual lock is detailed in [3]. Briefly, the pump probe is phase modulated by an EOM and this modulation is transferred to the pump beam via the modulation transfer spectroscopy [23] and used in a Pound-Drever-Hall configuration [4] where, instead of the reflection from the cavity, the transmitted probe beam is used to generate the error signal.

### 2.2.1 ZEEMAN SLOWER AND TRANSVERSE COOLING

The optical schemes of the transverse cooling (A) and the Zeeman Slower (B) respectively are reported in FIG. 2.4.

The transverse cooling creates a 2D optical molasses (sec. 1.3.1) acting on the plane perpendicular to atomic beam propagation direction in order to increase the atomic beam density (sec. 3.1). It applies a viscous force to the velocities perpendicular to the propagation direction the time dependence is given by EQ. 1.35:  $v(t) = v(0)e^{-(\beta/M)t}$ , where  $\beta$  is given by EQ. 1.34 and  $M$  is the atomic mass, and the damping is heavily dependent on the interaction time. The gaussian  $TEM_{00}$  beam emerging from the optical fibre is elliptically shaped by two anamorphics prisms in the direction of the propagation of the beam in order to increase the transit time while maintaining an intensity as large as possible. The beam has 3.5 and 8 mm waists at the atomic beam position. Two  $\lambda/4$  waveplates change the light polarization from linear to circular to optimize the

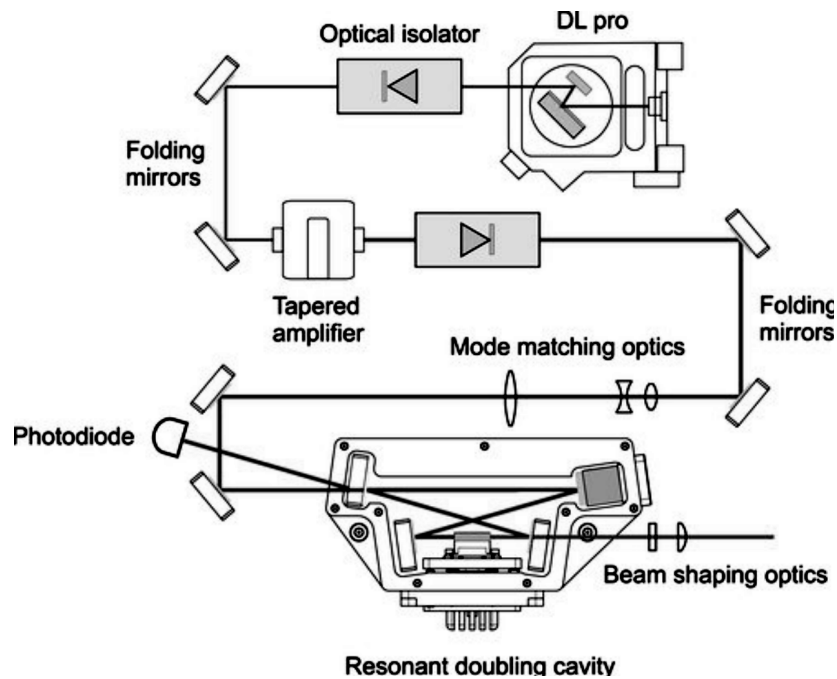


FIGURE 2.5: Scheme of the Toptica TA-SHG Pro (from the technical manual).

transverse cooling.

The Zeeman Slower optics is designed in order to focus the laser beam at the oven position so as to mimic the atomic beam size increase with the distance (see fig. 3.3) from the oven itself. Its waist at the MOT position is 8 mm and the light is circularly polarised.

### 2.3 THE 626 nm LASER

In order to be able to load the atoms in an optical dipole trap, we choose, to operate the MOT, the narrow line 626 nm transition, which has a residual Doppler temperature of only 3.2  $\mu\text{K}$ . The light at this wavelength is obtained by a Toptica TA-SHG Pro laser (FIG. 2.5), a commercial compact device. An external cavity laser diode generates a low intensity radiation at 1252 nm that is amplified by a Master-Oscillator Power-Amplifier (MOPA) and then frequency doubled in a bow-tie cavity in order to obtain nearly 1 W of radiation at the desired wavelength. The laser scheme is reported in FIG. 2.5 from its technical manual. According to the datasheet, this laser has a line-width of  $\sim 20\text{ kHz}$ , hence narrower than the dysprosium line-width of 135 kHz- Given the small saturation intensity of the transition choosen, we are able to obtain a peak intensity higher than  $200I_s$  in either of the three MOT beams.

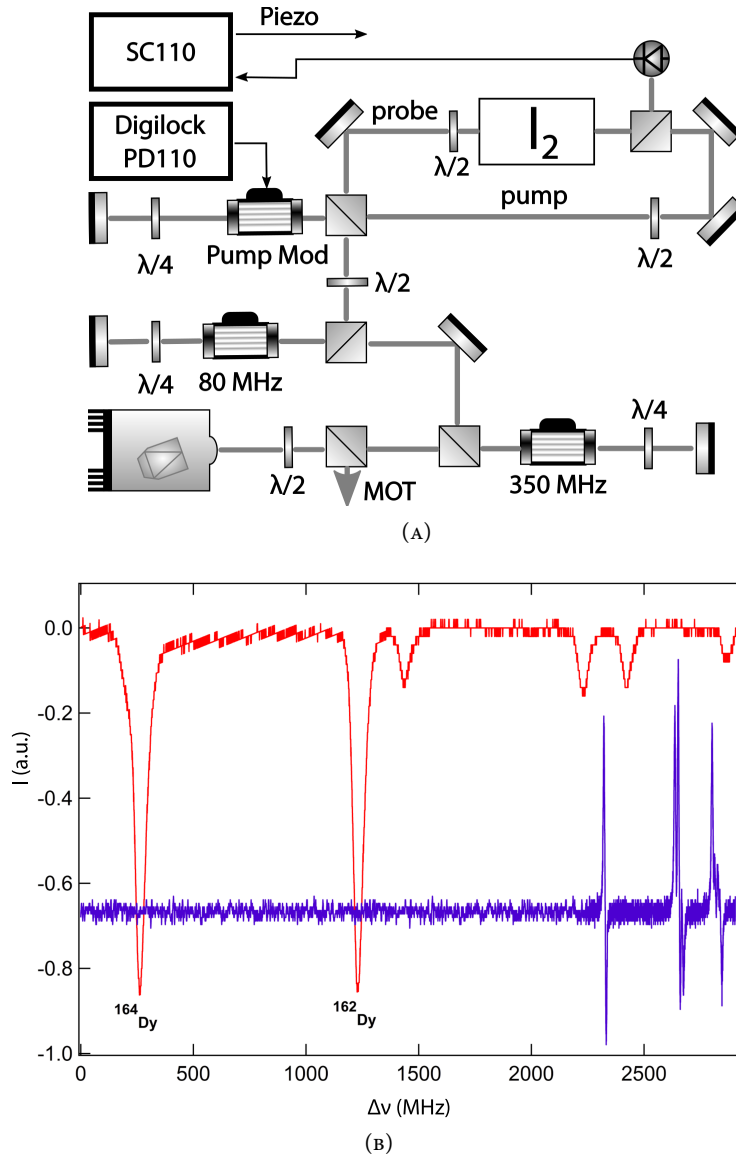


FIGURE 2.6: (A) Diagram of the locking scheme: one of the three AOM operates at 350 MHz and the other two at 80 MHz, all of them are in double passage. (B) Saturated absorption error signal of the  $I_2$  (in blue) and the Dy 626 nm transition spectroscopy (in red), the frequency gap between the  $^{162}\text{Dy}$  peak and the last Iodine peak is bridged by 4 AOMs.

### 2.3.1 IODINE LOCK

The reference signal necessary to lock the 626 nm laser to the atomic transition is obtained again via the saturated absorption spectroscopy of an Iodine ( $I_2$ ) transition. In FIG. 2.6 are reported both the optical scheme (A) and dysprosium absorption (red) and the error signals (blue) that this apparatus provides (B).

As already said in the previous section, the saturated absorption spectroscopy permits to achieve a Doppler free absorption signal. The optical scheme is reported in FIG. 2.6(A) and is analogous to the one used for the blue 421 nm lock: a strong pump beam excites the atoms and the absorption of a weaker counter-propagating probe beam is observed, in this way only the  $v = 0$  atomic velocity class is resonant. To obtain the error signal the pump beam is frequency modulated at 43 kHz and thanks to the non linear Iodine response, this modulation is transferred to the probe beam [23]. The lock-in technique can be described observing the absorption signal in FIG. 2.7(A). If the laser frequency is below resonance, then the resulting probe amplitude modulation (determined by the slope of the absorption curve) has a phase that is opposite with respect to the modulation one. On the other hand, if the laser frequency is above resonance, the the resulting amplitude modulation has the same phase as the frequency modulation. At this point, if the probe beam is detected by a photodiode, and the electric signal produced by the photodiode is multiplied by a square symmetric zero-crossing wave with the same period and the same phase (this is done with a mixer, like in the Pound–Drever–Hall scheme), the mixed signal oscillates at a double frequency with respect to the original pump modulation frequency. Furthermore, the mixed signal, is negative, null and positive at a base laser frequency respectively smaller, equal and higher than the resonance one. As a final step, the mixed electric signal, is low-pass filtered with a cutoff frequency lower than the probe modulation frequency resulting in the needed error signal.

### 2.3.2 MOT OPTICAL DESIGN

The optical scheme of the MOT is reported in FIG. 2.7. With a series of  $\lambda/2$  waveplates and polarising beamsplitters, it is possible to adjust the relative intensity in the three MOT's arms. The AOM allows to control the laser beam both in frequency and in amplitude, an can be used as an optical switch. During the loading of the MOT the light is far red detuned ( $-35\Gamma_R$ ) while during the compression stage both detuning and intensity of the beams are reduced in order to maintain a sufficient confining force and a small scattering rate. In addition, during the MOT loading phase, the AOM frequency is modulated ( $\sim 2$  MHz at 135 kHz rate) in order to increase the MOT capture velocity (see FIG. 1.2). Once atoms are captured and cooled their velocity dispersion is reduced and the frequency modulation is no more necessary and turned off.

The maximum velocity an atom can have and still be captured by the MOT, the MOT *capture velocity*, can be estimated by equating the kinetic energy of the atom to the maximum work that the scattering force can make along the laser beam diameter. Considering that the scattering force saturates at high intensity (see EQ. 1.25), enlarging the beam waist results in a higher capture velocity, provided (as in our case) that the light intensity remains well above the saturation intensity. The design of each of the three MOT arms follow this concept: the three beams are made

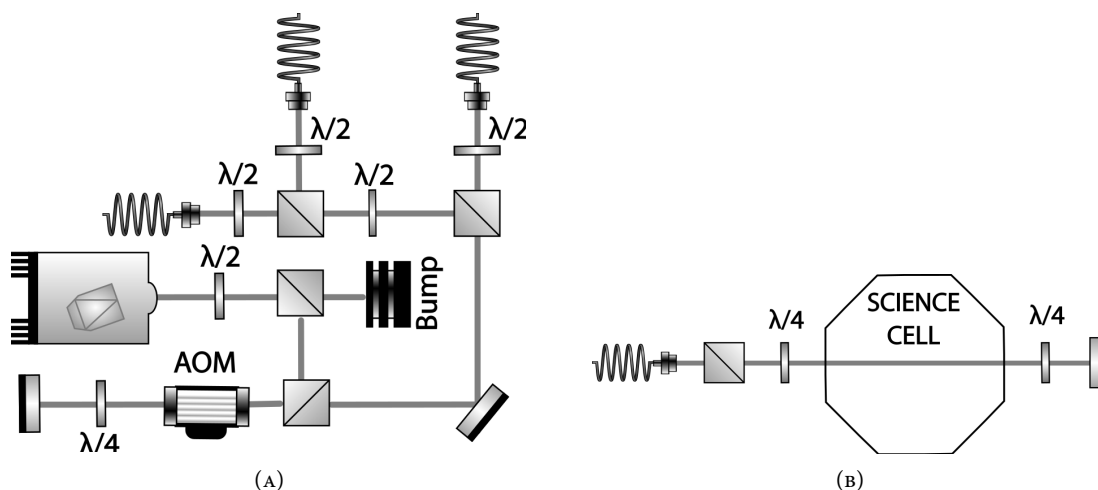


FIGURE 2.7: Scheme of the MOT optics. (A) The 626 nm light is injected in three mono mode (PM) optical fibers, the AOM is used for both frequency and amplitude modulation of the light. (B) The first  $\lambda/4$  waveplate turn the light polarization from linear to circular while the second one, a the first passage turn the polarization to linear and, at the second passage, again circular but with opposite ellicity (see FIG. 1.3).

as wide as possible, the limit being the windows diameter 4 cm of the science cell. The out of scale scheme of the optics used is reported in FIG. 2.7(B) (the scheme is the same for all the three beams). A certain attention has to be paid to the polarization of the light: as depicted by FIG. 1.3, for the correct MOT operation, the two counter-propagating beams have to be circularly polarised but with opposite helicity. At the exit of the fiber the light is approximately linear polarised, then polarization is made clearly linear by a polarizer, then circular by the first  $\lambda/4$  waveplate then again linear by the second  $\lambda/4$  waveplate and finally circular again during the second passage in the second  $\lambda/4$  waveplate.

## 2.4 THE 1064 nm LASERS

The 1064 nm radiation is provided by two commercial Mephisto lasers. They use a Nd:Yag crystal to produce up to 10 W of radiation. Their frequency can be controlled by varying a piezoelectric transducer and by changing the crystal temperature.

### 2.4.1 RESONATOR OPTICAL TRAP

The optical dipole potential is proportional to the laser intensity, in order to be able to confine the atom from the MOT at  $\approx 20 \mu\text{K}$  and with a sufficiently large waist ( $\sim 300 \mu\text{m}$ ), powers of the order of 100 W would be required. In order to reduce this power we use a resonant cavity

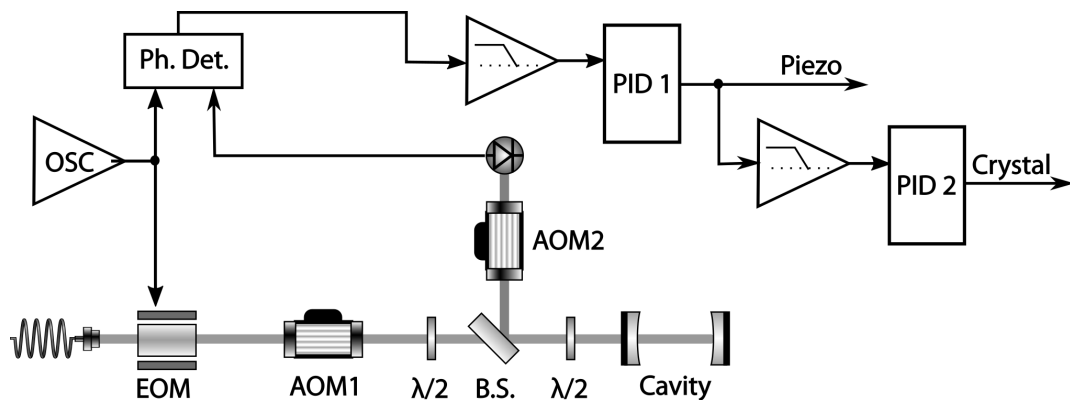


FIGURE 2.8: Scheme of the resonator optical dipole trap and its Pound-Drever-Hall locking scheme. The second AOM is used as a variable quasi neutral-density optical filter to maintain the correct power level on the photo diode. The beam splitter (B.S.) is used to deviate the cavity reflection onto the photo diode.

made with two high-reflectivity spherical mirrors. These mirrors are at 9 cm distance and have a curvature radius of 3 m and the measured cavity finesse is 1050. In this way a 1 W power is sufficient to form a potential of the order of 100  $\mu\text{K}$  (see sec. 3.4). A drawback of this configuration is that the radiation needs to be resonant with the cavity. For this reason one of the Mephysto lasers is locked to the cavity with a Pound-Drever-Hall scheme [4]. A scheme of the principal devices is reported in FIG. 2.8. Because of the laser frequency locking, the light intensity inside the resonator can't be completely switched off even when the other two ODTs are crossed inside the cavity. In order not to perturb the crossed trap, the light intensity has to be reduced by a factor higher than the cavity finesse but, at the same time, the photo diode that provide the signal to the locking electronics has a much lower dynamic range than  $1 \times 10^3$ . For this reason two AOMs are used as quasi neutral-density filter: the first, AOM1 is used to regulate the light intensity in the cavity while the second one, AOM2, is used to regulate the power level onto the photo diode. In this way it is possible to attenuate the light intensity in the cavity by a factor of  $1 \times 10^{-4}$  while maintaining the laser locked.

The Pound-Drever-Hall locking mechanism build uses two PID in order to compensate the slow and fast perturbations of the cavity: the first PID modify the laser frequency varying the Mephysto cavity length via the piezoelectric transducer, and this can compensate high frequency perturbations, then the output of the first PID is low pass filtered and sent to another PID that changes the Nd:Yag crystal temperature in order to maintain the first PID output at zero hence the laser at resonance with the cavity; this second feedback, acting on the crystal temperature, is much slower than the first one but permits higher frequency variations.

#### 2.4.2 SINGLE-BEAM OPTICAL DIPOLE TRAPS

The last two optical traps in use are two single beam optical dipole traps. They are realised by focusing a gaussian  $\text{TEM}_{00}$  beam at 1064 nm. With this configuration the confinement is very weak on the propagation direction of the beam and is much tighter on the transverse directions, so,

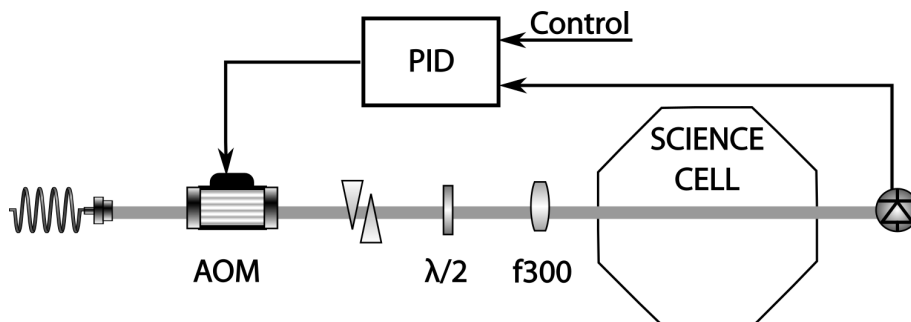


FIGURE 2.9: Optical scheme of the two optical dipole traps in use (for historical reasons  $ODT_1$   $ODT_3$ )  $ODT_1$  doesn't have the two anamorphics prisms and has a gaussian beam with a waist of  $400.6 \pm 0.2 \times 40.6 \pm 0.2 \mu\text{m}$  while  $ODT_3$  is elliptical with a waist of  $36.6 \pm 0.2 \times 80.6 \pm 0.2 \mu\text{m}$  thanks to the two anamorphics prisms. With respect to the other devices they are quite simple: the laser doesn't need to be locked, given the absence of resonating devices and the weak dependence of the dipole force for far red detuning radiation. The feedback loop, composed essentially by the photodiode, the AOM and the PID, necessary to power stabilise the two traps, is also reported.

in order to have a three dimensional confinement, we use two crossed gaussian beams at an angle of  $40^\circ$ . One of the two traps ( $ODT_1$ ) is a *cylindrical trap* because is made with a radial symmetric beam, the other (for historical reasons  $ODT_3$ ), being made with a elliptic cross section beam, is called an *elliptic trap*. In this way, the harmonic potential confining the atoms has comparable frequencies in all the three axes. Given the dipolar nature of dysprosium, the frequency of the potential along the polarization direction of the atoms needs to be higher than the one in the other two directions [18], and this is why  $ODT_3$  is made cylindrical.

Given the absence of resonant devices and the weak dependence of the dipole force on the radiation frequency (in the case of far red detuned radiation), the design of these two traps, depicted in FIG. 2.9, is quite simpler than the others encountered so far. Anyway, they need to be power stabilised, particularly in the last phases of the evaporation, because the potential depth depends linearly on the laser intensity hence fluctuations in the laser power perturb the potential and, in the end, can lead to atom losses. The power stabilisation is obtained using an AOM, a photodiode and a PID. At this wavelength the AOM frequency modification can be neglected but its transmissivity as a function of the RF power at which it is drive, can't. The power control is achieved by sending the photodiode signal (proportional to the laser intensity) to an input of the PID, the other input is driven by the control apparatus and it works as a stable and noise free reference. The PID output drives the RF arriving at the AOM controlling that the beam intensity matches the reference input. In this way, to some extent, the potential depth is independent on the actual laser power and to the noise.

As previously said, the resonator trap can't be completely turned off otherwise the lock of the laser fails. Furthermore, as already said, the high finesse cavity increases by a factory of roughly  $\sim 1000$  the radiation intensity present in the cavity and it easily perturbs the others optical dipole traps even though its power is set to the minimum. For this reason, the  $ODT_1$  is designed to be lowered by 3 mm moving one focusing lens. In this way, when atoms are loaded in the dipole traps, the resonator influence is completely neglected. This feature has not been actually used for

obtaining the first  $^{162}\text{Dy}$  BEC.

## 2.5 IMAGING SETUP

Data are extracted using standard absorption imaging with 421 nm resonant light through horizontal or vertical direction at choice. A short blue flash of the duration of 0.13 ms and a power of roughly 7 mW is sent to the trapped atoms and then an image is registered with a Stingray digital camera. Considering that the lifetime difference between the 626 and the 421 nm transitions is of the order of  $1 \times 10^3$ , for each scattering event in the MOT roughly a thousand scattering events with the imaging beam occur so atoms are easily scattered out of the MOT and out of any ODTS, so the imaging process results in the destruction of the sample.

In order to have a background-independent measure of the total absorption of the atomic sample, three images are required. The first one (“Im<sub>1</sub>”) with the atoms present; a second one (“Im<sub>2</sub>”) taken after all the atoms are scattered but with all the laser beams on and a third one (“Im<sub>3</sub>”) with all the beams turned off. Assuming that the camera provides a signal in the form of  $\text{Im} = AI + B$ , where  $Im$  are the pixels values corresponding to an intensity  $I$  and  $A$  and  $B$  are respectively the gain and the offset, the final measure is actually done on an image constructed as  $\text{Img} = -\ln\left(\frac{\text{Im}_1 - \text{Im}_3}{\text{Im}_2 - \text{Im}_3}\right) = \ln(I_0/I)$  that depends only on the ratio between the light intensity collected with the atoms ( $I$ ) and without the atoms ( $I_0$ ).

The first blue flash of intensity  $I(z=0) = I_0$  encounter in his path an atomic cloud with numeric density given by EQ. 1.62:

$$n(x, y, z) = \frac{N}{(2\pi)^{3/2} \sigma_x \sigma_y \sigma_z} e^{-\left(\frac{x^2}{2\sigma_x^2} + \frac{y^2}{2\sigma_y^2} + \frac{z^2}{2\sigma_z^2}\right)} \quad (2.1)$$

moving along the  $\hat{z}$  direction, for the light intensity it can be written:

$$\frac{\partial I(z)}{\partial z} = -\left(N_1(z) - N_2(z)\right) \sigma(\omega) I(z)$$

and, using a resonant light and considering all the atoms in the ground state, for the absorption cross section and for the populations it can be written:

$$N_2 = 0 \quad \omega = \omega_A \quad \rightarrow \quad \sigma(\omega) = \sigma = \frac{3\lambda^2}{2\pi}$$

so the equation becomes  $\frac{\partial I}{\partial z} = -n(x, y, z) \sigma I$  whose solution is

$$\ln\left(\frac{I(x, y, z)}{I_0}\right) = -\sigma \int_a^z n(x, y, z') dz';$$

posing  $I(z) = I_0$  for  $z \leq a$ ; for  $z \rightarrow \infty$  it becomes:

$$\ln\left(\frac{I(x, y)}{I_0}\right) = -\frac{N\sigma}{(2\pi)\sigma_x\sigma_y} e^{-\left(\frac{x^2}{2\sigma_x^2} + \frac{y^2}{2\sigma_y^2}\right)}. \quad (2.2)$$

The image used by our imaging program is then

$$\text{Img}(x, y) = -\ln\left(\frac{I(x, y)}{I_0}\right) = \frac{N\sigma}{(2\pi)\sigma_x\sigma_y} e^{-\left(\frac{(x-x_0)^2}{2\sigma_x^2} + \frac{(y-y_0)^2}{2\sigma_y^2}\right)} \quad (2.3)$$

where  $x_0$  and  $y_0$  are the coordinate of the cloud centre.

In order to extract useful information from EQ. 2.3, a fit is done in the two orthogonal directions: the program sums the pixels over the same row (i.e. over  $x$ ) in order to obtain

$$\ln\left(-\frac{I(y)}{I_0}\right) = \frac{N\sigma}{\sqrt{2\pi}\sigma_y} e^{-\frac{(y-y_0)^2}{2\sigma_y^2}} \quad (2.4)$$

and then it calculates the fit using  $A = MP_y N_y \sigma / \sqrt{2\pi} \sigma_y$  and  $MP_y \sigma_y$  as fit parameters, where  $M$  is the magnification factor and  $P_y$  the  $\hat{y}$  pixel dimension, and then it calculates  $N_y$  and  $\sigma_y$ . Repeating the same procedure but summing over each column ( $y$ ) it obtains  $N_x$  and  $\sigma_x$  and finally  $N = \sqrt{N_x N_y}$  ( $x_0$  and  $y_0$  are obtained directly from the maximum in the image).

### 2.5.1 TIME OF FLIGHT MEASUREMENT

If the confining potential is turned off, after a time  $t$  The Maxwell-Boltzmann velocity distribution will be

$$f(\mathbf{v}) = \left(\frac{2\pi k_B T}{M}\right)^{-\frac{3}{2}} e^{-\frac{1}{2} \frac{M\mathbf{v}^2}{k_B T}} \quad (2.5)$$

given the absence of any potential it can be written:  $\mathbf{r}(t) - \mathbf{r}_0 = \mathbf{v}t$  and EQ. 2.5 becomes

$$f(\mathbf{v}) = \frac{1}{(2\pi)^{3/2}} \frac{1}{\sigma_v^3} e^{-\frac{(\mathbf{r}-\mathbf{r}_0)^2}{2\sigma_v^2}}; \quad \sigma_v^2 = \frac{k_B T}{M} t^2 \quad (2.6)$$

thus the distribution of the final position of the atoms is

$$n(\mathbf{r}) = \int_{-\infty}^{\infty} n(\mathbf{r}_0) f\left(\frac{\mathbf{r}-\mathbf{r}_0}{t}\right) d\mathbf{r}_0 = \frac{N}{(2\pi)^{3/2}} \frac{1}{\sigma_x(t)\sigma_y(t)\sigma_z(t)} e^{-\left(\frac{x^2}{2\sigma_x^2(t)} + \frac{y^2}{2\sigma_y^2(t)} + \frac{z^2}{2\sigma_z^2(t)}\right)} \quad (2.7)$$

where

$$\sigma_{x,y,z}^2(t) = \sigma_{x,y,z}^2(0) + \frac{k_B T}{M} t^2. \quad (2.8)$$

By taking an *in situ* absorption image it is possible to measure the cloud size while by taking the image after a free expansion time, it is possible to calculate the velocity distribution and thus the atomic temperature.

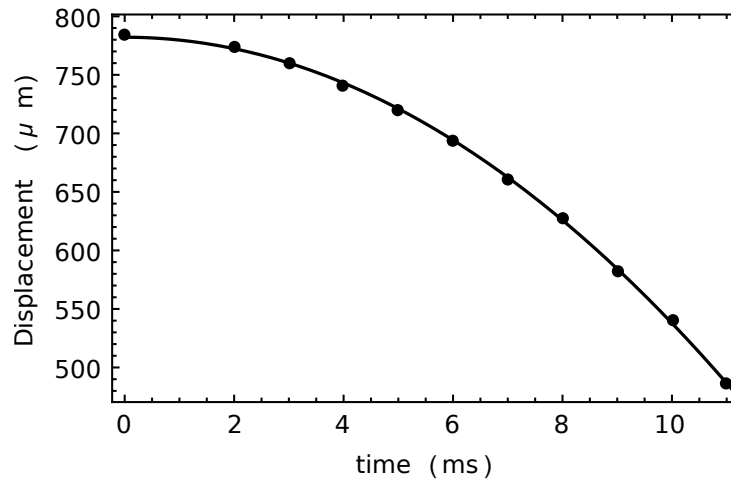


FIGURE 2.10: Cloud centre displacement as a function of time (dots) and (line) the fit result with the function  $z = O + \frac{1}{2}At^2$ .

### 2.5.2 HORIZONTAL IMAGING MAGNIFICATION

In order to have more detailed images, the imaging beam passes through a series of optics that enlarge it so to produce magnified images. If, on the one hand, this magnification is useful, on the other hand can produce a systematic error.

The magnification factor can be calculated via the geometric optics laws and, at least for the horizontal beam, using the acceleration of a free falling body as a reference.

FIG. 2.10 reports the measure of the central position of a free falling cloud (at rest at  $t = 0$ ) for different times  $t$ . The displacement from the  $t = 0$  position is then  $z(t) = -\frac{1}{2}gt^2$  where  $g = 9.81 \text{ m/s}^2$  is the gravity acceleration. In our case, performing a fit with the function:  $z(t) = O - \frac{1}{2}At^2$ , where  $A = gM(\text{pxsize})$  and  $O$  is the initial position, gives  $A = 4.89$  and, keeping in mind that the camera in use has pixel of  $6.45 \mu\text{m}$ , a magnification factor of  $M = 3.2$ , in very good accordance with the calculated one.

## RESULTS

This chapter is devoted to present our experimental results. They will be reported in an order related to the various physical phenomenons presented in cap. 1 that, incidentally, is the same order of the phenomena that atoms, in their travel toward the degeneracy, experience.

The first process described is the so called transverse cooling stage. It is essentially a 2D optical molasses arranged in the plane orthogonal to the atomic beam. It is intended to collimate the atomic beam and maximize the atomic flux arriving at the MOT position and, as an example, a measure of the fluorescence radiation is reported.

For what concerns the Zeeman Slower, I report some simulation results that helped in the understanding how the various parameters like current, laser detuning and oven temperature are related and the measure of the final velocity.

Our MOT, given the narrow-line used, is rather peculiar, and a description and a characterization are reported. Together with the measured results are discussed and compared with the publications from other experiment.

Finally, it follows a description of the various optical dipole traps, along with the discussion of the various parameter measured, and a comparison with the performed calculation.

Strictly related to the optical dipole trapping technique, there is the forced evaporative cooling (today under development) so a description of the various ramps and, for what is in my capabilities, a description of the phenomenon involved is reported.

Obviously in this chapter there is not only my work but there is the work of several physicists. In any case I participated, although with a limited role in all the reported measurements.

As it will be said in the following, our measurements are entirely done with absorption imaging, which destroys the sample. So the experiment works in cycles: the atomic beam is slowed, then the MOT is loaded, then the resonator dipole trap and finally the three single beam optical dipole traps are loaded. If an absorption imaging is performed at some point the sample is lost and another measure is taken in the successive cycle. The various samples aren't exactly equal but exhibit some fluctuations, especially in the number of atoms that can vary up to 30% from cycle to cycle. This is our biggest error source so, each measure is obtained repeating the same measure a certain number of times. The error is then calculated by using standard error theory.

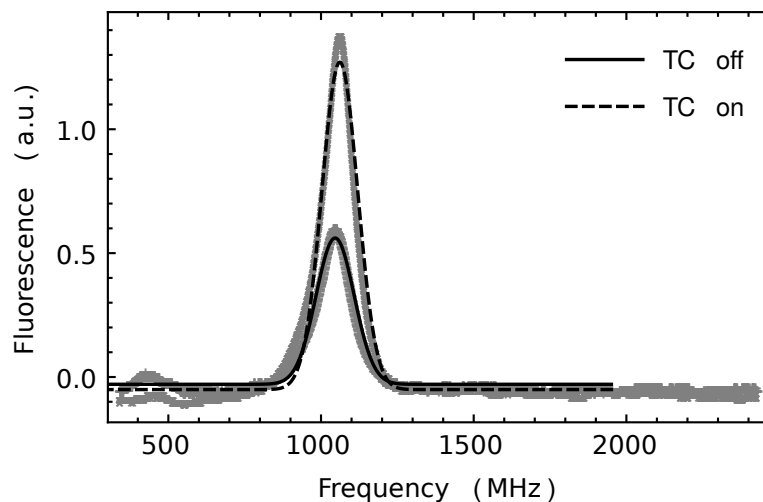


FIGURE 3.1: Fluorescence signal at the science cell obtained shining the 626 nm laser orthogonally with respect to the atomic beam. The laser frequency was modulated in order to scan a useful range of velocities. The resulting transverse velocity distributions have quite similar widths but Data are fitted with  $y = A/\sqrt{2\pi}s\exp(-(x-x_0)^2/2s^2)$ ; the ratio between the two  $A$  parameters is  $\sim 2.1$  and between the two  $s$  parameters is  $\sim 1.1$ . The resulting fit functions are integrated leading to a 16:9 ratio. The  $x_0$  parameter is necessary because the frequency scale hasn't an absolute reference.

### 3.1 TRANSVERSE COOLING

The transverse cooling stage is intended to increase the density of atoms propagating at small angles and thus entering the ZS and being slowed. It consists in a 2D optical molasses that slows the velocities in the plane  $xz$  orthogonal to the Zeeman Slower axis  $y$ . The transverse velocities are dumped exponentially with a certain time constant (see SEC. 1.3.1) so the cooling effect is dependent on the interaction time between the moving atoms and the laser beams. The beams are shaped with an elliptical waist with  $3.5 \times 8$  mm axis in order to increase this interaction time, have total laser power of 75 mW ( $\simeq 3I_s$ ) and a detuning of  $\delta = -\gamma/3$ . We tried different configurations in the beams path and polarizations and the best one was with two retroreflected beams of the same intensity, obtained by splitting the blue light. The power balance was controlled by a  $\lambda/2$  plate and a polarising beam-splitter and two additional  $\lambda/4$  allowed varying the polarization.

Assuming that the atoms reach a thermal equilibrium in the path from the oven to the science cell, the final Maxwell-Boltzmann distribution has always the same width but different peak density respectively with or without the transverse cooling. In FIG. 3.1 are reported two fluorescence spectra of the atomic-beam at the science cell, the fluorescence was collected by a photomultiplier tube orthogonal both to the probe laser and the atomic-beam. By modulating the frequency of the 626 nm laser, atoms with different velocity were excited at different frequencies thanks to the Doppler effect. The amplitude of the signal produced by the photomultiplier tube was proportional to the number of excited atoms. Again, data in FIG. 3.1 are fitted with a gaussian function whose integral is proportional to the atom density. From the data analysis it emerged that the peak atom density is increased by a factor of 2.1 by the transverse cooling, in these

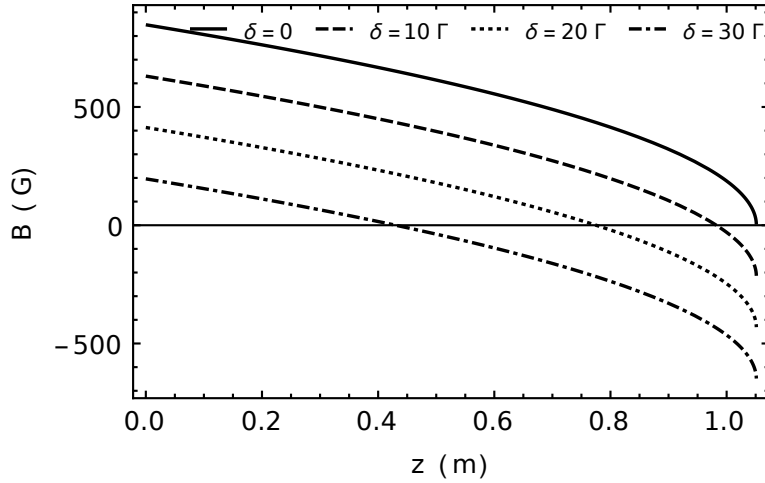


FIGURE 3.2: The magnetic  $B(y)$  calculated with EQ. 3.5 for different values of the detuning  $\delta$ , the saturation parameter is  $s = \infty$ .

conditions we observed an increase up to a factor of 4 in the number of trapped atoms in the MOT with the transverse cooling turned on.

### 3.2 ZEEMAN SLOWER

The aim of the Zeeman Slower is to provide a flux of dysprosium atoms cool enough to be captured by the MOT. For this task, thanks to its strength, the 421 nm blue transition is used with a circular polarised light.

Because of the magnetic dipole moment of  $\mu 9.93\mu_B$ , the dysprosium atoms in a non zero magnetic field are aligned in the direction of the field, and the use of circularly polarised light lead to a  $\sigma^-$  ( $\sigma^+$ ) transition which pumps atoms in a “stretched” i.e.  $J = 8$ ,  $m_J = -8$  (*optical pumping*). From EQ. 1.88 the most probable velocity of an atom at 1110 °C is  $v_{MP} \approx 480$  m/s and at this velocity the time for covering a 0.5 m distance (approximately the Zeeman Slower length) is 1 ms. Given the 421 nm transition lifetime of 4.94 ns (TAB. 1.2) the number of absorption followed by spontaneous emission is roughly  $1 \times 10^5$  and, because of the optical pumping, all the atoms can be considered cycling between the  $J = 8$ ,  $m_J = -8$  and  $J = 9$ ,  $m_J = -9$  states hence a two state model of the atom can be used.

As reported in chapter 2, the Zeeman Slower principle is based on the force EQ. 1.40 that has to be adapted to our case so  $\mu_B \Delta m_J = \mu_B (g_J' m_J' - g_J m_J)$  and, for light atoms where the L-S coupling is valid, the expression for the  $g$ -factor is:

$$g_J = 1 + \frac{J(J+1) + S(S+1) - L(L+1)}{2J(J+1)}. \quad (3.1)$$

Dysprosium is a quite heavy atom so the previous expression (EQ. 3.1) is not exact, the correct g-factor values are  $g' = 1.22$  and  $g = 1.24$  [15] so, in our case the correct form of EQ. 1.40 is

$$F_{ZS} = \hbar k \frac{\gamma}{2} \frac{s}{1 + s + \frac{4}{\gamma^2} (\delta + kv - 1.06 \frac{\mu_B B(y)}{\hbar})^2}. \quad (3.2)$$

As already reported in SEC. 1.4 the force in EQ. 3.2 is maximum when the term in bracket at the denominator is zero, leading to the condition for the magnetic field

$$B(y) = \frac{\hbar}{1.06 \mu_B} (kv(y) + \delta). \quad (3.3)$$

So, for each atom moving at the velocity  $v(y)$  the maximum possible force is  $\eta F_{MAX}$  (where  $\eta < 1$  is a “security” factor introduced to have into account the fact that the force can be non optimal. In our case a value  $\eta = 0.4$  has been chosen. This determines the length of the Zeeman Slower). Once the initial and final velocities ( $v_i$  and  $v_f$  respectively) and the saturation parameter  $s$  are chosen, the length of the apparatus  $z_0$  and the maximum force  $F_{MAX}$  are determined by

$$y_0 = \frac{1}{2} M \frac{v_i^2 - v_f^2}{\eta F_{MAX}}; \quad F_{MAX} = \hbar k \frac{\gamma}{2} \frac{s}{1 + s}. \quad (3.4)$$

With this assumptions, an atom moves with a constant acceleration so that an expression can be written for both the velocity  $v(y)$  and also for the magnetic field  $B(y)$ :

$$v(y) = v_0 \sqrt{1 - \frac{y}{y_0}}; \quad B(y) = \frac{\hbar}{1.06 \mu_B} (\delta + kv_0 \sqrt{1 - \frac{y}{y_0}}). \quad (3.5)$$

The laser detuning in EQ. 3.5 can be chosen in order to have a more convenient magnetic field. As shown in FIG. 3.2 the choice to have  $\delta = 0$  implies that the blue laser is resonant with the atoms leaving the Zeeman Slower. In this case the atoms will be pushed away from the radiation pressure of the blue light and will never reach the MOT. Furthermore this choice leads to a very intense magnetic field at the end of the Zeeman Slower hence a high power is required to generate it. Choosing a  $\delta \neq 0$  implies that a constant magnetic field ( $B_{OFF} = \frac{\hbar \delta}{1.06 \mu_B}$ ) is present and causes the laser not to be resonant with the exiting atoms and the total magnetic field to be smaller at the beginning of the Zeeman Slower. The use of a detuned laser, as can be seen in FIG. 3.2 implies that the z projection of the magnetic field assumes both positive and negative values, this means that the atoms change their angular momentum orientation and also the transition change between  $\sigma^+$  and  $\sigma^-$ . This is a so called *spin flip* Zeeman Slower.

Our Zeeman Slower FIG. 3.3 is a spin flip one and the magnetic field is generated by 11 different coils connected in series. The inversion of the magnetic field direction is obtained by inverting the current flow direction in the coils. A smaller coil at the beginning ensures that the magnetic field goes quickly to zero before the beginning of the ZS. The laser beam is focused at the oven position and is shaped in order to have a diameter of roughly 16 mm (the diameter of the CF16 tube) at the entrance of the ZS, so that the saturation intensity is reached at a laser power of  $P \approx 112$  mW. A power of 150 mW is normally used. Assuming the waist evolving linearly in space from 16 to 6 mm, the average saturation parameter is  $s \approx 1.3$ . The laser detuning is around  $-32.8\Gamma$  and, in absence of magnetic field, it is resonant with the atoms moving at a velocity of 480 m/s.

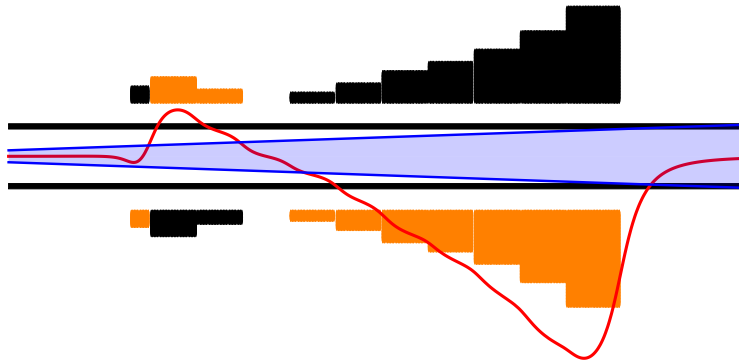


FIGURE 3.3: Scheme of the Zeeman Slower: the orange and black boxes are the cross sections of the different coils with opposite current direction. Superimposed in red there is (solid line) the magnitude of the resulting magnetic field along the longitudinal. The blue shadow represents the laser beam focused at the oven position in the approximation of a linear varying waist. The atoms are moving to the right and the blue light to the left.

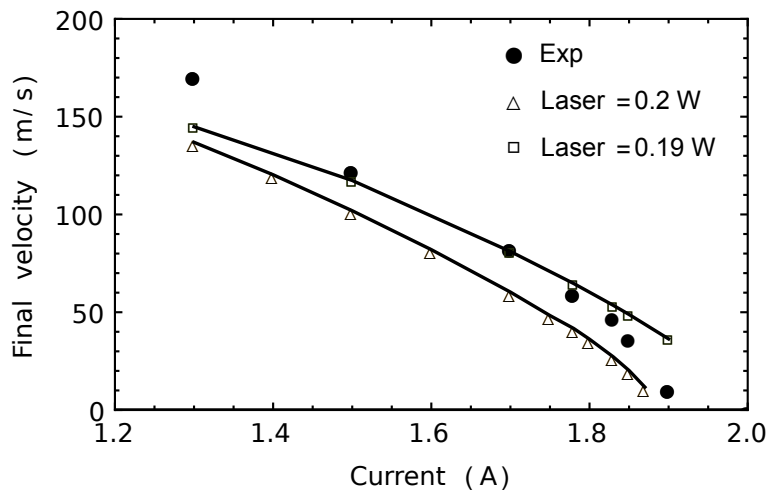


FIGURE 3.4: The final atomic velocities measured and simulated as a function of the Zeeman Slower current. The simulation code has been kindly provided by Prof. Fallani of the University of Florence.

We measured the velocity of the atoms exiting the Zeeman Slower by varying the current circulating in the coils (FIG. 3.4) and we confronted them with simulations. The simulation program was kindly provided by Prof. L. Fallani of the LENS at the University of Florence. In order to measure the final velocity we illuminated the dysprosium beam at the centre of the science cell with two red 626 nm laser beams propagating in the  $xy$  (horizontal) plane, one orthogonally to the atoms direction (in order to be resonant with all the frequency classes) and the other at the same frequency with an angle of  $\theta = 45^\circ$  in order to be sensitive to different velocity at different frequency. We observed the fluorescence emitted by the atoms with a photomultiplier tube directed along the  $z$  axis, in this way we observed only the spontaneous emitted light. The red laser wavelength was scanned until we observed the  $^{162}\text{Dy}$  and  $^{164}\text{Dy}$  peaks, by knowing their frequency separation of 1 GHz, we were able to assign a frequency to the timescale of the oscilloscope, at this point the distance of the slowed atom peak from the  $^{162}\text{Dy}$  peak gave us the frequency shift ( $\Delta$ ) due the atomic velocity and then from  $v = \frac{\Delta}{k \cos \theta}$  we obtained the final velocity.

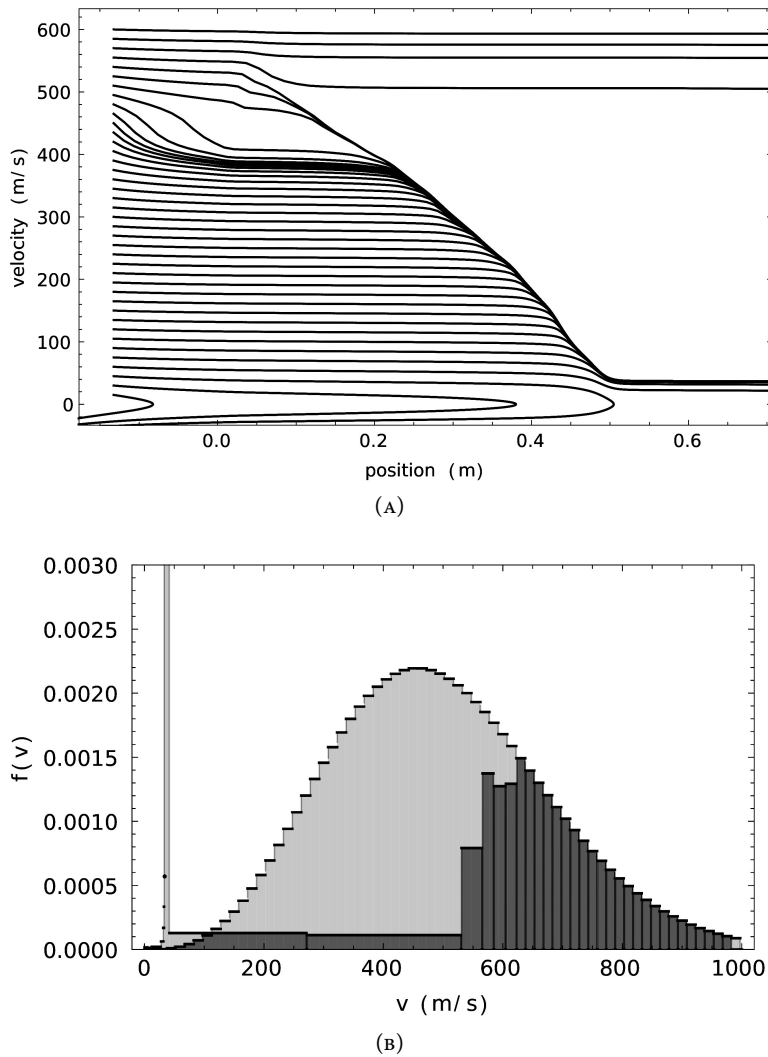


FIGURE 3.5: Results of the Zeeman Slower simulation code for a current of 1.8 A, a laser power of 110 mW and a detuning of  $32.8\Gamma$ . (A) Trajectories in the velocity/position phase space for different classes of initial velocities. One can observe that the highest velocities are not slowed, a large central part of the velocity classes is slowed to a final velocity of  $\sim 36$  m/s and some very slow classes are pushed back. (B) All the slowed velocities are slowed to an average final velocity of 36 m/s this causes a different velocity distribution (light) than the one for an atomic beam EQ. 1.87 (dark) resulting in a big increase in the population in the average final velocity and in conclusion in an effective cooling (the higher peak, its value being  $f(v) = 0.07$ , in order to have a readable graph is cut).

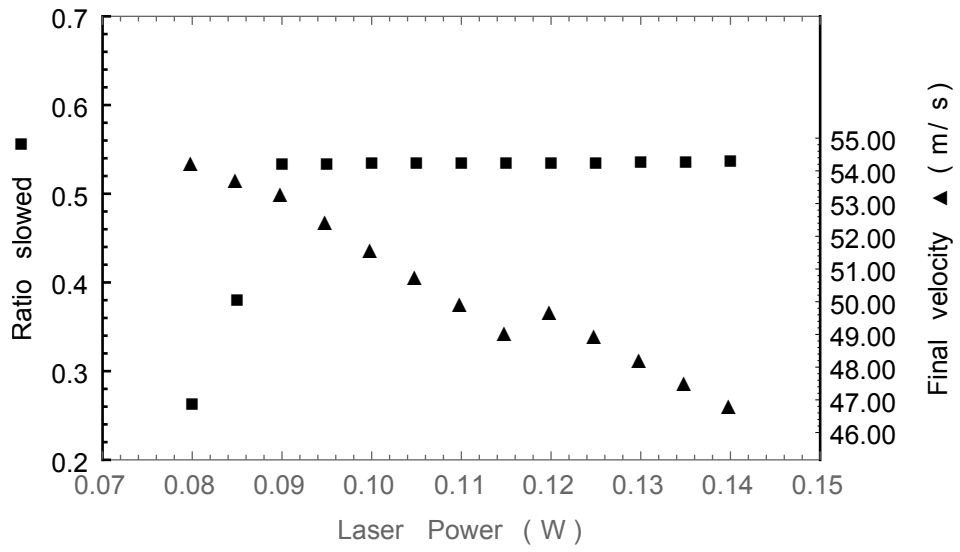


FIGURE 3.6: Simulation results of the fraction of slowed atoms and of the final velocity as a function of the laser power.

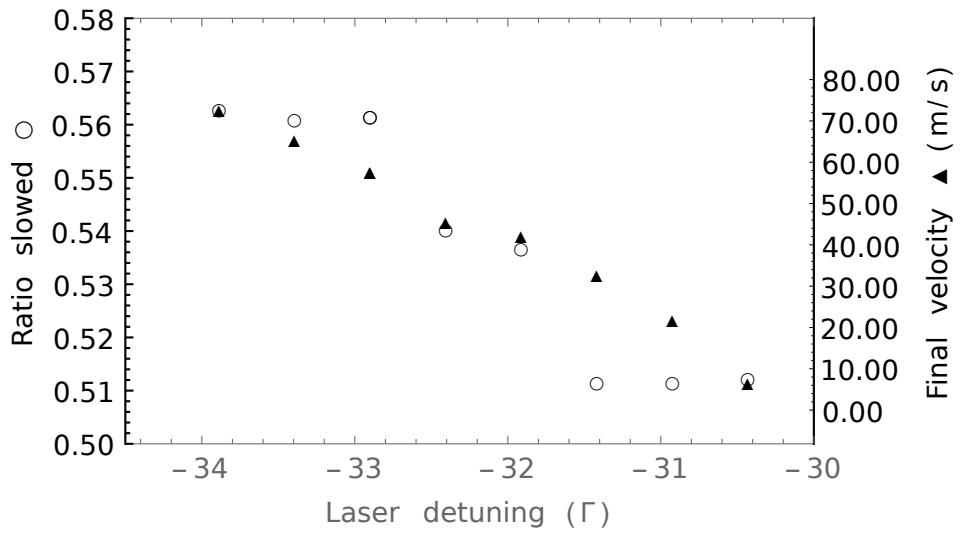


FIGURE 3.7: Simulation results of the fraction of slowed atoms and of the final velocity as a function of the laser detuning.

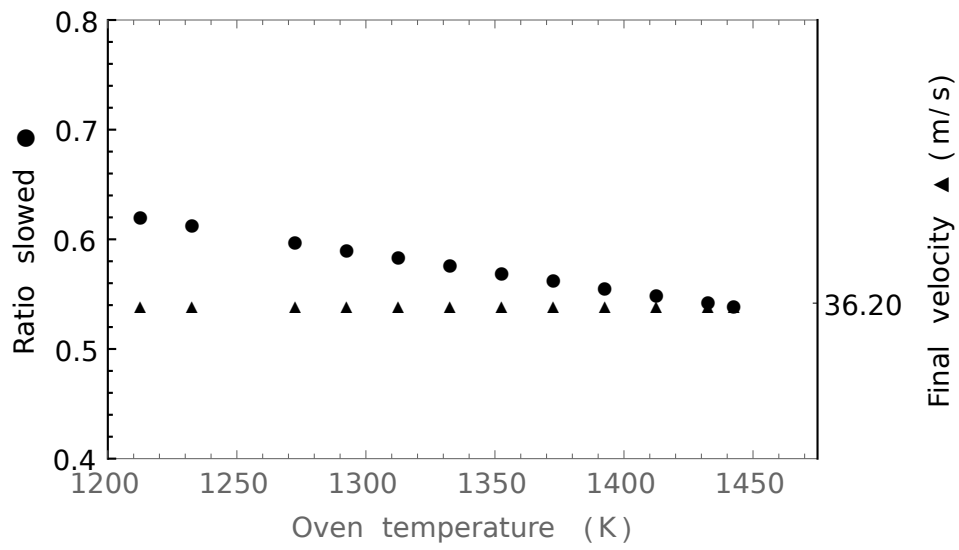


FIGURE 3.8: Simulation results of the fraction of slowed atoms and of the final velocity as a function of the oven temperature (at a current of 1.8 A).

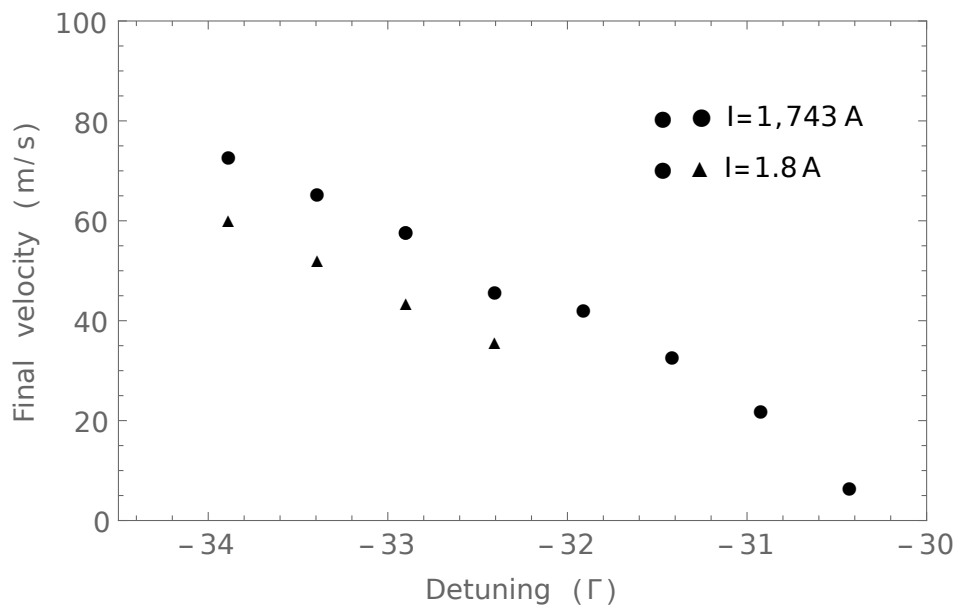


FIGURE 3.9: Simulation results of the final velocity as a function of the laser detuning for two different current values in the ZS.

In our setup the Zeeman Slower is essential to load the MOT in fact the atoms must have a sufficiently low velocity in order to be captured. Furthermore, once trapped in the MOT, the atoms are lost at certain rate so it is also important to have a big flux of slowed atoms. At a first sight, all the atoms moving with a velocity smaller than the initial velocity for which the Zeeman Slower has been designed are slowed because, moving through the apparatus, they reach a region in which the Zeeman shift, due to the magnetic field, make the laser to be resonant and then the atoms exit from the slower at the designed exit velocity, so all the velocity populations  $f(v)$ ,  $v < v_0$  are transferred in the final velocity one (FIG. 3.5). This holds if the magnetic field is shaped exactly as in EQ. 3.5 but the practical realization can't be exact. In order to have some information we performed some additional simulations to find out how the final velocity and the ratio of the atoms slowed vary as a function of the laser power, of the laser detuning, of the oven temperature and of the coils current. The results are plotted in FIG. 3.6 and FIG. 3.7.

Taking into account that at the end of the Zeeman Slower both  $B(y)$  and  $\delta$  are negative, the inversion of EQ. 3.3 and EQ. 3.4 leads to

$$v_f = \frac{1}{k} \left( -\frac{1.06\mu_B}{\hbar} |B(y_f)| + |\delta| \right) \quad v_f = \sqrt{v_i^2 - \frac{2\eta F_{MAX}}{M} y_f} \quad (3.6)$$

In FIG. 3.8 it can be seen how the velocity decreases linearly as the detuning increases as well as the laser power (through the saturation parameter  $s$  in the definition of  $F_{MAX}$  EQ. 3.4). The increase in the number of atoms slowed with increasing the laser power can be referred to the decreasing of  $y_0$  (EQ. 3.4) so that also atoms with higher initial velocity (that would require a bigger  $y_0$ ) can be slowed. Finally, in FIG. 3.9, it can be seen how the current and the detuning are related: once the current is changed, varying the detuning it is possible to obtain the same final velocity.

### 3.3 626 nm MOT

The MOT setup is arranged with three retroreflected laser beams each of which is propagating from the source optical table through single-mode polarization-maintaining optical fibers. Of the three beams, one is propagating along the vertical ( $\hat{z}$ ) direction and the other two in the horizontal  $xy$  plane with an angle of 45 and 135° with respect to the Zeeman Slower axis  $\hat{y}$ . The two coils producing the quadrupole field are parallel to the  $xy$  plane hence the strong axis of the quadrupole field is directed along  $\hat{z}$ . In order to have the correct circular polarization, at the exit of each fiber there are a polarising beam-splitter and a  $\lambda/4$  plate so, after the polarising beam-splitter, the linearly polarised light is turned circular by the plate. Before entering into the cell, the three beams are collimated by a  $f = 150$  mm lens to a waist of 13.2 mm. After exiting from the cell, the beams encounter another  $\lambda/4$  plate so, being retroreflected they pass through the plate twice and, in this way, the helicity is inverted as shown in FIG. 1.3. A total power of 150 mW in the three beams (corresponding to  $I > 200I_s$  per beam) is used during the MOT loading.

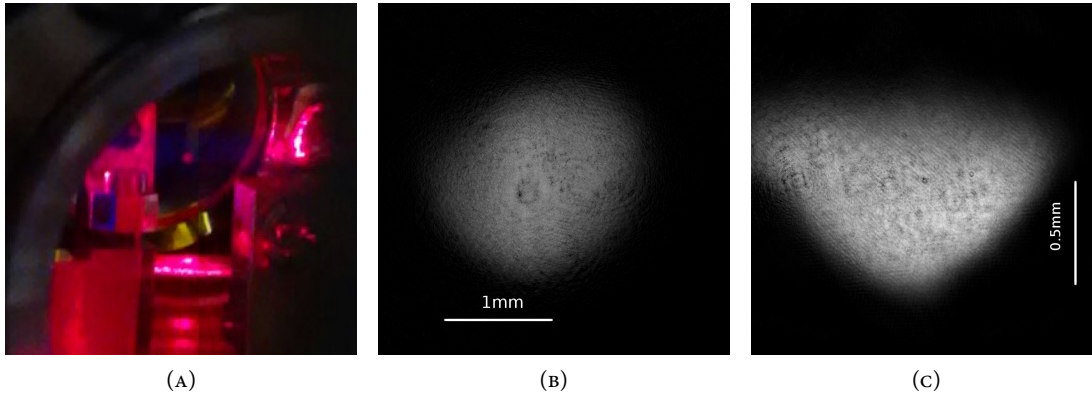


FIGURE 3.10: (A): Picture of one of the first MOT achieved (the small red dot at the center). (B): vertical MOT absorption image, the circular shape reveals the symmetry with respect to the  $\hat{z}$  axis of the confining forces. (C): Horizontal MOT absorption image, the image has been rotated so to have the  $\hat{z}$  axis in the vertical direction; it can be seen how the gravity influences the cloud shape. In (b,c) the difference in size of the two images is due principally to the differences in the magnification factor ( $1.6\times$  and  $3.2\times$  for the vertical and horizontal imaging beam respectively) the brightness of each pixel is proportional to  $\ln \frac{I_0}{I}$ .

### 3.3.1 MOT IMAGING

The MOT absorption imaging can be performed either with an horizontal beam or with a vertical one. The latter has a higher resolution ( $\sim 2.5\mu\text{m}$ ). Images are then fitted to extract the atom number, the peak density and the atomic temperature.

Although the assumptions used in SEC. 2.5 are rigorously verified only in a optical dipole trap, given the elastic forces in EQ. 1.48, the same fit function can be used in the MOT imaging, especially in the  $xy$  images FIG. 3.10 where gravity doesn't play any role (as will be explained in the next section).

Sadly we recognized an error in our program imaging due to a misplacement of the magnification factor in the formulas leading to a miscalculation of the absolute number of atoms. Therefore, in the nex two sections the number of atoms is incorrect, overestimated by a factor of 4.

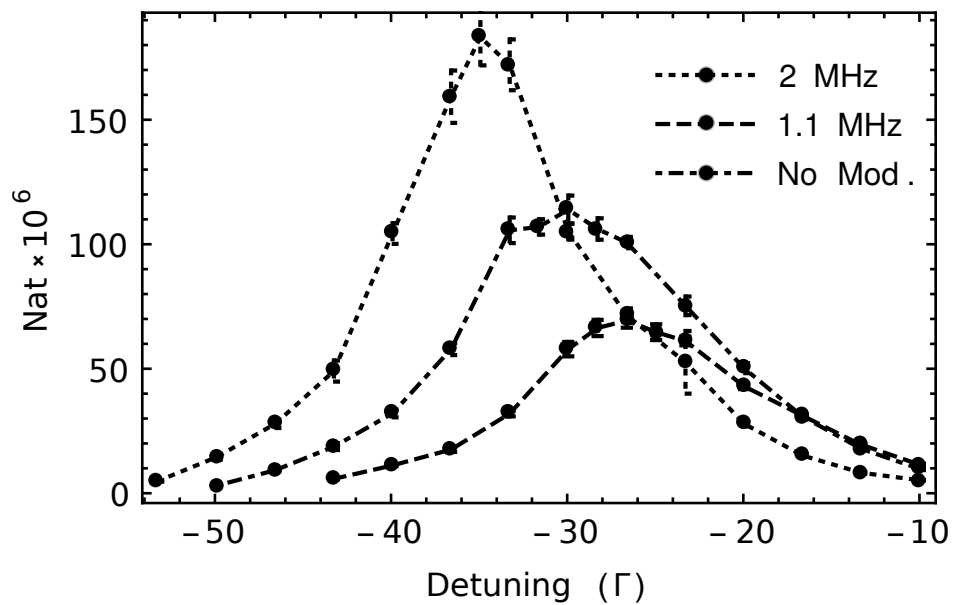


FIGURE 3.11: MOT number of atoms as a function of the detuning and frequency modulation (the frequency of the modulation was 135 kHz as in [10] and very similar to [21]). The lines connecting the point are to be intended as simple visual aids. The absolute number of atoms isn't correct as explained in the text. The modulated width is indicated in the figure.

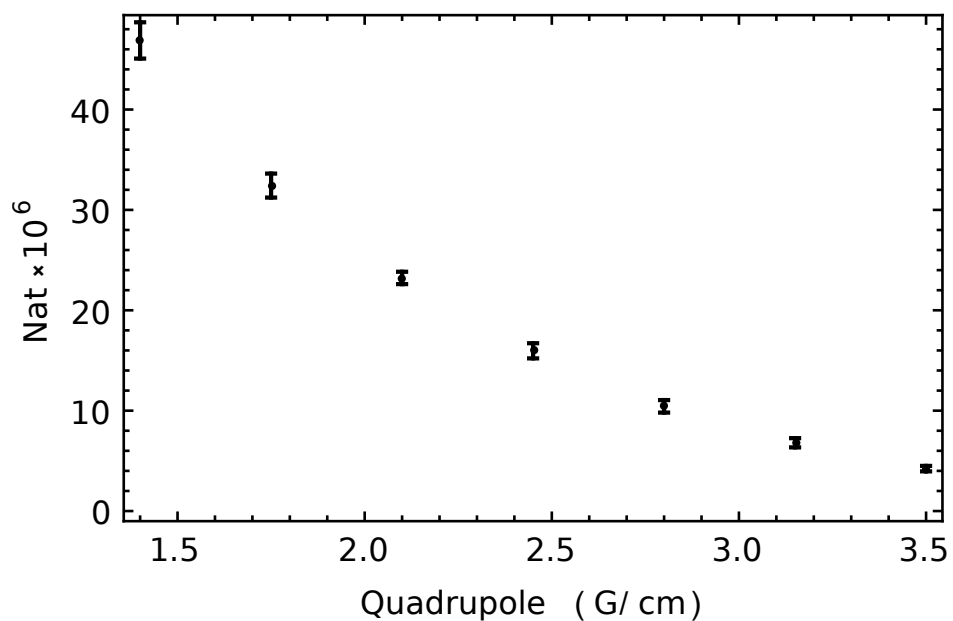


FIGURE 3.12: MOT number of atoms as a function of the magnetic field gradient. The atom number reported in this graph as well as all the others are obtained after the compression phase in the c-MOT. The absolute number of atoms isn't correct as explained in the text.

### 3.3.2 MOT DETUNING AND RELATED CHARACTERISTICS

The use of the “red” 626 nm transition for the MOT formation, given its linewidth of 136 kHz (TAB. 1.2) implies a low enough Doppler temperature to allow the direct loading of a dipole trap but, on the other hand, implies some peculiarities in the MOT detuning during the loading phase and in its equilibrium position. As an example see FIG. 3.10.

The measured results of the number of atoms captured as a function of the detuning are reported in FIG. 3.11 for different amplitudes of frequency modulation. In FIG. 3.12 the number of atoms as a function of the magnetic field gradient is reported.

Restricting the discussion along the  $\hat{z}$  axis, an atom is subjected both to the radiative and the weight forces which have to compensate each other in order to maintain the atom at the equilibrium. In this condition the atom moves to a region where the Zeeman shift, due to the magnetic field gradient, breaks the balance between the forces exerted by the two counter-propagating vertical laser beams resulting in a neat force opposing the weight force. This situation, where one of the two counter propagating laser beams is off resonant, can be better described by Zeeman Shift dependent radiative force (EQ. 1.40) rather than the expression for the MOT (EQ. 1.46). This case has been studied in detail in [10] and, although with a different atom and for a “narrower” transition, in [2]. For an atom at rest and neglecting the force arising from the static magnetic field gradient  $\mu b$  (which is at least one order of magnitude smaller) the two forces remaining at play have to satisfy the relation  $\mathbf{F}_R + m\mathbf{g} = \mathbf{0}$  resulting in a local detuning  $\Delta_{\text{LOC}}$  sum of the laser detuning and the Zeeman shift given by [10]:

$$\Delta_{\text{LOC}} = -\frac{\gamma}{2}\sqrt{(\eta-2)s-1}; \quad \eta = \frac{\hbar k\gamma}{2mg} \quad (3.7)$$

In addition, as observed in [10], the displacement of the centre of the MOT at a finite distance below the centre of the quadrupole magnetic field imply that the atoms are constantly at a non zero magnetic field and so, as for the Zeeman Slower, the use of a circularly polarised light gives rise to optical pumping into the  $J = 8, m_j = -8$  state. With this assumption, the equilibrium position  $z_{\text{EQ}}$  depends on the laser detuning  $\delta$ , the magnetic field gradient  $b$  and the saturation parameter  $s$ . In our configuration, can be written as

$$z_{\text{EQ}} = \frac{\hbar}{\Delta_\mu b} \left( \delta + \frac{\gamma}{2} \sqrt{s(\eta-1)-1} \right) \quad (3.8)$$

where  $\Delta_\mu = (-9g_9 + 8g_8)\mu_B = -1.69\mu_B$ ,  $b$  is the magnetic field gradient. The light circular polarisation and the magnetic field gradient are adjusted in order to result in  $\Delta_\mu b > 0$ .

Increasing the red laser detuning ( $\delta < 0$ ) increases the displacement of the MOT centre farther below the Zeeman Slower laser beam,  $z_{\text{EQ}} < 0$  in EQ. 3.8. In this way losses due to the blue light [12, 21] are reduced resulting in an increase in the number of atoms loaded by a factor of three, as shown in FIG. 3.11. In addition to the vertical displacement, the far detuning (in EQ. 1.23  $F_R$  scales as  $1/\delta^2$ ) implies a decrease of the elastic force in EQ. 1.46 and as a consequence an increase of the MOT size. A further increase in the detuning leads to a smaller final number of atoms due to the finite size of the laser beams. For a similar reason, there is a dependence of the number of atoms on the magnetic field gradient: increasing its magnitude decreases the width of the geometrical

region where the resonance condition

$$\delta + kv - \frac{\Delta\mu}{\hbar} \mathbf{b}z = \Delta_{\text{LOC}} \quad (3.9)$$

holds, resulting in a smaller overlap between the slowed atoms flux emerging from the Zeeman Slower leading, at the end, to fewer captured atoms. As a final observation, given the much narrower line-width of the 626 nm transition compared to the 421 nm one, the frequency modulation of the red laser allows to satisfied the resonance condition EQ. 3.9 trough a wider interval of the velocities distribution around the final average velocity  $v_f$  in EQ. 3.6. An analytic analysis won't be reported here but a graphical explanation can be found in FIG. 1.2.

Given the size of the cloud during the loading phase, in order to obtain usable images as in FIG. 3.10, the MOT has to be compressed ramping down the detuning typically to  $\delta = -6\Gamma_{626}$  and the laser intensity down to  $I = 0.3I_s$  in 40 ms. This operation is quite critical, decreasing the detuning moves the MOT toward the quadrupole centre and so toward smaller magnetic field hence, if the intensity isn't appropriately reduced simultaneously, the polarization of the sample is easily lost.

### 3.3.3 MOT POPULATION TEMPORAL EVOLUTION

Once we determined the best choices for the detuning, magnetic field gradient and frequency modulation we studied the MOT loading and holding time. Once an atom is captured in the MOT region it doesn't remain trapped for an indefinite amount of time but can be lost as a result of multiple events. The evolution of the MOT population during the loading phase is determined by the *capture rate*  $R$  (the number of atoms captured each second) which can be considered constant, and by the rate at which atoms are lost. The study of the loading phase is simply done by starting at  $t = 0$  the loading process and then taking absorption images at successive times  $t$  until the population reaches a steady state. The MOT *lifetime* study is done letting the population to reach the steady state then, at  $t = 0$  a shutter blocks the atoms flux. During the lifetime study the Zeeman Slower beam is turned off and finally absorption images are taken at successive times  $t$ . The measurements obtained are reported in FIG. 3.13. The presence or absence of the ZS (see [21]) has a deep influence on the MOT lifetime. As said, once the atoms are trapped, they can leave the trap after different types of events, the first one is the collision with the background gas that is in thermal equilibrium with the chamber walls so the particles are moving at velocities well beyond the ones that can be trapped. As a result, for each collision, a trapped atom leaves the MOT, assuming negligible the probability that an escaping atom collides with a trapped atom. This process occurs with a probability dependent on the number of atoms of the background gas in the MOT region (and hence on the background pressure, assuming the pressure constant in the chamber) and on the density of the trapped atoms and, because it involves one trapped atom at a time, is called a *one-body loss*. In this way the average MOT density variation depends on the density itself leading to a time dependence as

$$\bar{n}(t) = \bar{n}_0 e^{-\frac{t}{\tau}} \quad (3.10)$$

where  $\bar{n}_0 = \frac{1}{2\sqrt{2}} \frac{N}{V}$  is the initial average density and  $\tau$  the MOT decay time. Among other processes that can lead to atom losses of interest are the so called *two body* or *density dependent* losses

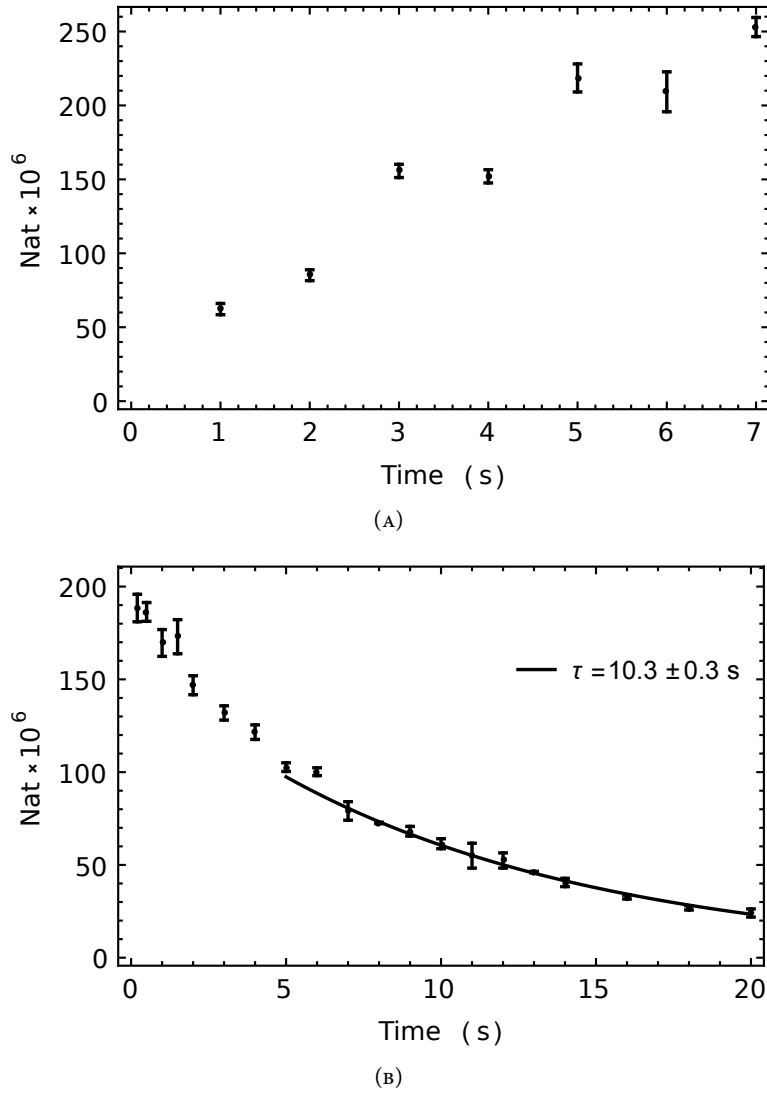


FIGURE 3.13: (A): MOT number of atoms as a function of the loading time, the capture rate at early times is  $R=4.6 \times 10^7$  /s and the loading time is 10 s. (B) MOT number of atoms as a function of the holding time and a single exponential fit superimposed resulting in a time decay constant of  $\tau = 10.3 \pm 0.3$ s. In both cases the detuning was  $\delta = -35\Gamma_{626}$  and the magnetic field gradient about 1.4 G/cm. The absolute number of atoms isn't correct as explained in the text.

that, because imply a two trapped atoms collision, it depends on the squared average population density with a general law [29]

$$\frac{d\bar{n}}{dt} = \frac{\bar{n}}{\tau} - \beta_0 \bar{n}^2 \quad (3.11)$$

where  $\beta_0$  depends on the particular process involved. Our results of the MOT population are reported FIG. 3.13. Data of `gr:mottime(B)` are fitted with EQ. 3.10 but the data can be correctly fitted just for times longer than 5 s meaning that at large population we are in presence of two body losses that became less relevant while the trapped population decrease leaving the one-body losses to predominate.

### 3.3.4 MOT DIMENSIONS AND TEMPERATURE

In order to transfer the greater number atoms from the MOT to the optical dipole trap the MOT temperature and size are of particular interest. From our measurements<sup>1</sup> we observed for the compressed MOT dimension (*in situ*) varying from 400 to 550  $\mu\text{m}$  (depending on the number of atoms) in the  $\hat{x}$  and  $\hat{y}$  directions and around 300  $\mu\text{m}$  (with much smaller variations) in the  $\hat{z}$  direction.

A temperature measurement is done using EQ. 2.8: once known the *in situ* dimension, the MOT is left to freely expand for a determined period of time, 30 ms in our case, then the new dimensions are measured and finally, inverting EQ. 2.8, the temperature is obtained. We observed a MOT temperature of 20  $\mu\text{K}$ .

### 3.3.5 OVEN TEMPERATURE AND MOT POPULATION

From what reported in SEC. 1.8, an increase in the oven temperature, should lead to an increase in the atom density in the atomic beam and, in the end, in an increase in the number of atoms captured in MOT. Surprisingly the results of our measurement of the MOT population at a constant time in FIG. 3.14 exhibits a maximum around 1130  $^{\circ}\text{C}$ . In EQ. 1.94, the temperature dependence is given from the exponential term that is monotonic with respect to  $T$ . A possible explanation is that at higher temperature the atom density became so high that the effusive regime underlying all the description fails.

### 3.3.6 OTHER MOTS IN LITERATURE

---

<sup>1</sup>These values are obtained with the corrected imaging program and are correct.

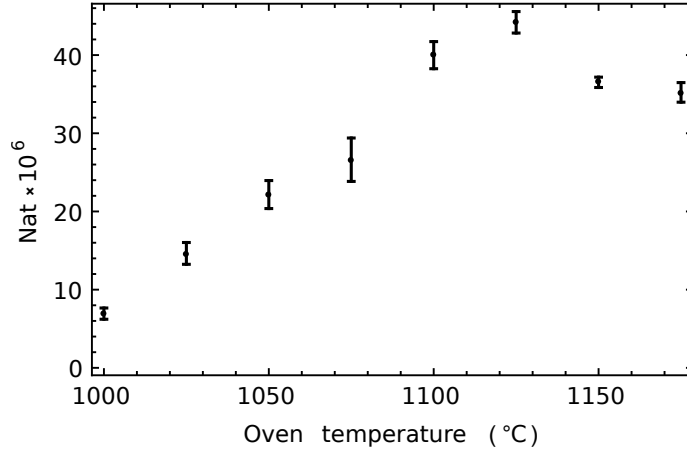


FIGURE 3.14: Number of atoms captured by the MOT as a function of the oven temperature. We expected the number of atoms to be a monotonic function of the oven temperature but we observed a maximum at 1130 °C. The atomic number reported here is correct.

TABLE 3.1: Principal characteristics of the various MOT I found in the literature. The use of the 421 nm transition by the Stanford group results in big differences in almost every aspect of the MOT. Using the 626 nm transition leads to very similar laser detuning in the loading phase, while for larger light intensities the final temperatures are higher.

Loading phase				
	us	Stuttgart	ENS-PSL	Stanford
$\lambda$ (nm)	626	626	626	421
Waist (mm)	13.16	22.5	20	11
b (G/cm)	1.4	3	1.71	?
T load (s)	10	4	6	0.05
I ( $I_s$ )	200	370	50	0.2
$\delta$ ( $\Gamma$ )	-35	-35	-31	-1.2
$\Delta\mu$ ( $\Gamma$ )	15	?	45	0
Nat $\times 10^8$	1?	1.5	3	2.5
Temp. ( $\mu$ K)	?	500	15	1000
Compressed MOT				
	us	Suttgart	ENS-PSL	Stanford
$\lambda$ (nm)	626	626	626	421
Waist (mm)	13.16	22.5	20	11
b (G/cm)	1.4	1.5	–	–
Duration (ms)	40	170	430	–
I ( $I_s$ )	0.4	0.15	?	–
$\delta$ ( $\Gamma$ )	-6	-2.75	?	–
$\Delta\nu$ ( $\Gamma$ )	15	?	?	–
Nat $\times 10^8$	1?	1	?	–
Temp. ( $\mu$ K)	20	6	?	–

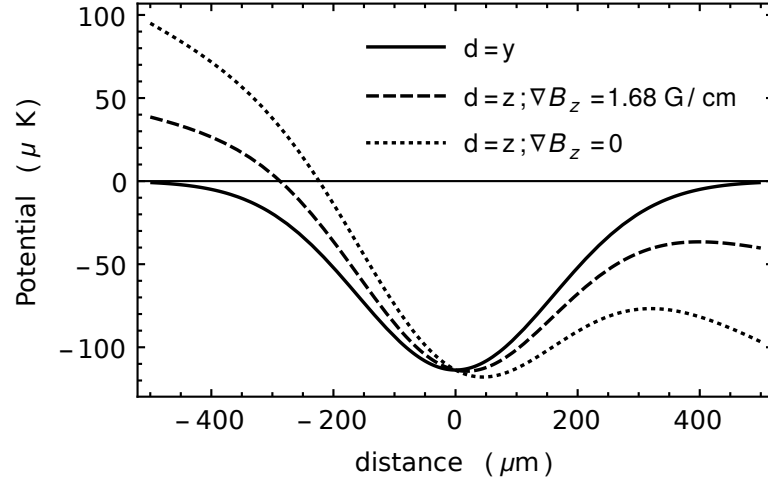


FIGURE 3.15: Resonator optical dipole trap depth calculation for a laser power  $P = 0.6\text{W}$ , a waist  $w_0 = 320\mu\text{m}$ . Plot of the potential as a function of  $y$  or  $z$  ( $x = 0$ ) and  $b = 1.68\text{G/cm}$  and  $b = 0$ ; the resulting trap frequencies in the  $b = 1.68\text{G/cm}$  case are:  $\omega_x = 98\text{kHz}$ ,  $\omega_y = 73.3\text{Hz}$ ,  $\omega_z = 72.9\text{Hz}$ , the vertical depth is  $72\mu\text{K}$  while along  $\hat{y}$  and  $\hat{x}$  is  $107\mu\text{K}$ . For  $b = 0$  the vertical depth is  $35.5\mu\text{K}$  while in the other directions is unchanged.

### 3.4 RESONATOR OPTICAL DIPOLE TRAP

In order to start the forced evaporative cooling, once captured by the MOT, atoms have to be confined by a conservative potential well, hence in an optical dipole trap.

The optical dipole trap should have a waist roughly of the MOT dimensions  $w \simeq 300\mu\text{m}$  and should be deep enough to confine atoms at  $20\mu\text{K}$ . Given these conditions, with a  $1064\text{nm}$  laser, the power required is around  $350\text{W}$ . This power can be reduced to more reasonable values using an high finesse optical resonator.

We adopted a symmetric nearly planar optical resonator composed of two mirror of the same reflectivity  $\mathcal{R} = 99\%$  at a distance of  $L = 88.3\text{mm}$  and with curvature radius  $R = 3\text{m}$ . The waist inside the resonator can be calculate by [32]:

$$w_0 = \sqrt{\frac{\lambda L}{\pi} \left( \frac{1 + L/R}{4L/R} \right)^{1/4}}; \quad w = \sqrt{\frac{\lambda L}{\pi} \left( \frac{1}{1 - (1 - L/R)^2} \right)^{1/4}} \quad (3.12)$$

where  $w_0 = 270\mu\text{m}$  is the minimum waist (at the centre of the cavity) and  $w = 320\mu\text{m}$  is the waist at the mirror. For a gaussian beam propagating along the  $\hat{x}$  axis, the electric field can be written as [32]

$$E(x, y, z) = E_0 e^{-ik \left( x + \frac{y^2 + z^2}{2} \left( \frac{1}{R} - i \frac{\lambda}{\pi w^2(x)} \right) \right)} \quad (3.13)$$

where  $k = \frac{2\pi}{\lambda}$  and  $R$  is the curvature radius of the wave front. Given the big curvature radius of the mirrors, equal to  $R$  at the mirror itself, the previous expression can be approximated by

$$E(x, y, x) \simeq E_0 e^{-\frac{y^2 + z^2}{w^2(x)}} e^{-ikx}. \quad (3.14)$$

The amplitude of the electric field after the passage through the first mirror is multiplied by  $[6]$   $\sqrt{1-\mathcal{R}}$  then, after the first reflection on the second mirror is again multiplied by  $\sqrt{\mathcal{R}}$ , taking into account the opposite direction of propagation after each reflection, the total electric field inside the cavity is given by:

$$E(x, y, z) \simeq E_0 e^{-\frac{y^2+z^2}{w^2(x)}} \sqrt{1-\mathcal{R}} \sum_{m=0}^{\infty} \left( e^{(-)^m i k x} \mathcal{R}^{m/2} \right) = E_0 \frac{e^{i k x} + \sqrt{\mathcal{R}} e^{-i k x}}{\sqrt{1-\mathcal{R}}} e^{-\frac{y^2+z^2}{w^2(x)}}. \quad (3.15)$$

In order to describe an optical dipole trap we are interested in the intensity of the electromagnetic field (SEC. 1.5.1) and the previous expression, in terms of light intensity, is obtained by taking the (squared) modulus:

$$I(x, y, z) \simeq \frac{2P}{\pi w^2(x)} \frac{4\mathcal{F}}{\pi} \cos^2(kx) e^{-2\frac{y^2+z^2}{w^2(x)}} \quad (3.16)$$

where  $I_0 = \frac{2P}{\pi w^2}$  is the intensity of the laser beam,  $\mathcal{F} = \frac{\pi\sqrt{\mathcal{R}}}{1-\mathcal{R}}$  is the finesse of the cavity (that can actually be measured) and the substitution  $\mathcal{R} = 1$  has been made. The cavity has a finesse of 1050 (see in sec. 2.4.1) and the light intensity inside the resonator is multiplied by a factor varying between 0 and  $\frac{4\mathcal{F}}{\pi}$  allowing us to use a 1 W laser to obtain a trap depth of nearly 200  $\mu\text{K}$ . Furthermore the optical dipole potential is obtained by multiplying the light intensity by the atomic polarizability (see SEC. 1.5.1) and the  $\cos^2(kx)$  term (due to the interference inside the cavity) making the  $\hat{x}$  dependence of the dipole potential rather different than in the other two directions. In addition, for the  $\hat{z}$  direction both the gravity and the force arising from the magnetic field gradient have to be taken into account leading to an expression for the trap potential:

$$U(x, y, z) = -\alpha \frac{8P\mathcal{F}}{\pi^2 w_0^2} \cos^2(kx) e^{-2\frac{y^2+z^2}{w_0^2}} + (Mg - \mu b)z \quad (3.17)$$

where  $\alpha$ ,  $M$  and  $\mu$  are respectively the dysprosium polarizability, mass and magnetic moment;  $g$  is the gravity acceleration and, in addition, the waist inside the resonator is supposed to be constant and equal to  $w_0$ . In a similar way described in [13] it could be calculated the Taylor series of EQ. 3.17 at the minimum of the potential  $\mathbf{r}_c$

$$U(x, y, z) \simeq U(\mathbf{r}_c) + \frac{1}{2} \sum_{i,j=1,2,3} \frac{\partial^2 U(\mathbf{r}_c)}{\partial x_i \partial x_j} (x_i - r_{ic})(x_j - r_{jc}) \quad (3.18)$$

in order to obtain an harmonic approximation of the potential:

$$U(x, y, z) = \frac{1}{2} M \omega_x^2 x^2 + \frac{1}{2} M \omega_y^2 y^2 + \frac{1}{2} M \omega_z^2 z^2 \quad (3.19)$$

where, in the basis where  $\frac{\partial^2 U(\mathbf{r}_c)}{\partial x_i \partial x_j}$  is diagonal, it holds

$$\omega^2 = \frac{1}{M} \frac{\partial^2 U(\mathbf{r}_c)}{\partial x^2}. \quad (3.20)$$

In our case, calculations will be rather complicated and of limited help, nevertheless some characteristics of  $\omega_x$  and  $\omega_y$  can be shown: posing  $A = \alpha \frac{4P\mathcal{F}}{\pi^2 w_0^2}$ , for the first derivatives we have

$$\frac{\partial U}{\partial x} = 2k \sin(2kx) A e^{-2\frac{y^2+z^2}{w_0^2}}; \quad \frac{\partial U}{\partial y} = \frac{8y}{w_0^2} \cos^2(kx) A e^{-2\frac{y^2+z^2}{w_0^2}} \quad (3.21)$$

TABLE 3.2: Optimal compressed MOT detuning values for different laser power.

Nat $\times 10^6$	Temp $\mu\text{K}$	Res. Power (%)	$\Delta$ ( $\Gamma$ )
$30 \pm 5$	$29 \pm 2$	100	$8.2 \pm 0.5$
$31 \pm 5$	$25 \pm 2$	80	$7.9 \pm 0.5$
$36 \pm 5$	$23 \pm 2$	60	$7.7 \pm 0.5$
$28 \pm 5$	$14 \pm 2$	50	$7.4 \pm 0.5$
$24 \pm 5$	$10 \pm 2$	40	$7.5 \pm 0.5$

and the  $x$  derivative vanishes for  $x = m\lambda/4$  while the  $y$  derivative vanishes for  $y = 0$  or  $x = (2m + 1)\lambda/4$ ,  $m \in \mathbb{N}$ , so  $\mathbf{r}_c = (0, 0, z_c)$ . For the second derivatives we have:

$$\frac{\partial^2 U}{\partial x^2} = 4k^2 \cos(2kx) A e^{-2\frac{y^2+z^2}{w_0^2}}; \quad \frac{\partial^2 U}{\partial y^2} = \left( \frac{8}{w_0^2} - \frac{32y^2}{w_0^4} \right) \cos^2(kx) A e^{-2\frac{y^2+z^2}{w_0^2}} \quad (3.22)$$

and in  $\mathbf{r}_c = (0, 0, z_c)$  we have

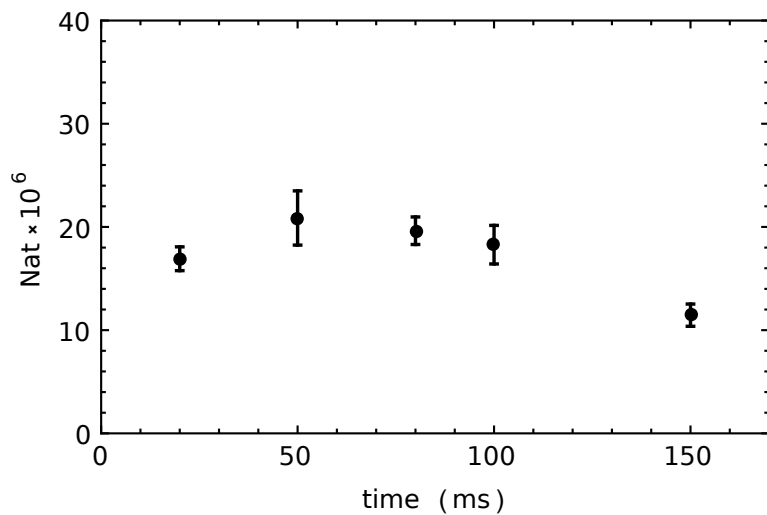
$$\omega_x^2 \propto \frac{\alpha \mathcal{F} P}{w_0^2} k^2; \quad \omega_y^2 \propto \frac{\alpha \mathcal{F} P}{w_0^4}. \quad (3.23)$$

Given  $k \simeq 6 \times 10^6$  and  $w_0 \simeq 300 \times 10^{-6}$  we expect a  $\omega_x/\omega_y$  ratio of the order of  $4 \times 10^3$  hence atoms are much more tightly confined in the  $x$  direction rather than in the other two and due to gravity  $\omega_z$  is expected to be even smaller than  $\omega_y$ .

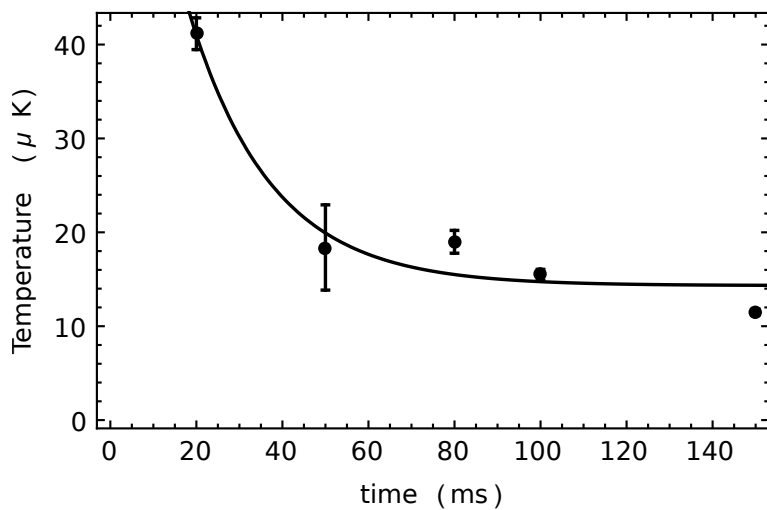
Calculation using EQ. 3.18 are reported in FIG. 3.15 for a laser power of  $P = 0.6\text{W}$ , a waist of  $w_0 = 320\mu\text{m}$  and a magnetic field gradient of  $b = 1.68\text{G/cm}$ . The resulting vertical trap depth is  $U(10^6/k_b) = T_z = 71.3\mu\text{K}$ . and the resulting frequencies are  $\omega_x = 98\text{kHz}$ ;  $\omega_y = 73.3\text{Hz}$  and  $\omega_z = 72.9\text{Hz}$ .

### 3.5 MOT TO RESONATOR OPTICAL DIPOLE TRAP TRANSFER

Atoms are loaded from the MOT into the resonator optical dipole trap. Although the resonator permits to have a quite large waist it is still smaller than the compressed MOT hence a certain amount of atoms will be lost. Furthermore, due to the high light intensity, the MOT is perturbed during the compression stage that is a rather delicate phase that can easily end in a copious loss of atoms. The process involves a fine tuning of the final detuning and of the light intensity of the cMOT, the light intensity injected in the optical cavity and the duration of the time for which the MOT is superimposed to the resonator. In fig. 3.17 (A,B) are reported both the number of atoms and the temperature of the atoms as a function of the superimposing time. The MOT was compressed with the resonator power at 50% and, after varying the superimposing time, the MOT was turned off and atoms were left in the resonator for 50 ms; then an absorption image was taken with a time of flight of 13 ms. From the graph it can be seen that atoms were heated from the  $20\mu\text{K}$  in the cMOT then cooled down again until an estimate temperature of roughly  $15\mu\text{K}$ .



(A)



(B)

FIGURE 3.16: Number (A) and temperature, (B) of the atoms trapped in the resonator as a function of the superimposing time with both the compressed MOT and the resonator beams on. The cMOT intensity was ramped down to  $0.5I_s$  and the resonator intensity was 0.5 W. Superimposed in (B) is the fit with  $y = A + Be^{-t/\tau}$ , the time constant resulting is  $\tau = 19 \pm 9$  ms and the constant value  $A = 14 \pm 2 \mu\text{K}$ .

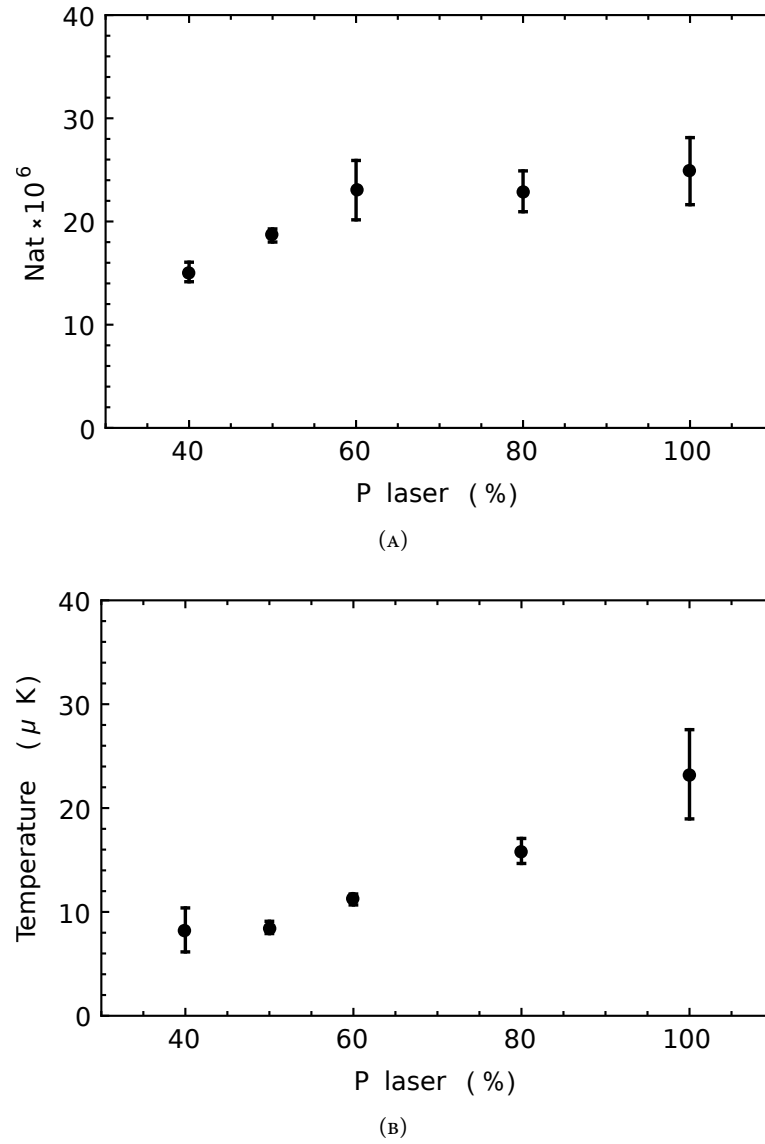


FIGURE 3.17: *Number of atoms (A) and temperature (B) as a function of the resonator power (100%=1 W). Atoms in the MOT had an initial temperature of around 20  $\mu$ K. After an initial evaporation that lowers this temperature, increasing the laser power beyond the limit required to hold them results in an heating of the atoms. Imaging was performed after atoms were left 50 ms in the resonator.*

We can notice that a high light intensity in the optical cavity assures that atoms are bounded by a higher force but, on the other hand, if atoms are already colder than the trap depth, there is no gain in the process efficiency. In the graphs in fig. 3.17 (C,D) it can be seen how increasing the laser intensity over 60% (roughly 600 mW) there is an actual heating due to the increasing the scattering rate with the light intensity. In addition we noticed that for each laser power there is an optimal MOT detuning that causes minimum loss of atoms and a lower final temperature; this is probably due to the light shift [26] of the 626 nm transition in the presence of the high intensity 1064 nm light. Our results are reported in TAB. 3.2.

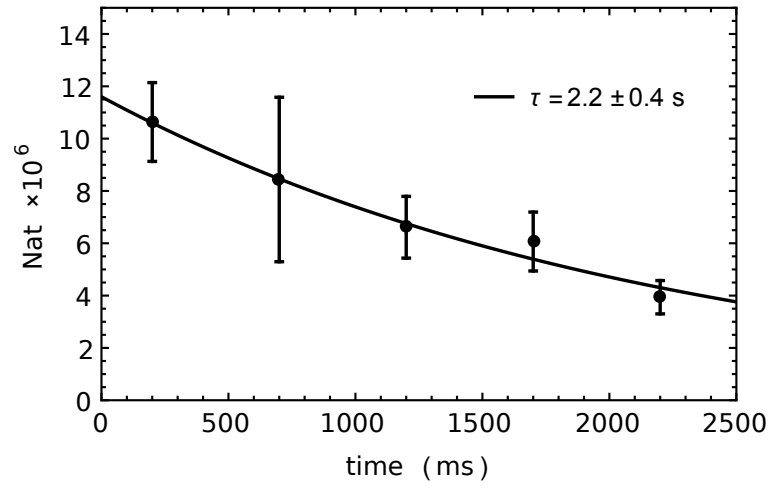
After some studies it was found that by changing the polarization of the light injected in the cavity from circular to linear, the transfer of atoms from the MOT to the cavity trap is more efficient and robust, in particular for certain angle in the light polarization. This fact can be related to the light-shift induced by the 1064 nm radiation to the dysprosium state excited by the MOT light: keeping in mind that atoms are polarised along the vertical direction this anisotropy arises from the tensor part in the dysprosium excited state polarizability. This feature is actually being studied.

### 3.5.1 THE RESONATOR TRAP LIFETIME

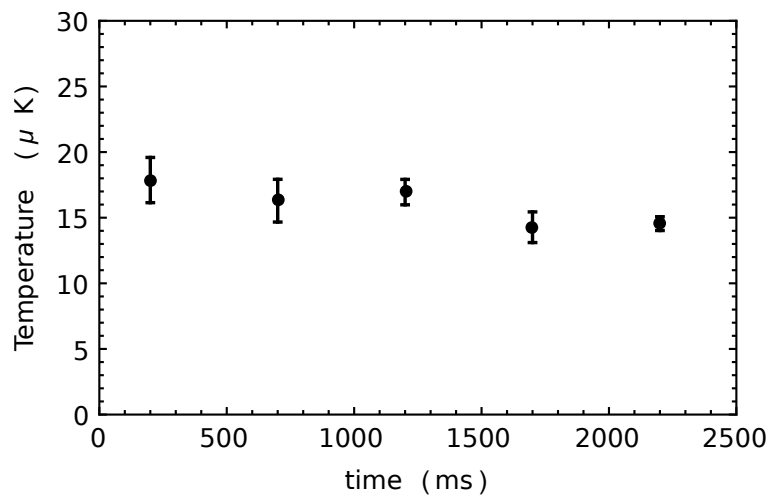
Once the optimal parameters for the resonator loading were established, we studied the lifetime of the trap at the full power,  $P \approx 1$  W. The results are plotted in FIG. 3.18 the lifetime obtained is  $\tau = 0.92$  s and the temperature was stable at  $T \approx 20$   $\mu$ K. In order to work at lower resonator laser power, we decided to compensate the gravity using the quadrupole magnetic field. As a consequence of the polarization of our MOT (SEC. 3.3.2) we know that atoms cycle between the  $J = 8$   $m_J = -8$  and the  $J' = 9$   $m_{J'} = -9$  states so  $\Delta_m u = \mu_B(-9g_9 + 8g_8) < 0$  but, at the same time, at red MOT detuning it has to be fulfilled the condition  $\Delta_\mu b > 0$  (EQ. 1.40) and, in the end,  $b < 0$ . Applying a constant magnetic field, once the MOT is turned off, the atoms decay into the  $J = 8$   $m_J = -8$  and remain polarized in this state with  $\mu = 9.93\mu_B > 0$ . From

$$\mu b = -Mg \tag{3.24}$$

(where  $g$  is the gravity acceleration and  $M$  the dysprosium mass) it follows that we have to invert the direction with respect to that used during the MOT stage, in order to compensate gravity. The quadrupole magnetic field needed to be inverted in order to have  $b > 0$  and it was done simply inverting the current flow. From EQ. 3.24 it follows that the required magnetic field gradient is  $b = 2.88$  G/cm. In FIG. 3.18 are plotted the lifetime and temperature with the gravity compensation. Without the gravity compensation the measured lifetime was  $\sim 1$  s. The lifetime is longer with gravity compensation because with the same laser power, and so with the same scattering rates, the vertical trap depth is higher avoiding vertical losses.



(A)



(B)

FIGURE 3.18: (c) Number of atoms as a function of time but with  $b$  inverted during in the MOT phase in order to compensate gravity; the fit revealed a lifetime of  $\tau = 2.2 \pm 0.4$  s, without compensating for the gravity the resulting lifetime is  $1.0 \pm 0.2$  s.

TABLE 3.3: *Principal characteristics of the three optical dipole traps.*

	Vertical waist ( $\mu\text{m}$ )	Horizontal waist ( $\mu\text{m}$ )	Power (W)	Angle ( $^\circ$ )	Polarization
Resonator	320.5	320.5	1 (240)	$8^\circ$	linear
ODT1	$40.6 \pm 2.0$	$40.6 \pm 2.0$	1.5	$0^\circ$	linear
ODT3	$36.6 \pm 1.0$	$80.6 \pm 2.0$	2.5	$40 \pm 3^\circ$	linear

### 3.6 SINGLE BEAM OPTICAL DIPOLE TRAPS

The last confining method implemented is constituted by two crossed single beam optical dipole traps: ODT1 and ODT3. Before entering in the details of the atomic cloud transfer between the different trapping schemes, a brief description of the crossed trap resulting from the superposition of the two beams is reported below.

#### 3.6.1 CROSSED OPTICAL DIPOLE TRAPS FREQUENCIES

For each single trap the potential depth can be obtained using EQ. 1.58 where  $x, y, z$  are referred with respect to the beam propagating along  $\hat{x}$ :

$$\omega_{y,z}^2 = \frac{\alpha}{M} \frac{8P}{\pi(w_{oy}w_{oz})^2}; \quad \omega_z^2 = \frac{\alpha}{M} \frac{4P\lambda^2}{\pi^2(w_{oy}w_{oz})^4} \quad (3.25)$$

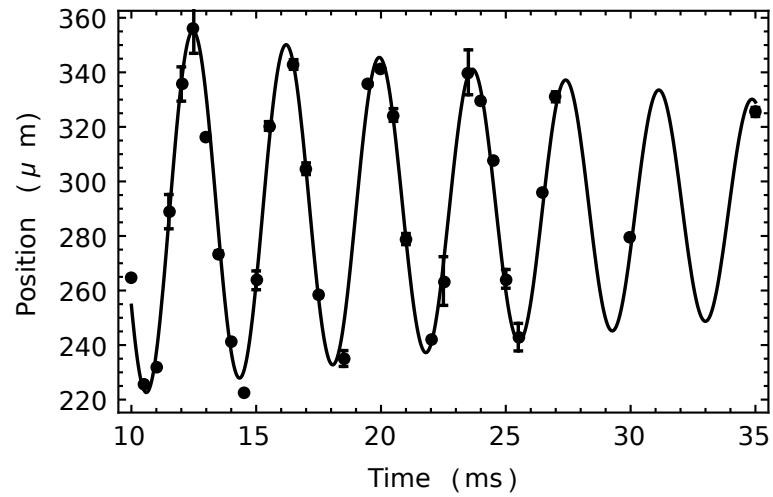
where gravity has been neglected and an elliptic waist beam is considered. For a wavelength of  $\lambda = 1064 \text{ nm}$  and a waist of  $w_0 \approx 10 \mu\text{m}$  it holds  $\omega_{y,z}^2 \sim \times 10^2 \omega_x^2$  then, given the same kinetic energy, the oscillation amplitude of a particle is  $\approx 1 \times 10^2$  longer in the longitudinal direction with respect to the transverse one and as a result atoms are essentially confined along a line.

In our experiment, in order to obtain a three-dimensional trap with comparable lengths along the three axis, two crossed beams are used at an angle of  $40^\circ$ . When different ODTs are crossed, the resulting potential calculation is performed in a slightly different way than using (EQ. 3.25) that is referred with respect each beam axis. When two beams are superimposed the reference axis are function not only of the crossing angle but also of the relative beam intensities and waists. A calculation can be performed using EQ. 3.18: the light intensity in EQ. 1.57 is infinitely derivable, hence the matrix obtained with all the nine second order crossed derivatives is symmetric so it has three real eigenvalues ( $\xi_1, \xi_2, \xi_3$ ) and their relative eigenvectors can be used to define a basis ( $\hat{x}', \hat{y}', \hat{z}$ ) where EQ. 3.20 holds ( $\hat{z}' = \hat{z}$  given that all beams propagate in the  $xy$  plane). The three trap frequencies then are:

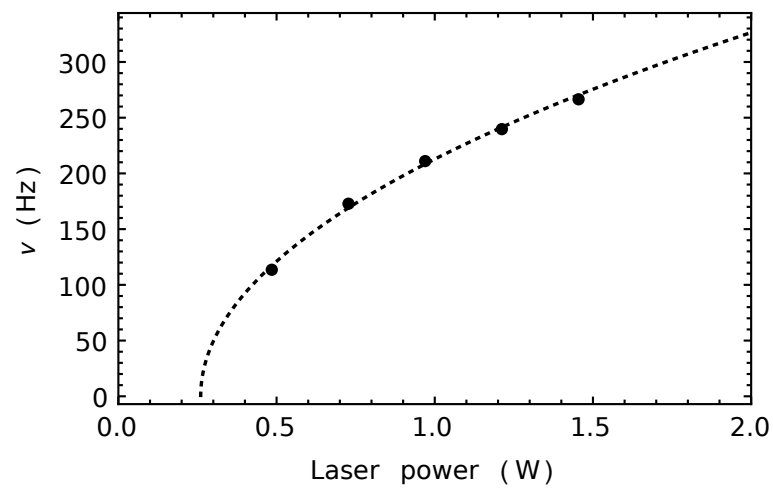
$$\omega_{x'}^2 = \frac{\xi_1}{M}, \quad \omega_{y'}^2 = \frac{\xi_2}{M}, \quad \omega_z^2 = \frac{\xi_3}{M} \quad (3.26)$$

that can be used in EQ. 3.19.

Calculation relies on the beam waist, the laser power and the atomic polarizability. The laser power is easily measured, the dysprosium polarizability at 1064 nm has been measured



(A)



(B)

FIGURE 3.19: Example of vertical trap frequency measure. (A) For ODT1 at 1.45 W,  $\nu = 268 \pm 1$  Hz. (B) ODT1 frequency as a function of the laser power. From EQ. 3.25 the fit function is  $\nu = A\sqrt{P - P_0}$  where  $P_0 \sim 0.3$  W is the minimum laser power that permits to hold the cloud against the gravity. The error bars in (B) are within the dots.

[31] for the  $^{164}\text{Dy}$  (for the  $^{162}\text{Dy}$  the difference is expected to be negligible) then the remaining unknown parameter is the beam waist. Measurements of the beam waist have been done recording the beam with a CCD camera at various distances and then fitting the measured waist with  $w(z) = w_0 \sqrt{1 + \left(\frac{z}{z_R}\right)^2}$ . But this method, although accurate, has the disadvantage that can't be done in the vacuum chamber: once the position of the minimum waist ( $w_0$ ) is found outside the vacuum chamber, the beam has to be deviated into the chamber thus the position at which beams intersects isn't known exactly. In a different prospective, by comparing the measured frequency traps for different laser powers with the calculated one, the beams waist (the only parameter not known) can be inferred indirectly. In FIG. 3.19 it is reported an example of such a measurement for the ODT1.

Once the waists of the three optical dipole traps are known, the resulting values are reported in TAB. 3.3. The trap potentials can be calculated in various configurations: the potential of the ODT1 superimposed to the resonator is plotted FIG. 3.20 along with the absorption image. In FIG. 3.21 it is plotted the potential for the crossed trap along with a 3D representation of the shape of the atomic thermal cloud. We observed that for a given vertical trap depth  $U_0$ , the corresponding temperature of the atomic cloud is approximately  $T_z = 1/7 U_0$  thus the 3D plot is the surface determined by the solution of this equation.

The method we used for measuring the trap frequencies consisted in loading the two traps and performing an evaporation ramp until reaching a cloud temperature of 1  $\mu\text{K}$ . Then the two traps are switched off for 0.6 ms and ODT1 is again switched on at the desired power. The trap is held for a variable time  $t$  and then again the cloud is released and finally, after a fixed time of flight of  $t_F = 5$  ms, an absorption image is taken. In this way, by considering the centre of mass of the cloud at rest in the origin when the trap is shut down at  $t = -t_0$ , its position and velocity when the recapture start at  $t = 0$  are respectively  $z_0$  and  $v_0$ . During the variable recapture time, the position and velocity of the centre of mass of the cloud are respectively:

$$\begin{aligned} z(t) &= A \sin(\omega_z t + \phi) & z_0 &= -1/2 g t_0^2 & v_0 &= -g t_0 \\ v_z(t) &= \omega_z A \cos(\omega_z t + \phi) & A^2 &= z_0^2 + \frac{\omega_z^2}{v_0^2}; & \tan \phi &= \frac{z_0}{\omega_z/v_0} \end{aligned} \quad (3.27)$$

in the end, when the absorption image is taken at  $t = t_F$  the position of the centre of mass of the cloud is:

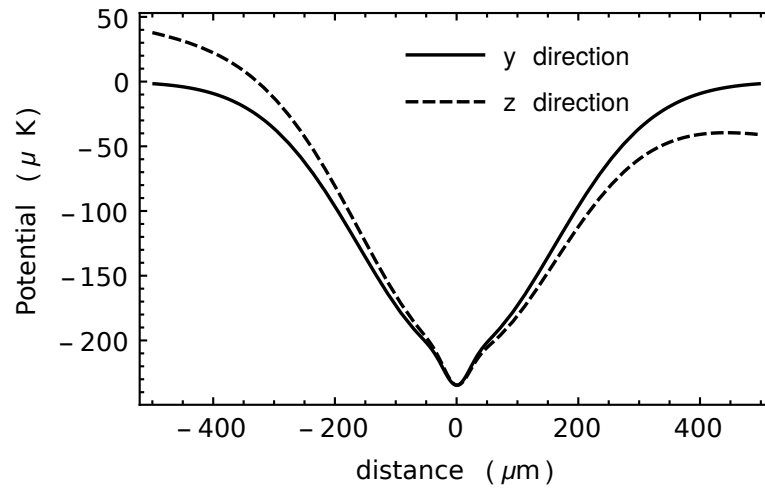
$$z(t_F) = A \sin(\omega_z t + \phi) + \omega_z A \cos(\omega_z t + \phi) t_F - \frac{1}{2} g t_F^2. \quad (3.28)$$

Once the data are collected, the actual fit is done with the function:

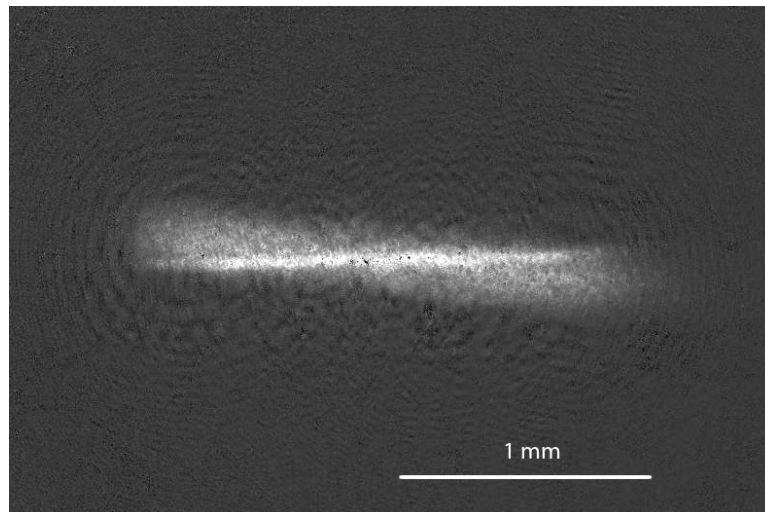
$$z = \left(O + A \sin(\omega t + \phi)\right) e^{-t/\tau} \quad (3.29)$$

where  $A$ ,  $O$ ,  $\phi$  and  $\tau$  are fitting parameters. The exponential term, although its origin is not clear (at least to me, maybe it is necessary because the underlying hypothesis in the model depicted is that the trapped cloud is a rigid body while it actually isn't, furthermore the potential is not constant in the cloud volume) is necessary in order to obtain a reasonable fit. The waists resulting from these measurements are reported in tab TAB. 3.3.

Given the strong dipolar nature of dysprosium [17] the trap frequency  $\omega_z$  along the polarization direction of the dysprosium atoms  $\hat{z}$  must be higher than the average frequency  $\bar{\omega}_{x'y'}$  in the

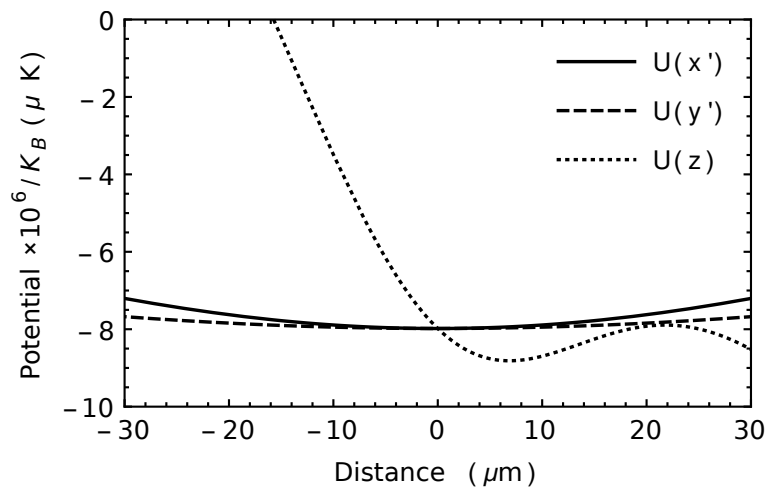


(A)

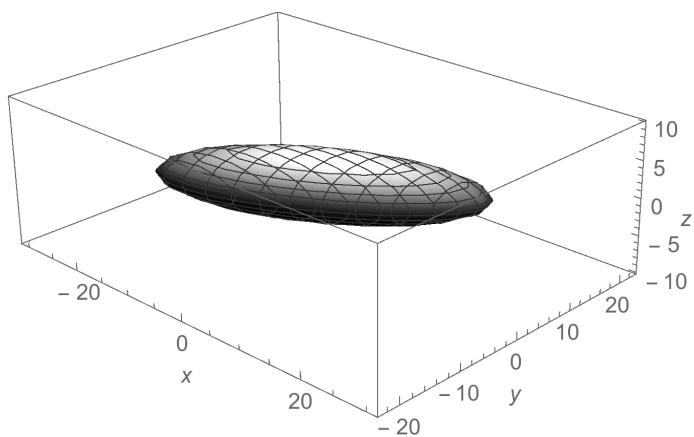


(B)

FIGURE 3.20: (A) Calculated potential of the ODT1 superimposed to the resonator optical dipole trap as a function of  $x$  and  $z$ : ODT1 is much weaker than the resonator and it presents as the small peak at the top of each well. (B) Absorption image of the transfer from the resonator to the ODT1, the tight longitudinal confinement of the resonator trap prevent atoms to spread along the ODT1 direction. The intensity of the light injected into the cavity is already reduced to permit the transfer to the ODT1.



(A)



(B)

FIGURE 3.21: Example of potential calculation for the crossed trap with  $\text{ODT1}$  at  $0.05\text{ W}$  and  $\text{ODT3}$  at  $0.8\text{ W}$ . (A) The potential (expressed as  $U/k_B \times 10^6$ ) in the three directions, it can be seen the gravity effect in the  $\hat{z}$  direction. (B) The 3D graph is the surface determined by the solutions of  $\frac{1}{7}T_z = \frac{1}{2}M(\omega_{x'}^2 x'^2 + \omega_{y'}^2 y'^2 + \omega_z z^2)$ ; the vertical trap depth is  $0.4\ \mu\text{K}$  and the aspect ratio of the trap is  $\lambda = 3.9$  [17].

plane  $\hat{x}'\hat{y}'$  orthogonal to  $\hat{z}$  and the *aspect ratio*:

$$\lambda = \frac{\omega_z}{\sqrt{\omega_{x'}\omega_{y'}}} = \frac{\omega_z}{\bar{\omega}_{x'y'}} \quad (3.30)$$

must satisfy  $\lambda > 3$  [26]. For this reason, the laser beam forming ODT<sub>3</sub> is elliptically shaped with the smaller axis of the waist directed along  $\hat{z}$ . Crossing the two beam at a different angle than  $\pi/2$  permits to vary the potential shape and orientation as a function of the two beams powers while assuring an aspect ratio  $\lambda > 3$ .

### 3.6.2 ODTS LIFETIME

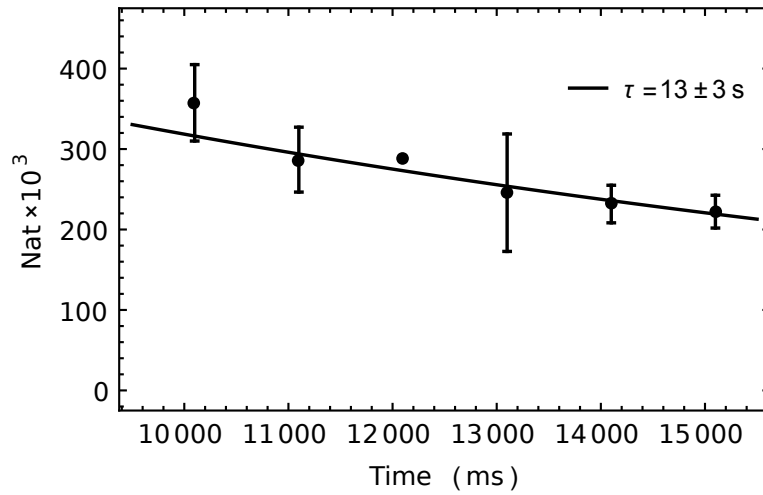
The crossed trap lifetime is an important parameter and a study of the trapped population time evolution provides information about the loss mechanism involved. Furthermore, as the trapping potential depth decrease during the evaporation ramps, trap frequencies also decrease and as a consequence the velocity at which the potential depth is decreased needs to be slowed (see Sec. 1.6). Finally having a trapped sample with a long lifetime allows for future studies to be performed.

The study is done measuring the number of trapped atoms at successive longer times. From the results, plotted in FIG. 3.22, it can be seen that, for higher temperature the trap lifetime is quite long  $\sim 13$  s and is well fitted with a single exponential function meaning that the atom loss isn't due to the two or three body processes. At colder temperature (hence at lower laser intensity) the lifetime is shorter  $\sim 1.7$  s but the population evolution is again well fitted with a single exponential, atom losses are probably due to some noise in the laser radiation although from the plot (not shown here) of the temperature time evolution it doesn't appear clearly.

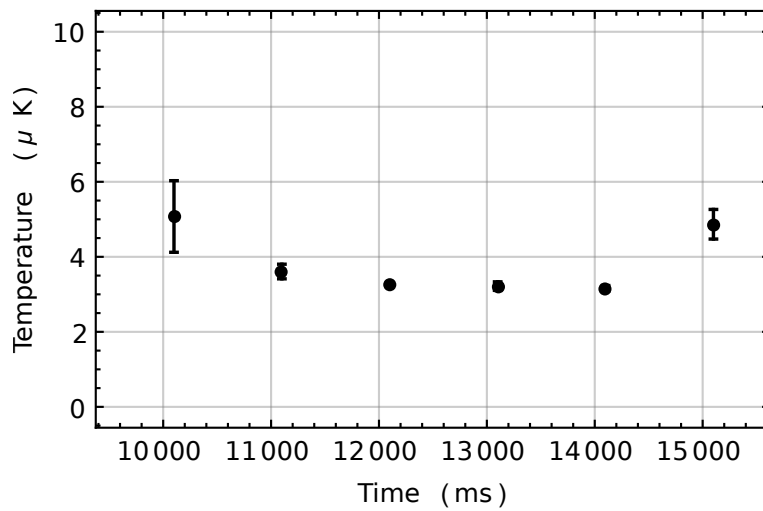
## 3.7 EVAPORATIVE COOLING AND FIRST SIGNS OF BOSE-EINSTEIN CONDENSATION

The evaporative cooling process begins as soon as atoms are transferred from the compressed MOT to the resonator optical dipole trap. As said, atoms captured in the MOT are pumped in the  $J = 8$ ,  $m_J = -8$  state and a constant and uniform magnetic field of 3 G is applied during the whole time in order to prevent spin-flip collisional losses.

The power of the three lasers as function of time are reported in FIG. 3.23. The graph starts at the end of the MOT phase. The resonator light intensity is ramped up during the last MOT compression phase until a potential depth of 200  $\mu$ K, that are sufficient to trap up to  $3 \times 10^7$  atoms at 30  $\mu$ K. At the same time, also the ODT<sub>1</sub> is activated at 1.5 W then the resonator power is exponentially decreased in 2 s down to a potential of 20  $\mu$ K. In this stage, atom are prevented to move along the ODT<sub>1</sub> propagation direction thanks to the longitudinal periodicity of the resonator potential (EQ. 3.16 and FIG. 3.20) which provides a strong longitudinal confining force. At this point the ODT<sub>3</sub> trap is activated providing the confinement along the ODT<sub>1</sub> propagation direction



(A)



(B)

FIGURE 3.22: Number of atoms (A) and temperature (B) of the atomic cloud held in the crossed optical dipole trap without evaporation. This gives an estimate of the heating rate.

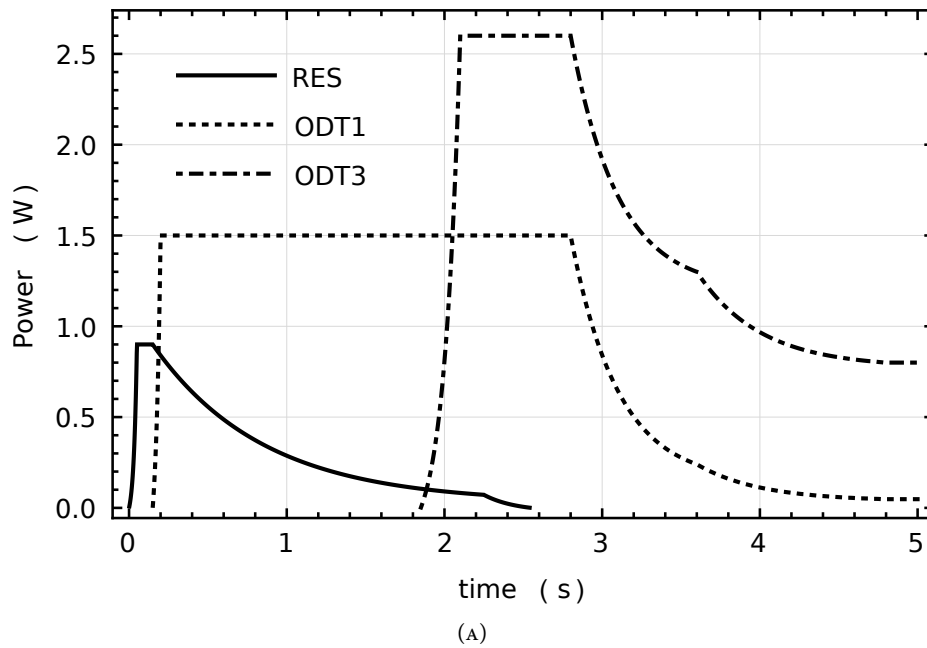


FIGURE 3.23: Time sequence of the lasers power during evaporative cooling ramps. The graph starts at the end of the MOT phase. The optical power in the resonator is the power of the incoming beam, not the power inside the cavity.

when the resonator laser power is reduced by a factor of  $1 \times 10^{-4}$ . In the remaining crossed trap are collected up to  $1 \times 10^6$  atoms at  $4 \mu\text{K}$  while the calculated trap depth is  $34 \mu\text{K}$  with an aspect ratio of  $\lambda = 3$ . In the first 1600 ms of the evaporation stage the light intensity of ODT1 is decreased, then both ODT1 and ODT3 laser power are decreased down to 50 mW for ODT1 and 800 mW for ODT3, the entire evaporation phase lasts 5 s. This final potential is plotted in FIG. 3.21 the trap depth is  $0.9 \pm 0.1 \mu\text{K}$  and the trap frequencies are  $\omega_z = 2\pi \times 141 \pm 1 \text{ Hz}$ ,  $\omega_{y'} = 2\pi \times 81.0 \pm 0.5 \text{ Hz}$  and  $\omega_{x'} = 2\pi \times 27.0 \pm 0.2 \text{ Hz}$ .

In the absorption images of FIG. 3.24, taken at the end of the process described above with a time of flight of 35 ms, it can be seen how the atomic density profile changes from a gaussian profile into a parabolic profile, the last meaningful temperature measure indicates a temperature of 100 nK and the number of atoms is roughly  $5 \times 10^4$ .

The emerging of the parabolic peak in the gaussian thermal distribution of the cloud density profile, as predicted in the Thomas-Fermi limit [18] is the sign of the phase transition toward Bose-Einstein condensation of  $^{162}\text{Dy}$ . A more detailed study is necessary, and will be done in the next future. The first dysprosium condensate has been achieved in 2011 for the isotope  $^{164}\text{Dy}$  (see ref. [26]).

In FIG. 3.25 we report the measurement of the lifetime the condensate. Its lifetime is comparable with the one measured for a thermal cloud at  $0.4 \pm 0.1 \mu\text{K}$ , the data are well fitted with a single exponential.

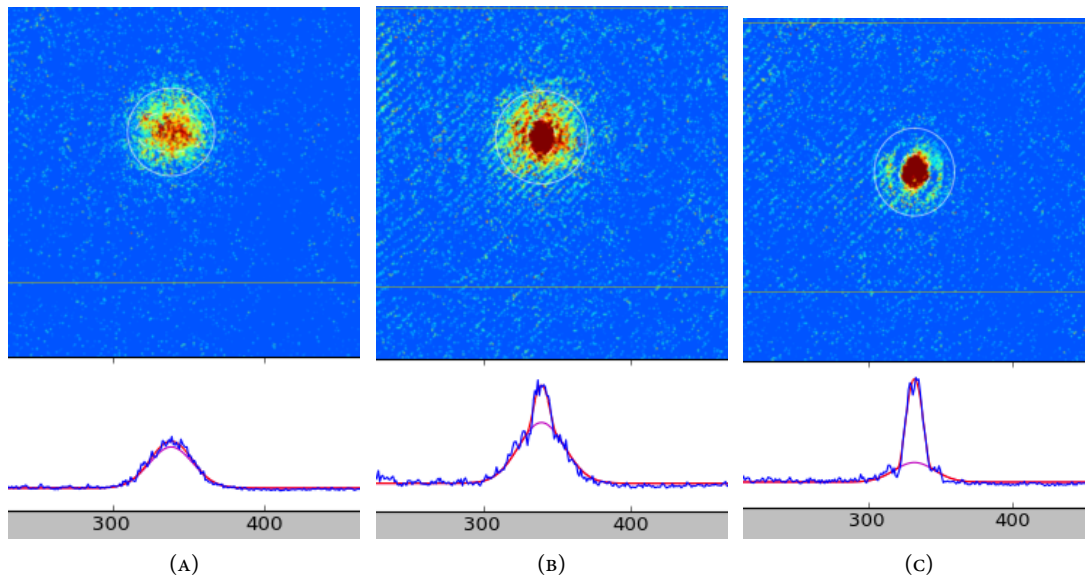


FIGURE 3.24: False colours absorption images taken with a time of flight of 35 ms along the vertical direction. The images are a screenshot of the program used to extract data from the images collected. The blue lines represent the integral of the column pixel values; the red lines is a bi-modal (gaussian + Thomas-Fermi) fit to these data.

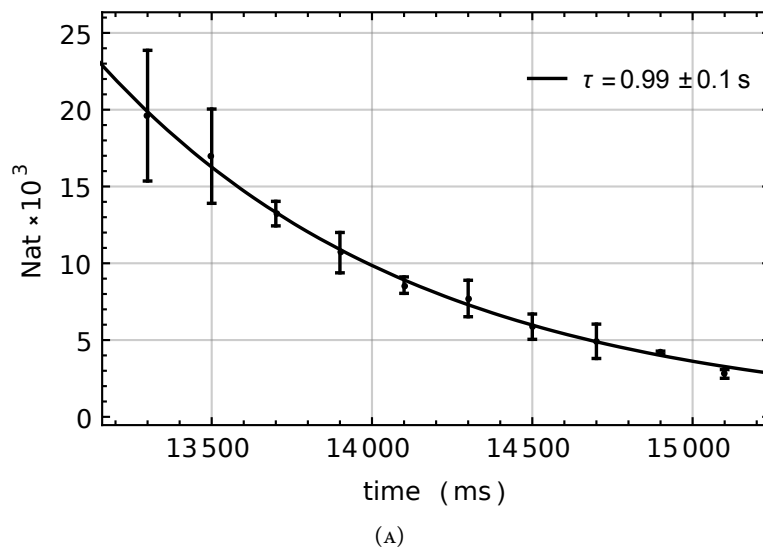


FIGURE 3.25: Lifetime of the condensate.



# CONCLUSIONS

During the first days of my Thesis the measures of final velocity of dysprosium atoms slowed by the Zeeman slower were in progress while this Thesis ends with the first characterization of the Bose-Einstein condensation. For me it is without any doubt an honour to present these results in my Diploma Thesis.

During the first part of my experience in the laboratory I participated to the realization of some electronics while becoming familiar with the complexity of the experimental apparatus, then I took part in many of the measurements and finally realized a Mathematica code capable to calculate the depth and the trapping frequencies of a combination of optical dipole traps. This has allowed the possibility to compare the experimental measurements of the trapping frequencies to the theory and so precisely calibrate the waist of the laser beams used for the ODTs, which are very hard to measure experimentally.

Today, in addition to the other Bose-Einstein condensates of dysprosium already realized before this Thesis was started, other experiments are on the way to attain quantum degeneracy. This is a clear sign of the interest generated by the dipole-dipole interaction in the physics of ultracold atoms.

Achieving the quantum degeneracy for alkali atoms is nowadays well proved but for submerged-shell lanthanides it was far from being obvious given their complex electronic structure. The transition chosen to obtain the MOT has allowed to limit the apparatus complexity but has required a careful tuning of the MOT itself and of the ZS. The optical dipole trap realized with a Fabry-Perot cavity is another peculiarity of our setup that allowed to obtain a large waist optical dipole trap with the use of a relatively low power laser and again it wasn't known if it could work with dysprosium. At this point it can be said that the experimental apparatus has proven to be well conceived and rather stable.

The Bose-Einstein condensate obtained is the key starting point for a series of quantum phases that are planned to be studied. Another important factor in view of these studies is the ability to control the  $s$ -wave scattering length, this days is under exam the Feshbach spectrum of dysprosium and the first characterization of a broad low magnetic field resonance is started. The new experimental tool, the Bragg spectroscopy, will be implemented in the near future, allowing a momentum selected excitation of the condensate.

The prospects of this experiment, once concluded the characterization and optimization phase of the Bose-Einstein condensate, are multiple and very exciting. By adding some extra laser beams, it will be possible to produce 1D, 2D or 3D optical lattices where the dipolar condensate can be loaded. This will enable the exploration of new quantum phases, in particular to undertake the long-awaited quest for the super-solid phase. Finally, with a small change in the frequency

stabilization chain of the two main lasers (the 421 nm and the 626 nm one), one of the Fermionic isotopes of dysprosium will be cooled, trapped and eventually reduced to quantum degeneracy. This will enlarge the wealth of possibilities of studies offered by this experiment.

I believe that working with the two joint teams from Lens and from CNR-INO for my Diploma thesis has been an interesting and productive experience. I took part in a poster section at the INO Annual Symposium 2018 and the characterization of our MOT has been published. In the experiment there are aspects concerning different subjects I encountered in my studies and this gave me the opportunity to put to work what I have studied in my courses and to gain a deeper understanding of the light-matter interaction. I also faced my limits but I was lucky enough to meet physicists that helped me to overcome some of them, it has been a very meaningful experience in my life.

# BIBLIOGRAPHY

- [1] M. H. Anderson *et al.* “Observation of Bose-Einstein Condensation in a Dilute Atomic Vapor”. *Science* **269** (1995).
- [2] Andrew J. Berglund, James L. Hanssen, and Jabez J. McClelland. “Narrow-Line Magneto-Optical Cooling and Trapping of Strongly Magnetic Atoms”. *Physical Review Letters* **100**.113002 (2008).
- [3] Leonardo del Bino. “Development of an experimental apparatus for the realization of dipolar quantum gases of Dysprosium atoms”. Tesi Magistrale. Università di Firenze, 2015.
- [4] Eric D. Black. “An introduction to Pound–Drever–Hall laser frequency stabilization”. *American Journal of Physics* **69**.79 (2001).
- [5] Immanuel Bloch, Jean Dalibard, and Wilhelm Zwerger. “Many-body physics with ultracold gases”. *Reviews of Modern Physics* **539**.885 (2008).
- [6] Max Born and Emil Wolf. *Principles of optics*. Cambridge university press, 2005.
- [7] C. C. Bradley *et al.* “Evidence of Bose-Einstein Condensation in an Atomic Gas with Attractive Interactions”. *Phys. Rev. Lett.* **75**.1687 (1995).
- [8] Calude Cohen-Tannoudji and David Guéry-Odelin. *Advances in Atomic Physics An Overview*. World Scientific, 2011.
- [9] K. B. Davis *et al.* “Bose-Einstein Condensation in a Gas of Sodium Atoms”. *Physical Review Letters* **75**.22 (1995).
- [10] D. Dreon *et al.* “Optical cooling and trapping of highly magnetic atoms: the benefits of a spontaneous spin polarization”. *Journal of Physics B* **50**.6 (2017).
- [11] C. J. Foot. *Atomic physics*. Oxford university press, 2005.
- [12] A. Frisch *et al.* “Narrow-line magneto-optical trap for erbium”. *Physical Review A* **85**.051401(R) (2012).
- [13] R. Grimm, M. Weidemüller, and Y. B. Ovchinnikov. “Optical dipole traps for neutral atoms”. *Advances In Atomic, Molecular, and Optical Physics* **42** (1999).
- [14] T. W. Hänsch and B. Couillaud. “Laser Frequency Stabilization by Polarization Spectroscopy of a Reflecting Reference Cavity”. *Optics Communications* **35**.3 (1980).
- [15] B. R. Judd and I. Lindgren. “Theory of Zeeman Effect in the ground multiplets of rare-earth atoms”. *Physical Review* **122**.6 (1961).

- [16] W. Ketterle and N.J. van Druten. "Evaporative Cooling of Trapped Atoms". *Advances in Atomic, Molecular, and Optical Physics* **37**.181 (1996). Ed. by B. Bederson and H. Walther.
- [17] T. Koch *et al.* "Stabilization of a purely dipolar quantum gas against collapse". *Nature physics* **4** (2008).
- [18] T. Lahaye *et al.* "The physics of dipolar bosonic quantum gasses". *Rep. Prog. Phys.* **72**.126401 (2009).
- [19] Mingwu Lu, Seo Ho Youn, and Benjamin Lev. "Spectroscopy of a narrow-line laser cooling transition in atomic dysprosium". *Physical Review A* **83**.012510 (2011).
- [20] O. J. Luiten, M. W. Reynolds, and J. T. M. Walraven. "Kinetic theory of the evaporative cooling of a trapped gas". *Physical Review A* **53**.1 (1996).
- [21] T. Maier *et al.* "Narrow-line magneto-optical trap for dysprosium atoms". *Optics Letters* **39**.11 (2014).
- [22] W.C. Martin, Romuald Zalubas, and Lucy Hagan. *Atomic Energy Levels - The Rare-Earth Elements*. NSRDS-NBS, 1978.
- [23] D. J. McCarron, S. A. King, and S. L. Cornish. "Modulation transfer spectroscopy in atomic rubidium". *Measurement Science and Technology* **19**.10 (2008).
- [24] James M. McCormack, Peter R. Platt, and Richard K. Saxer. "Vapor Pressure of Dysprosium and Erbium". *Journal of Chemical and Engineering Data* **16**.2 (1971).
- [25] Harold J. Metcalf and Peter van der Straten. *Laser cooling and Trapping*. Springer, 1999.
- [26] Lu Mingwu *et al.* "Strongly Dipolar Bose-Einstein Condensate of Dysprosium". *Physical Review Letters* **104**.190401 (2011).
- [27] NIST, ed. *Atomic Data for Dysprosium*. 2016. URL: <http://physics.nist.gov/PhysRefData/Handbook/Tables/dysprosiumtable1.htm>.
- [28] Hans Pauly. *Atom, Molecule, and Cluster Beam I*. Springer, 2000.
- [29] M. Prentiss *et al.* "Atomic-density-dependent losses in an optical trap". *Optics letters* **13**.6 (1988).
- [30] E. L. Raab *et al.* "Trapping of Neutral Sodium Atoms with Radiation Pressure". *Physical Review Letters* **59**.23 (1987).
- [31] C. Ravensbergen *et al.* "Accurate Determination of the Dynamical Polarizability of Dysprosium". *arXiv:1801.05658v1* (2018).
- [32] Orazio Svelto. *Principles of Lasers*. Springer, 1998.
- [33] C Trefzger *et al.* "Ultracold dipolar gases in optical lattices". *Journal of Physics B: Atomic, Molecular and Optical Physics* **44**.19 (2011).

## RINGRAZIAMENTI

*Ringrazio il dr. Andrea Fioretti, perché è sempre, ma proprio sempre, stato attento e gentile. Mi ha aiutato a mantenere l'attenzione sull'obiettivo e mi ha incoraggiato e indicato la strada. Non è mai stato lontano, nemmeno da oltreoceano, e ha trovato sempre il tempo di ascoltare i miei dubbi, rispondere alle mie domande e offrirmi qualche consiglio che poi si è puntualmente rivelato prezioso. Devo ringraziare il prof. Danilo Giulietti, perché mi ha seguito con attenzione, spronato e incoraggiato, e per me ha sempre avuto una parola gentile. Ringrazio il dr. Carlo Gabbanini, che ha risposto a tutte le mie domande in modo preciso e puntuale, ed è sempre stato paziente, anche quando dimenticavo di accendere qualche recondito amplificatore. E grazie alla dr.ssa Eleonora Lucioni, che mi ha aiutato quando ho avuto paura. Anche lei mi ha ascoltato e, tante volte di fronte ai miei dubbi, mi ha spiegato che quello che stavo pensando non era poi sbagliato, solo non era esattamente come lo pensavo, e dopo tutto diventava subito più chiaro. Ringrazio il dr. Luca Tanzi che spesso mi ha fatto tornare a casa con una nuova domanda o una nuova risposta che ogni volta mi hanno insegnato qualcosa. Ringrazio il prof. Giovanni Modugno perché quando pensava a voce alta ha sempre fatto in modo che poi qualcosa la capissi anch'io. E ringrazio il dr. Guido Masella con cui ho condiviso i miei primi giorni in laboratorio e mi ha aiutato a non combinare disastri. Ringrazio la dr.ssa Silvia Gozzini che è stata disponibile e attenta, anche che stessi bene. E ringrazio Alessandro Barbini, che ha avuto pazienza e ha anche trovato il tempo di spiegarmi qualcosa di elettronica. E devo ringraziare Mauro Tagliaferri, che mi ha tenuto d'occhio sempre con un tocco di allegria sana, scanzonata e garbata. Ringrazio anche tutte le persone meno coinvolte nella mia tesi, la dr.ssa Clara Lanza, dr. Iginio Longo e il dr. Alessandro Lucchesini che sono stati gentili e simpatici. Li ringrazio tutti, perché mi hanno accolto con garbo e col sorriso e mi hanno fatto sentire bene.*

